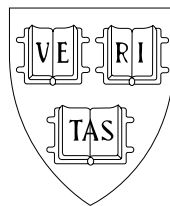# Interaction of Femtosecond Laser Pulses with Transparent Materials

Chris B. Schaffer

Harvard University

Cambridge, Massachusetts

May 2001

Interaction of Femtosecond Laser Pulses with Transparent Materials

A thesis presented

by

Chris B. Schaffer

to

The Department of Physics

in partial fulfillment of the requirements

for the degree of

Doctor of Philosophy

in the subject of

Physics

Harvard University

Cambridge, Massachusetts

May 2001

Thesis advisor: Eric Mazur　　　　　　　　　　　*Author: Chris B. Schaffer*

Interaction of Femtosecond Laser Pulses with Transparent Materials

Abstract

An intense femtosecond laser pulse can have an electric field strength which approaches or even exceeds the strength of the electric field that holds valence electrons in a transparent material to their ionic cores. In this regime, the interaction between the laser pulse and the material becomes highly nonlinear. Laser energy can be nonlinearly absorbed by the material, leading to permanent damage, and the material's nonlinear response to the laser field can, in turn, induce radical changes in the laser pulse itself. The nature of these nonlinear interactions, the changes produced in the material and to the laser pulse, as well as several practical applications are explored in this thesis. We measure the laser intensity required to damage bulk transparent materials and uncover the dominant nonlinear ionization mechanism for different laser wavelengths and material band gaps. Using optical and electron microscopy, we examine the morphology of the material changes induced by tightly-focused femtosecond laser pulses in bulk transparent materials, and identify several mechanisms by which material changes are produced. We show that a high repetition rate train of femtosecond laser pulses can provide a point source of heat located inside the bulk of a transparent material, an effect which no other technique can achieve. The mechanism for white-light continuum generation is uncovered through measurement of the laser wavelength, the material band gap, and the external focusing angle dependence of the continuum spectrum. Using a time-resolved imaging technique, we follow the dynamics of the laser-produced plasma over eight orders of magnitude in time, revealing picosecond time scale dynamics that have not been previously observed. Finally, we discuss applications in direct writing of optical waveguides and in sub-cellular laser surgery.

Table of Contents

List of Figures and Tables

Acknowledgments

I have been fortunate in my career and in my life to be surrounded by and to work with great people. In these pages, I would like to thank the many friends and colleagues who helped me with the work presented in this thesis.

First I would like to thank my advisor, Prof. Eric Mazur, for his excellent mentorship during my five years at Harvard. Eric provided an ideal environment for me to begin my career as a professional scientist. He has always been receptive to and supportive of my ideas, allowing me the opportunity to direct the course of my research. This is a unique challenge for a graduate student, and I believe that, by taking on this challenge, I have become a better and more confident scientist. Eric's emphasis on clear presentation of ideas will stick with me in my professional and non-professional activities for the rest of my life. On a personal level, one could not ask for a better advisor than Eric. He always asked me how my day was going before he asked about the experiment, and he always waited for me to catch up when we went mountain biking together. I also thank Eric for being understanding about my unconventional work and vacation schedule.

I would also like to thank the other members of my thesis committee. Prof. Henry Ehrenreich taught me virtually everything I know about solid state physics (any errors in this thesis lie with the author, not the teacher), and has always had an encouraging interest in my work. In addition to serving on my thesis committee, Prof. Jene

Golovchenko, gave me the opportunity to teach, for three consecutive years, one of the most unique and rewarding classes at Harvard, the Freshman Seminar in Experimental Physics. Guiding three years of freshmen through complicated physics experiments gave me confidence in my ability to lead a research group. Jene always encouraged and supported my experimental ideas for the class and for my thesis research, a compliment I do not take lightly given his stature as an experimental physicist.

The collaborative approach to research favored in Eric's group has given me the opportunity to work directly with a long list of excellent scientists. Two post-docs, Dr. Eli Glezer and Dr. André Brodeur provided mentorship at crucial stages in my graduate career. Eli's initial experiments launched the project that is the focus of this thesis. I was very fortunate to work with Eli for my first year as a member of Eric's group. Eli is a powerhouse experimentalist who taught me to try new ideas and always think of applications and consequences beyond the obvious. His patient introduction to the project provided me with a firm understanding from which all subsequent work developed. During my third year as a graduate student, I collaborated extensively with André. It was André who taught me to be systematic and precise. He helped me transform from a young graduate student with lots of ideas to a critically thinking scientist with a research plan. The work in Chapters 3 and 5 is the result of our very productive year working together.

I worked closely with three graduate students in Eric's group: Nan Shen, Jon Ashcom, and Albert Kim. Nan and I began working together during our second year in graduate school, and our collaboration has been not only productive but also pleasant. Nan is one of the kindest people I know and I hope that some of that kindness has rubbed off on me. The experiments on biological samples described in Chapter 7 represent the

beginning of the results from our collaboration. Jon joined the project more than a year ago and brought a new degree of precision to the experiments at a crucial time. Without Jon's help, the results described at the end of Chapter 5 would not have been presentable. Jon has also been a good friend and roommate who has tolerated both my personality quirks and my apparent inability to help him clean our apartment. Albert and I joined Eric's group at the same time and bonded well from the start (we share similar character flaws). Although we only began working together on experiments in our last year together, we have been very productive (experiments not described in this thesis), and I am saddened that Albert will, at least temporarily, be leaving science. Albert has been a good friend throughout my graduate school years, and I look forward to our continued friendship.

The Mazur lab was filled with great people during my stay there. Rich Finlay and Tsing-Hua Her, both careful experimentalists, made me look bad by working so hard. Aryeh Feder and Paul Callan are directly responsible for my confused understanding of international politics, which, incidentally, is a big step up from my former complete lack of understanding. Claudia Wu reminded me that, even in a physics lab, not everything is about science. Li Huang was a good friend, who I sorely missed after she graduated. Rebecca Younkin has showed unbelievable patience with me, and though many of her efforts to keep me honest and respectable have failed, they were all appreciated. I have enjoyed working with and hanging out with Chris Roeser, Jim Carey, and Raphael Gattass, the next generation of Mazur lab graduate students. I have always admired Dr. Catherine Crouch and Adam Fagan's work on education reform, and, if I ever get a class of my own, I hope they will be willing to share their latest ideas.

In Eric's group, I had the opportunity to advise several wonderful undergraduate students. Nozomi Nishimura was the first student I advised. We worked together for three years, until she booted me off the project we started together. The work in biological samples described in Chapter 7 is the result of our collaboration with Nan. Alan Jamison did the experimental work described in the early sections of Chapter 4 and was a wonderful advisee. Alan's perspective on things, though often strange, was always refreshing. Jose Garcia was my most dedicated student and is responsible for the work at the end of Chapter 4 and the waveguide writing experiments described in Chapter 7. In addition, Jose has been a great friend and was a good roommate during his second stay in Cambridge. Willie Leight, a high-school student at the time I advised him, showed remarkable scientific maturity and helped immensely with the waveguide experiments. Deb Datta is one of the smartest people I have ever met, and it has been my pleasure to have played a role in his education since his first day at Harvard. Deb contributed greatly to the single-cell experiments described in Chapter 7 of this thesis. Jeremy Huang developed into an independent experimentalist in record time, and I look forward to the results of his work with Jon. Jennifer Hseih, my last advisee at Harvard, was infinitely patient with me while I finished this thesis. Although I was not an ideal advisor for her, she was an ideal student, and I envy the member of the Mazur lab who she works with after I leave.

I received an unusually good background in experimental physics as an undergraduate student at the University of Florida. Prof. Dave Reitze took a chance by taking me on as a research assistant early in my second year of college. In the three years I worked in Dave's lab I learned the experimental skills that allowed me to get a quick

start in graduate school. Dave has remained an active supporter of my work, and I look forward to finally buying him the drink that I owe him. I would also like to thank Anatoly Efimov, a graduate student in Dave's group while I was there, for patiently teaching me the basics of ultrafast laser science.

Several collaborators outside Harvard played a critical role in the experiments described in this thesis. Prof. Alex Gaeta at Cornell did the simulations presented in Chapter 5 and has provided valuable input for all our experiments on continuum generation. My collaboration with Prof. Jeff Squier and Dr.Dave Fittinghoff at the University of California, San Diego in the last year of my graduate studies not only gave me the opportunity to surf some of the world's best waves, but also produced some of the waveguide splitter results discussed in Chapter 7. I look forward to working for Jeff in sunny southern California as a post-doc, and I sincerely hope he will understand if I come in late on days when the waves are really good.

My "collaboration" with Nozomi extended beyond the lab pretty soon after we started working together. I consider myself very fortunate to have found someone with whom I am so compatible. I can work a full day in the lab with Nozomi, and still be excited about spending the rest of the day with her. I love you very much, Nozomi, and I look forward to us living and working together again in California.

There is something special about the friends you grow up with, and it's even better when they are also great people. I've hung out with Glen Silba, Chris Encinas, and Davey Balboa for almost 15 years now. I don't have to hope our friendship will last another 15 or 50 years, I just know that's the way it will be. Glen and I have, so far, surfed Florida, Costa Rica, and Hawaii together. I can't wait to add California (I'm

telling you, Glen, the water isn't that cold), the South Pacific islands, Bali, and who knows where else to that list. Chris's efforts to get me into shape have produced some results, and I promise to do better in California. Davey has finally, by getting married, added a hint of respectability to our group – I doubt that it is enough. Adrian Berry, another long-time friend, is on her own path to becoming a scientist. I have enjoyed our recent talks about the science we do and how much we slack off at lab and I hope they continue. Here in Cambridge, I have had many roommates and friends who made my time more fun, and I thank them all: Jay Goldman, John Baskey, Dave Morin, Rob Jenks, Paul Evans, Sarah Pohlen, Chia-Lin Kao, Hiroko Nagai, and many others.

Finally I would like to thank my family for their loving support throughout these many years of my education. My parents, Larry and Carolyn Schaffer, and my sister, Karen Schaffer, encouraged me throughout my undergraduate and graduate studies, and I hope I can count on more of the same in the future.

Citations to previously published work

Parts of this dissertation have appeared or will soon appear in the following publications:

C. B. Schaffer, A. Brodeur, J. F. Garcia, and E. Mazur, "Micromachining bulk glass using femtosecond laser pulses with nanojoule energy," *Optics Letters* **26**, 93 (2001).

C. B. Schaffer, A. O. Jamison, J. F. García, and E. Mazur, "Structural changes induced in transparent materials with ultrashort laser pulses," to appear in *Ultrafast lasers: technology and applications*, edited by M. E. Fermann, A. Galvanauskas, and G. D. Sucha (expected 2001).

E. N. Glezer, C. B. Schaffer, N. Nishimura, and E. Mazur, "Minimally disruptive laser-induced breakdown in water," *Optics Letters* **22**, 1817 (1997).

C. B. Schaffer, A. Brodeur and E. Mazur, "Laser-induced breakdown and damage in bulk transparent materials using tightly-focused femtosecond laser pulses," submitted to *Journal of Measurement Science and Technology* special issue "Ultrashort electromagnetic pulse science: technology and measurement," edited by J.-F. Eloy (expected 2001).

C. B. Schaffer, A. O. Jamison, and E. Mazur, "Morphology of femtosecond laser-induced structural changes in bulk transparent materials," in preparation.

A. Brodeur, C. B. Schaffer, E. Mazur, K. D. Moll, A.M. Streltsov, and A. L. Gaeta, "Mechanisms of ultrafast white-light continuum generation," in preparation.

C. B. Schaffer, J. F. García, and E. Mazur, "Bulk heating of transparent materials using a high repetition-rate femtosecond laser," in preparation.

C. B. Schaffer, N. Nishimura, E. N. Glezer, and E. Mazur, "Dynamics of femtosecond laser-induced breakdown in water from femtoseconds to microseconds," in preparation.

C. B. Schaffer, A. Brodeur, J. B. Ashcom, N. Nishimura, and E. Mazur, "Band gap and wavelength dependence of femtosecond laser-induced breakdown in transparent materials," in preparation.

For my parents, Larry and Carolyn Schaffer

Study is like the heaven's glorious sun,
That will not be deep-searched with saucy looks.

William Shakespeare
Love's Labor's Lost, Act I, Scene i, Line 84

Where shall we take our stand to view the infinite & unbounded

William Blake
The Four Zoas, Night IX, Page 122, Line 24

And I saw as it were a sea of glass mingled with fire

The Book of Revelation, Chapter 15, Verse 2

Chapter 1

Introduction

The advent of femtosecond lasers has spawned whole new fields of scientific investigation. Most of this research relys on three unique characteristics of ultrashort laser pulses. First, a short pulse can be used to measure very fast processes. Such diverse phemenona as electron-phonon scattering, phonon vibration, and chemical bond breaking can all be directly time-resolved with femtosecond laser pulses. Second, a short pulse can create very nonequilibrium conditions. For example, because ionic cores respond much more slowly than valence electrons do, a femtosecond pulse can excite electrons to a very high temperature while the ions are still cold. Finally, a femtosecond pulse can provide an extremely high laser intensity. Electric field strengths that exceede the electric field that binds valence electrons to their constituite atoms are easily produced with a table-top laser system. As the electric field of the laser becomes comparable to or exceedes the binding fields that hold the material together, the familiar linear approximations used to describe the interactions between light and materials break down. This thesis is concerned with the highly nonlinear interaction between intense femtosecond laser pulses and transparent materials.

Usually when light propagates through a transparent material, nothing happens to either the material or the light. With a powerful femtosecond laser pulse, however, both the material and the light can be dramatically changed by the interaction. Despite a long history, much still remains to be learned about the fundamental mechanisms that govern the interaction of powerful laser pulses with transparent materials. Furthermore, as available pulse durations become shorter the problem must be revisited as new interaction regimes become accessible. In addition to the intrinsic scientific value of understanding the interaction mechanisms, the propagation of short pulses in transparent media is of great practical importance.

This thesis deals with several aspects of the interaction of intense femtosecond laser pulses with transparent materials. Several unique phenomena are demonstrated and studied: Tightly-focused femtosecond pulses "rip" the transparent material apart at the laser focus, producing permanent material change at the focus. This material change can be used to micromachine structures inside the bulk of the material. A train of femtosecond laser pulses serves as a point source of heat located *inside* the bulk of a transparent material, a feat that cannot be matched by any other technique. A loosely-focused femtosecond pulse changes its color as it propagates through a transparent material, producing a pulse of white light. This continuum generation is one of the most dramatic examples of the extraordinary difference between the interaction of normal light and of powerful laser pulses with transparent materials. These and related phenomena as well as applications in direct writing of waveguides and optical devices in bulk glass and in disruption of sub-cellular structures inside single cells are discussed in the following chapters.

Organization of this thesis:

Although all the work described in this thesis involves the interaction of short laser pulses with transparent materials, several different phemenona are studied and many different experimental techniques are used. For this reason, I have tried to make each of the experimental chapters (3 – 7) as "stand alone" as possible, so that they may be read independently.

Chapter 2: This chapter provides an introduction to the basic nonlinear propagation and ionization mechanisms that govern short-pulse behavior in transparent materials. The sections on nonlinear ionization are important for the ionization experiments described in Chapter 3 and the dynamics measurements presented in Chapter 6. The comparison of long and short pulse damage mechanisms is relevant to the damage morphology studies in Chapter 4, and the discussion of nonlinear propagation of femtosecond pulses is important for the continuum experiments described in Chapter 5.

Chapter 3: When a powerful femtosecond laser pulse is tightly focused into the bulk of a transparent material, the laser intensity at the focus can become high enough to nonlinearly ionize the material. Despite extensive research on these nonlinear ionization mechanisms in recent decades, much still remains unclear. In this chapter, techniques for measuring the threshold laser intensity for producing bulk material damage are presented. Measurements of this threshold intensity for different laser wavelength and different material band gap reveal the relative importance of different nonlinear ionization mechanisms.

Chapter 4: If enough laser energy is deposited into the material by nonlinear absorption, permanent material changes are produced at the laser focus. This chapter discusses the

changes induced in bulk material by tightly-focused femtosecond laser pulses. The morphology of the material change is carefully examined and different mechanisms for producing different morphologies are revealed. A new mechanism for bulk structural change that relies on depositing energy at a rate faster than it can escape by thermal diffusion is introduced. This new technique allows the bulk of a transparent material to be heated in a micrometer-sized region with nanojoule energy precision.

Chapter 5: When loosely focused into a transparent material, a femtosecond laser pulse can be transformed into a white-light continuum pulse. In this chapter, the dependence of the width of the continuum on laser wavelength and material band gap is presented. The results provide stringent constraints on models for continuum generation, and help bring forth the most satisfactory explanatinon for continuum generation presented to date. Preliminary data on the dependence of the continuum on external focusing angle is also presented, revealing a transition from laser propagation dominated by nonlinear effects to propagation dominated by linear focusing.

Chapter 6: The early chapters discuss the mechanism for producing a plasma and the morphology of the material damage that is ultimately produced. There are many processes that go on between the initial ionization and the final material change, however. In this chapter, the dynamics of laser-induced breakdown in water is measured over eight orders of magnitude in time, from the initial formation of a plasma to the final collapse of the cavitation bubble. The picosecond time scale dynamics, which have never before been measured, show puzzeling features that require additional work to properly explain.

Chapter 7: The refractive index changes produced in bulk transparent materials by femtosecond laser-induced damage can be used to fabricate optical devices. We demonstrate the direct writing of optical waveguides and waveguide splitters. Using the thermal mechanism discussed in Chapter 4, we micromachine waveguides using an unamplified femtosecond laser oscillator. In biological materials, tightly-focused femtosecond laser pulses provide a precise laser scalpel that can cut inside the material wihout affecting the surface. Applications in tissue-level skin surgery and in disruption of sub-cellular structures for biological research are presented.

Chapter 8: This thesis addresses many of the open questions regarding the interaction of femtosecond laser pulses with transparent materials, but much work remains to be done. In this chapter, the key results discussed in this thesis are reviewed and ideas for further experiments are suggested.

Chapter 2

Ultrashort laser pulses in transparent materials

In this chapter, we review some of the basic linear and nonlinear physics that governs how femtosecond laser pulses behave in transparent materials. A femtosecond pulse with only moderate energy can have an extremely high peak power and peak intensity. When materials are subjected to these high powers and intensities, the material response becomes highly nonlinear. For example, the index of refraction of the material becomes intensity dependent and infrared laser energy is absorbed in a normally transparent material, generating free electrons. After examining these effects, we review the state-of-the-art in ultrashort-pulse laser systems, and briefly describe the lasers used in the experiments presented in this thesis.

2.1   Linear propagation

The propagation of an electromagnetic wave in a medium is governed by the Maxwell equations.[1, 2] Combining the four Maxwell equations, and considering only the dipole response of the materal, we arrive at a wave equation for the electric field of the electromagnetic wave

$$\nabla \times \nabla \times \mathbf{E}(\mathbf{r},t) + \frac{1}{c^2}\frac{\partial^2}{\partial t^2}\mathbf{E}(\mathbf{r},t) = \frac{-1}{\varepsilon_0 c^2}\frac{\partial^2}{\partial t^2}$$ (2.1)

where $\mathbf{E}$ is the electric field vector, $\mathbf{P}$ is the induced dipole moment vector or polarization, c is the speed of light in vacuum, and ε_0 is the permitivity of free space. In the linear regime, when the laser intensity is low, the polarization is related to the electric field by

$$\mathbf{P}(\mathbf{r},t) = \varepsilon_0 \tilde{\chi}^{(1)}\mathbf{E}(\mathbf{r},t)$$ (2.2)

where $\tilde{\chi}^{(1)}$ is the linear susceptibility tensor, and we have taken the material's response to be instantaneous (i.e. no ferroelectric effect). For an isotropic medium, the susceptibility is a scalar quantity and the wave equation (2.1) can be simplified to

$$\nabla^2\mathbf{E}(\mathbf{r},t) + \frac{n_0^2}{c^2}\frac{\partial^2}{\partial t^2}\mathbf{E}(\mathbf{r},t) = 0$$ (2.3)

where the refractive index, n_0, is given by

$$n_0 = \sqrt{1 + \chi^{(1)}}$$ (2.4)

and we have further assumed that there are no free charges and that the susceptibility is spatially independent, so that the divergence of $\mathbf{E}$ is zero.[3] Equation (2.3) describes the propagation of optical radiation in media, and is the starting point for all of linear optics.

For a laser pulse to be short in time, it must be broad in frequency. For a femtosecond laser pulse, the spectral width is broad enough that the variation of the linear susceptibility over the bandwidth of the pulse is appreciable. For a 100-fs pulse with a center wavelength of 800 nm, for example, the spectrum must have at least a 10-nm

width. Because the group velocity of light in a material depends on wavelength, a short pulse tends to spread in time as it propagates through material. This disperson must be compensated to ensure a short pulse duration.[4]

2.2   Nonlinear propagation

When the laser intensity is high, the linear approximation in Eqn. (2.2) is no longer valid. The nonlinear dependence of the polarization on the applied electric field can be expressed as a power series in $\mathbf{E}$ [3, 5 - 7]

$$\begin{aligned}
\mathbf{P} &= \varepsilon_0 \left[\tilde{\chi}^{(1)} \mathbf{E} + \tilde{\chi}^{(2)} \mathbf{E} \mathbf{E} + \tilde{\chi}^{(3)} \mathbf{E} \mathbf{E} \mathbf{E} + ... \right] \\
&= \left[\mathbf{P}^{(1)} + \mathbf{P}^{(2)} + \mathbf{P}^{(3)} + ... \right]
\end{aligned} \tag{2.5}$$

where $\tilde{\chi}^{(n)}$ is the n-th order nonlinear susceptibility, and $\mathbf{P}^{(n)}$ is the n-th order nonlinear polarization, and we have dropped the explicit spatial and temporal dependence for clarity. All of perturbative nonlinear optics starts with the polarization given in Eqn. (2.5) going into the right hand side of the wave equation (Eqn. (2.1)).

Each of the electric fields on the right hand side of Eqn. (2.5) can have different frequency components, and there will be a nonlinear polarization produced at the sum and/or difference of these frequency components. The nonlinear polarization, in turn, drives the radiation of a field according to Eqn. (2.1). For the second-order polarization, for example, we could have two driving fields, $\mathbf{E}_1$ at frequency ω_1, and $\mathbf{E}_2$ at frequency ω_2. Assuming an isotropic medium so that $\tilde{\chi}^{(2)}$ is a scalar, the nonlinear polarization contains several different frequency components:

$$P^{(2)}(2\omega_1) \sim \chi^{(2)} E_1^2$$
$$P^{(2)}(2\omega_2) \sim \chi^{(2)} E_2^2$$
$$P^{(2)}(\omega_1 + \omega_2) \sim 2\chi^{(2)} E_1 E_2 \qquad (2.6)$$
$$P^{(2)}(\omega_1 - \omega_2) \sim 2\chi^{(2)} E_1 E_2^*$$
$$P^{(2)}(0) \sim 2\chi^{(2)}(|E_1|^2 + |E_2|^2)$$

The first two equations describe second-harmonic generation of each of the driving fields. The third and fourth equations describe sum- and difference-frequency mixing, respectively, and the final equation describes optical rectification. The number of possible combinations with the third-order polarization is even larger, allowing diverse phemenona such as two-photon absorption, four-wave mixing, and the nonlinear refractive index to be explained.

Radiation is not necessarily observed at all of the frequency components at which there is a nonlinear polarization. The generation of light by the nonlinear polarization, and the propagation of this light is governed by the wave equation (Eqn. (2.1)). In particular, to observe the radiation produced by the nonlinear polarization, the nonlinear process must be phase-matched, meaning that the radiation produced by the nonlinear polarization must stay in phase with the driving fields. Without such phase matching, there is destructive interference between the radiation produced by the nonlinear polarization at different positions in the material. Because the radiated field will, in general, have a different frequency than the driving field, and because the phase velocity of light depends on frequency, special arrangements must often be made to ensure that a nonlinear process is phase matched. Frequently, the driving and nonlinearly radiated field have crossed polarizations, and a birefringent material is angle-tuned so that the phase velocity for both fields is the same.[3]

2.2.1   The nonlinear refractive index

In this thesis, we are primarely concerned with the propagation of femtosecond pulses in amorphous materials such as glass. Because amorphous materials are isotropic, the tensor nature of the nonlinear susceptibilities can be dropped, and furthermore, because amorphous materials have inversion symmetry, all even-order terms in Eqn. (2.5) must vanish. To see this second point, consider a spatial inversion in a centrosymmetric material. We have $\mathbf{P}^{(2)} \to -\mathbf{P}^{(2)}$, $\mathbf{E} \to -\mathbf{E}$, but $\chi^{(2)} \to \chi^{(2)}$ because the material has inversion symmetry. We then have that

$$-\mathbf{P}^{(2)} = \varepsilon_0 \chi^{(2)}(-\mathbf{E})(-\mathbf{E}) = \mathbf{P}^{(2)}$$

(2.7)

and so $\mathbf{P}^{(2)} = 0$ which implies that $\chi^{(2)} = 0$. A similar argument holds for higher-order even terms in Eqn. (2.5).

For moderate laser intensities (up to about 10^{12} W/cm^2) in centrosymmetric media, we may terminate the expansion in Eqn. (2.5) after the third-order nonlinear polarization. Because the material is isotropic, $\mathbf{P}$ and $\mathbf{E}$ are parallel, and will henceforth be represented by scalars. Furthermore, because the material is isotropic and the refractive index depends on frequency, the only processes that will be phase-matched are those where all the fields have the same frequency, and therefore the same phase velocity. Including all three permutations of the fields on the right hand side of Eqn. (2.5) which contribute to the third-order nonlinear polarization, the polarization becomes

$$P = \varepsilon_0 [\chi^{(1)} + \frac{3}{4}\chi^{(3)}|E|^2]E$$

(2.8)

Following the same steps that led from Eqn. (2.1) to Eqn. (2.3) yields an index of refraction given by:

$$n = \sqrt{1 + \chi^{(1)} + \frac{3}{4}\chi^{(3)}|E|^2}$$

(2.9)

Taking the nonlinear term to be small compared to the linear susceptibility and expressing the electric field strength in terms of the laser intensity, I, we have

$$n = n_0 + n_2 I$$

(2.10)

where the laser intensity is

$$I = \frac{1}{2}\varepsilon_0 c n_0 |E|^2$$

(2.11)

and the nonlinear refractive index, n_2, is:

$$n_2 = \frac{3\chi^{(3)}}{4\varepsilon_0 c n_o^2}$$

(2.12)

This nonlinear refractive index gives rise to self-focusing and self-phase modulation, and explains many of the features of the propagation of loosely-focused short laser pulses in transparent materials.

2.2.2   Self-focusing

Self-focusing results from the intensity dependence of the refractive index, given by Eqn. (2.10). The spatial intensity variations in the laser pulse lead to spatial refractive index variations. Because n_2 is positive in most materials, the refractive index is higher at the center of the beam compared to the wings. This variation in refractive index acts as a lens and focuses the beam, as shown in Figure 2.1.

11
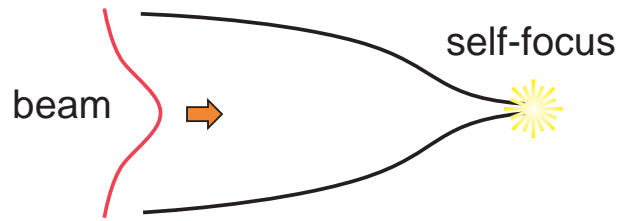
Figure 2.1 Schematic representation of self-focusing. The spatial dependence of the laser intensity leads to a spatial dependence of the refractive index, forming a lens which focuses the pulse.

Although the refractive index variation depends on the laser intensity, the strength of the self-focusing lens depends only on the peak power of the laser pulse.[8] This can be qualitatively understood as follows. Consider a collimated laser beam incident on a transparent material with sufficient power to self-focus inside the material. If the size of the incident laser beam is doubled, the laser intensity goes down by a factor of four resulting in a refractive index change that is smaller by a factor of four. The area of the self-focusing "lens," however, is also increased by a factor of four. This increase in area compensates for the decrease in refractive index change, giving the same refractive power.

As the power in the laser pulse is increased, self-focusing becomes stronger until, at some critical power, it balances diffraction and a filament is formed. If the peak power of the laser pulse exceeds this critical power for self-focusing then catastrophic collapse of the laser beam to a singularity is predicted.[8] The critical power, P_{cr}, is given by

$$P_{cr} = \frac{3.77\lambda^2}{8\pi n_0 n_2}$$

(2.13)

where λ is the laser wavelength, and is typically on the order of a few MW.[8] In real materials, other mechanisms halt the collapse of the beam due to self-focusing. In particular, as the laser beam self-focuses, the intensity rises and will eventually become sufficient to nonlinearly ionize the material (see Sections 2.3.1 and 2.3.2). The electron gas contributes a negative refractive index change (discussed in Section 2.3.4) that cancels the positive refractive index change produced by the intensity-dependent index, and prevents further self-focusing.[9]

A comprehensive theory of nonlinear pulse propagation in transparent materials for pulses whose power exceeds the critical power is still lacking, although much progress has been made in recent years.[9] For laser powers that are less than about a quarter of the critical power for self-focusing, however, the change in the spot size in the material due to self-focusing can be reliably calculated.[10] The laser intensity, I_{sf}, at the laser focus in the presence of weak self focusing increases with increasing peak power, P, according to

$$I_{sf} = \frac{I}{1 - P/P_{cr}}$$

(2.14)

where I is the laser intensity in the material in the absence of self-focusing.[8]

2.2.3   Self-phase modulation

Self-phase modulation is the temporal analogue of self-focusing. In self-focusing, the spatial intensity profile leads to a spatial refractive index profile which, in turn, focuses the beam. In self-phase modulation, the temporal dependence of the intensity profile

13

leads to a temporal dependence in the refractive index which, in turn, produces a time-dependent phase shift of the pulse. Qualitatively, the effect can be understood by considering the dependence of the phase velocity of the light on the intensity of the pulse. As shown in Figure 2.2, the temporal peak of the pulse sees a higher refractive index than the leading and trailing edges, so the electric field is temporally compacted toward the trailing edge of the pulse, producing a blue broadening of the spectrum, and temporally stretched on the leading edge of the pulse, producing a red broadening of the spectrum.
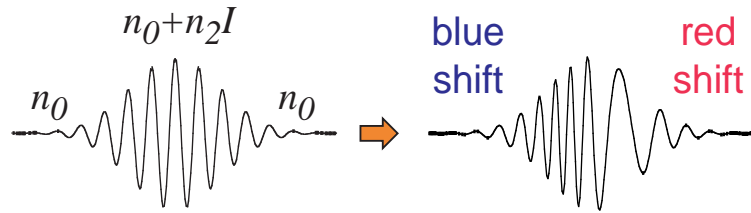
Figure 2.2 Schematic representation of self-phase modulation. The intensity-dependent refractive index retards the electric field at the temporal peak of the pulse, producing red broadening on the leading edge and blue broadening on the trailing edge of the pulse.

More quantitatively, we can describe the extent of the spectral broadening due to self-phase modulation by considering the propagation of an optical pulse through a medium with a refractive index that obeys Eqn. (2.12). In the slowly-varying envelope approximation, the electric field of the pulse has the form

$$E(z,t) = A(z,t)e^{i(kz-\omega t)} + \text{c.c.}$$

$$(2.15)$$

14

where $A(z,t)$ is the slowly-varying envelope of the laser pulse. The intensity of the pulse is given by $I(t) = (n_0 c / 2\pi)|A(z,t)|^2$. After propagating through a material of length L, the pulse acquires a phase, ϕ, given by:

$$\phi = (kL - \omega t)$$
$$= \frac{\omega L}{c}(n_0 + n_2 I(t)) - \omega t$$

(2.16)

The instantaneous frequency, $\omega(t)$, which is given by the negative of the time derivative of the phase, has the form:

$$\omega(t) = \omega - \frac{n_2 \omega L}{c} \frac{\partial}{\partial t} I(t)$$

(2.17)

The instantenous frequency is red (blue) shifted on the leading (trailing) edge of the pulse where the derivative of the intensity is positive (negative), in agreement with the qualitative picture discussed above.

2.2.4   White-light generation and other propagation effects

In addition to self-phase modulation and self-focusing, there are several other self-action effects that play a role in femtosecond pulse propagation in transparent materials. For example, just as the phase velocity of the pulse becomes intensity dependent, so can the group velocity of the pulse effectively depend on laser intensity. The group velocity is slower for higher laser intensity, causing a change in the pulse envelope, and the development of a steep, shock-like edge at the rear of the laser pulse. This effect, known as self-steepening, is illustrated in Figure 2.3.

15
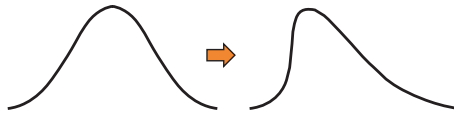
Figure 2.3 Self-steepening of a short laser pulse. An intensity-dependent group velocity causes the peak of the pulse envelope to slow down relative to the leading and trailing edges, producing an optical shock at the trailing edge.

One of the most dramatic examples of the complexity of the interaction between ultrashort laser pulses and transparent materials is white-light continuum generation. When an ultrashort laser pulse with sufficient power is weakly focused into a transparent material, it is transformed into a white-light pulse. The spectrum of the pulse broadens dramatically, as schematically indicated in Figure 2.4.
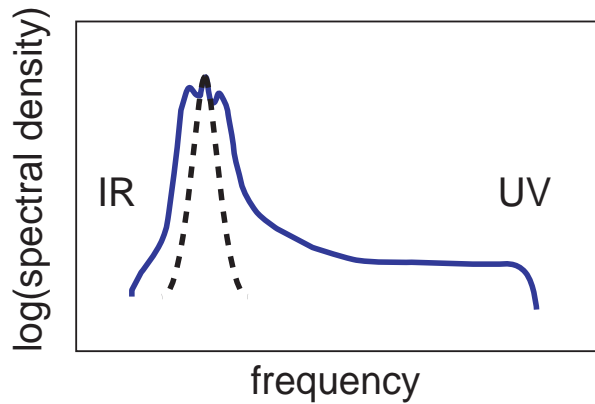
Figure 2.4 Sketch of the typical shape of a white-light continuum spectrum generated by loosely focusing an ultrashort, infrared laser pulse with sufficient power into a transparent material. The dashed line indicates the unbroadened spectrum.

Although it is widely used, the mechanism for generating the continuum remains largely unknown and misunderstood. In Chapter 5, we explore continuum generation and the role of effects such as self-steepening in detail.

2.3   Nonlinear ionization

In a pure transparent material, there is no linear absorption of the incident laser light. If the laser intensity is high enough, however, electrons can be promoted from the valence band to the conduction band of the material by nonlinear processes, depositing laser energy into the material. There are two classes of nonlinear excitation mechanisms, both reviewed in this section, that play a role in this absorption, photoionization and avalanche ionization. The plasma formed by this nonlinear excitation also affects the propagation of the laser pulse. These effects are discussed in Sections 2.3.3 and 2.3.4. In Chapter 3, we present measurements that identify the relative role of different nonlinear ionization

mechanisms for intense femtosecond pulses of different wavelength in materials with different band gap.

2.3.1   Nonlinear photoionization

Photoionization refers to direct excitation of the electron by the laser field. Because a single photon of visible light does not have enough energy to excite an electron in a transparent material from the valence to the conduction band, multiple photons must cooperate together to excite the electron. Depending on the laser frequency and intensity, there are two different regimes of photoionization, the multiphoton ionization regime and the tunneling ionization regime. Keldysh showed that both multiphoton and tunneling could be described within the same framework.[11] The conceptual picture for these two mechanisms is very different, however, so the distinction remains useful. Furthermore, the approximations used to calculate the ionization rates are very different in the two regimes.

For strong laser fields and low laser frequency, nonlinear photoionization is a tunneling process. In tunneling ionization, the electric field of the laser suppresses the Coulomb well that binds a valence electron to its parent atom. If the electric field is very strong, the Coulomb well can be suppressed enough that the bound electron tunnels through the short barrier and becomes free, as shown schematically in the left panel of Figure 2.5.

γ < 1.5
tunneling

γ ~ 1.5
intermediate

γ > 1.5
MPI
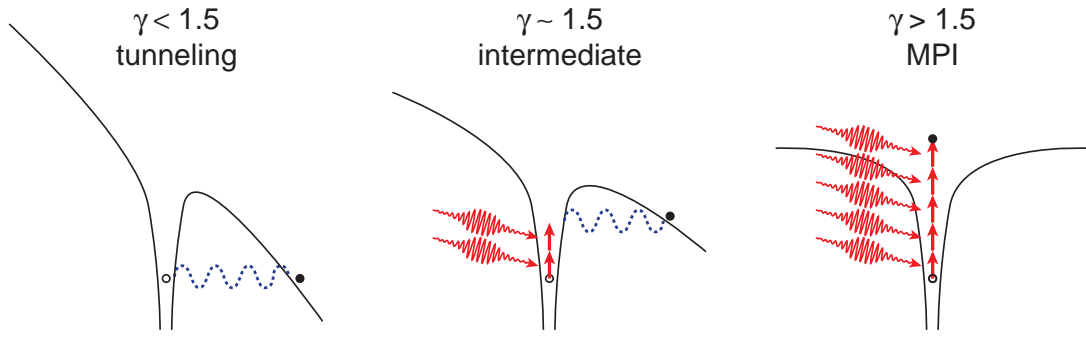
Figure 2.5 Schematic diagram of photoionization for different values of the Keldysh parameter. In a solid material, the electron is promoted from the valence to the conduction band, rather than ionized as these diagrams of atomic potentials suggest.

For higher laser frequencies (but not high enough that single photon absorption can occur) nonlinear ionization is usually described in terms of the simultaneous absorption of several photons by an electron, shown in the right panel of Figure 2.5. To be promoted from the valence to the conduction band by this multiphoton absorption, the electron must absorb enough photons so that the number of photons absorbed times the photon energy is greater than the band gap of the material.

The transition point between multiphoton ionization and tunneling ionization was worked out by Keldysh.[11] The adiabatic parameter, also known as the Keldysh parameter, γ, is defined as

$$\gamma = \frac{\omega}{e}\left[\frac{mcn\varepsilon_0 E_g}{I}\right]^{1/2} \tag{2.18}$$

where ω is the laser frequency, I is the laser intensity at the focus, m and e are the reduced mass and charge of the electron, c is the velocity of light, n is the refractive index of the material, E_g is the band gap of the material, and ε_0 is the permitivity of free space. When the Keldysh parameter is larger (smaller) than about 1.5, photoionization is a

multiphoton (tunneling) process. In the intermediate regime, one may think of the photoionization as being a mix between tunneling and multiphoton ionization as depicted in the middle panel of Figure 2.5.

The photoionization rate depends strongly on the laser intensity. In the multiphoton ionization regime, the rate is $P(I)_{MPI} = \sigma_k I^k$ where σ_k is the multiphoton absorption coefficient for k-photon absorption.[12] The number of photons required is determined by the smallest k which satisfies the relation $k\hbar\omega \geq E_g$. The tunneling rate, on the other hand, scales more weakly with the laser intensity than the multiphoton rate.

Figure 2.6 shows the photoionization rate and Keldysh parameter as a function of laser intensity for 800-nm light in fused silica (7.5 eV band gap). The dashed, dotted, and solid lines represent the photoionization rate for mulitphoton ionization only (Eqn. 40 in Ref. [11]), tunneling ionization only (Eqn. 41 in Ref. [11]), and the full Keldysh expression (Eqn. 37 in Ref. [11]), respectively. The multiphoton only rate and the tunneling only rate agree with each other and with the complete rate for a Keldysh parameter of about 1.5. The rate based on tunneling only agrees with the complete formula up to a Keldysh parameter of just over 1.5, then overestimates the rate. Similarly, the rate based on multiphoton ionization only agrees with the full formula for Keldysh parameters down to just below 1.5, then underestimates the rate. Simulations for other laser wavelength and material band gap consistently show this very abrupt transition from a multiphoton to tunneling regime at a Keldysh parameter of about 1.5.

Some recent experiments have called Keldysh's theory into question. Lenzner, *et al.* found that they could not account for the pulse duration dependence of the surface damage threshold of fused silica with the ionization rates predicted by Keldysh, and that

the multiphoton ionization coefficients that best fit their data were several orders of magnitude smaller than those predicted by Keldysh's theory.[13] This discrepancy could be the result of electron dephasing due to frequent phonon scattering.[14] Other researchers, however, have successfully fit their data using rates from Keldysh's theory.[15, 16] More experimental and theoretical work is necessary to resolve this issue.
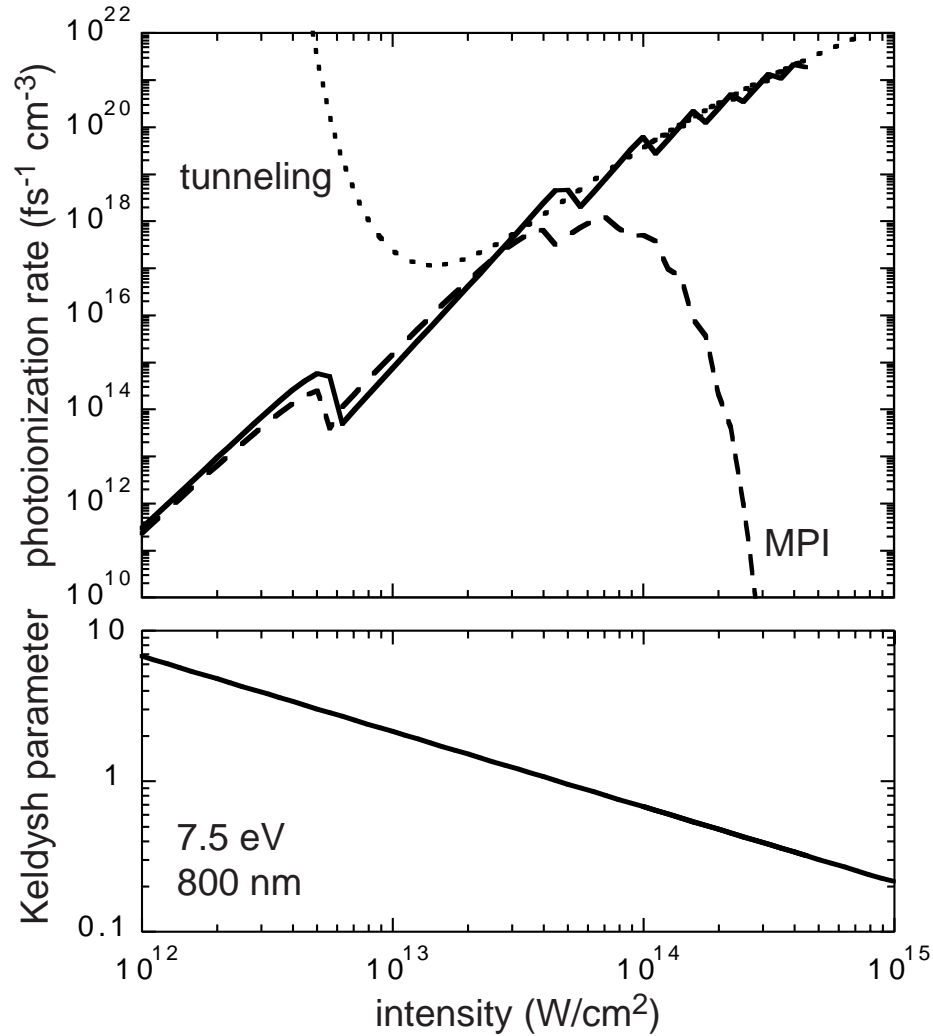
Figure 2.6 Photoionization rate and Keldysh parameter as a function of laser intensity for 800-nm light in fused silica (7.5-eV band gap). The solid line represents the photoionization rate based on the full expression from Keldysh (Eqn. 37 in Ref. [11]), the dashed line represents the multiphoton ionization rate, and the dotted line represents the tunneling ionization rate. Note that the multiphoton and tunneling rates overlap around a Keldysh parameter of 1.5.

2.3.2   Avalanche ionization

Avalanche ionization involves free-carrier absorption followed by impact ionization. An

electron already in the conduction band of the material linearly absorbs several laser

photons sequentially, moving to higher energy states in the conduction band, illustrated in the left panel of Figure 2.5. In order to conserve both energy and momentum, when the electron absorbs a laser photon, it must transfer momentum by absorbing or emitting a phonon or by scattering off an impurity.[17] For electrons high in the conduction band, the deformation potential scattering time is approximately 1 fs, so frequent collisions make free-carrier absorption efficient.[18] After the sequential absorption of n photons, where n is the smallest number which satisfies the relation $n\hbar\omega \geq E_g$, the electron's energy excedes the conduction band minimum by more than the band gap energy. The electron can then collisionally ionize another electron from the valence band, as illustrated in the right panel of Figure 2.7. The result is two electrons near the conduction band minimum, each of which absorb energy through free-carrier absorption and can subsequently impact ionize more valence band electrons. As long as the laser field is present, the electron density, N, in the conduction band thus grows according to

$$\frac{dN}{dt} = \eta N$$

(2.19)

where η is the avalanche ionization rate.
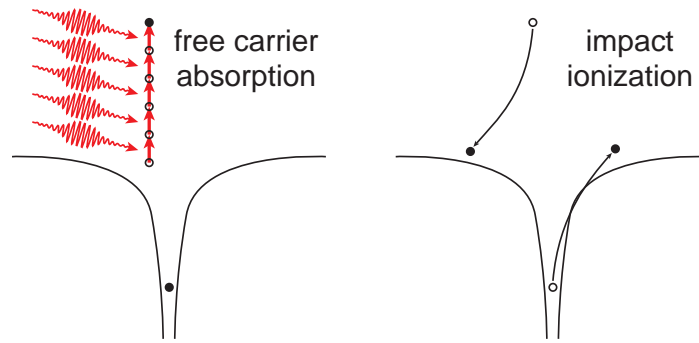
Figure 2.7 Schematic diagram of avalanche ionization. An initially free electron linearly absorbs several laser photons through free-carrier absorption, then impact ionizes another electron. As in Figure 2.5 the electrons are promoted from the valence to the conduction band in a solid rather than ionized as is suggested by the atomic potentials.

Avalanche ionization requires some seed electrons to already be in the conduction band of the material. These initial electrons are provided either by thermally excited carriers, by easily ionized impurity or defect states, or by carriers that are directly photoexcited by multiphoton or tunneling ionization.

Stuart, *et al.* developed a model of avalanche ionization in which the avalanche rate depends linearly on the laser intensity (i.e. $\eta = \alpha I$, where α is the avalanche ionization coefficient).[15] Heating of the electrons in the conduction band is taken into account using what is basically a Drude model but with the electron energy dependence of the conductivity included. The model also makes the flux doubling approximation, which states that an electron in the conduction band impact ionizes an electron from the valence band as soon as it has enough energy to do so. In other words, the model assumes there are no electrons in the conduction band with energy higher than the conduction band minimum plus the band gap energy (at least until the material is fully ionized, after which further electron heating can occur). Stuart's model also assumes that the energy

distribution of electrons in the conduction band does not change shape as the electron density grows. Recently, some researchers have called this model into question.[14, 19] Thornber, for example, predicts an avalanche rate that depends on the square root of the laser intensity.[20] As for photoionization, more experimental and theoretical work is necessary to resolve this dispute.

2.3.3   Free-carrier absorption by the plasma

The electron plasma formed by multiphoton and avalanche ionization can strongly absorb laser energy when the plasma density becomes high enough. The absorption of this plasma is easily understood using the Drude model. If the plasma density, N, grows until the plasma frequency, given by

$$\omega_p = \left[\frac{Ne^2}{\varepsilon_0 m}\right]^{\frac{1}{2}}$$

(2.20)

reaches the laser frequency, then the absorption becomes very efficient. The absorption coefficient is given by

$$\kappa = \frac{\omega_p^2 \tau}{c(1 + \omega^2 \tau^2)}$$

(2.21)

where ω is the laser frequency, and τ the the phemenological Drude scattering time (usually around 0.2 fs).[17]

Figure 2.8 shows the absorption depth of the plasma as a function of plasma density for 800-nm radiation. For a plasma density of about 10^{21} cm^{-3}, the absorption depth is about 1 µm. For the tight focusing typical of the experiments described in this thesis, the Raleigh range (1/2 of the confocal parameter) is on the order of a micrometer. Thus, if the plasma produced by the nonlinear ionization mechanisms discussed in the

25

previous sections reaches a density of about 10^{21} cm^{-3}, we expect that a large fraction of

the laser pulse energy will be absorbed in the focal volume. As we discuss in Section 2.4,

it is this deposition of laser energy that leads to permanent damage.
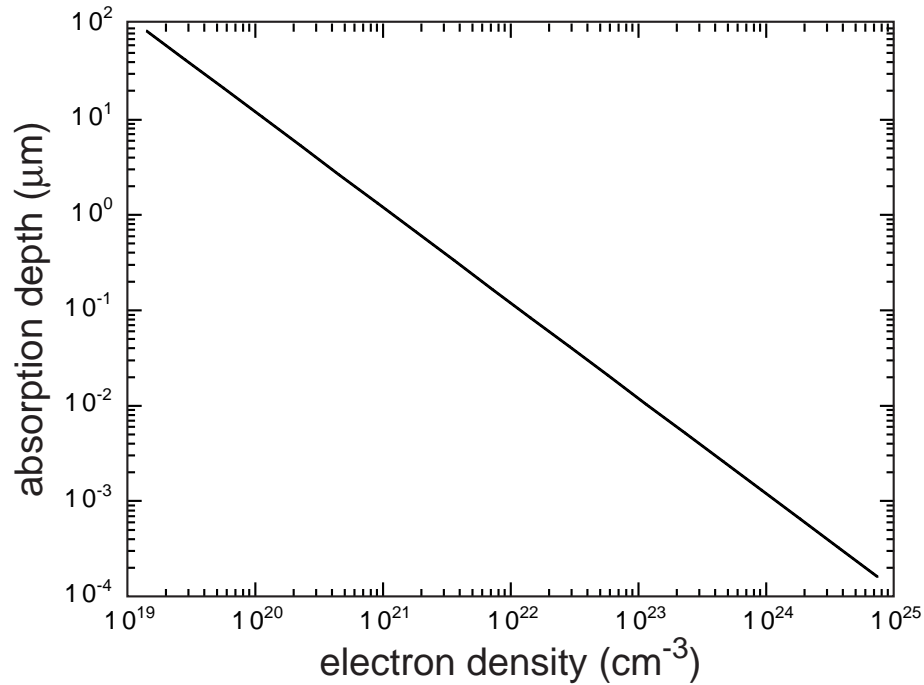
Figure 2.8 Absorption depth for 800-nm light in a Drude plasma as a function of plasma density.

2.3.4   Plasma defocusing

In addition to being strongly absorbing at high density, the plasma formed by nonlinear

ionization can have a defocusing effect on the laser pulse because the free electrons

contribute negatively to the refractive index. The spatial distribution of the electron

density is highest in the center of the beam and decreases radially outward because of the

spatial intensity profile of the beam. This spatial distribution of the electron plasma forms a negative lens which defocuses the pulse.

This plasma defocusing is the mechanism that stops self-focusing. As the laser intensity grows during self-focusing, free electrons are produced by nonlinear ionization. When the plasma density reaches $10^{17} - 10^{18}$ cm^{-3}, the negative contribution to the refractive index due to the plasma balances the nonlinear index, n_2I.[21, 22] As we will see in Chapter 5, this mechanism for limiting the intensity achieved in a self-focus plays an important role in continuum generation.

2.4 Material damage

If enough laser energy is deposited into the material by the nonlinear absorption mechanisms described above, permanent damage is produced. In this section, we discuss the qualitative differences in the damage mechanisms for long and short laser pulses. In Chapter 4, we explore in detail the morphology of the damage produced in bulk transparent materials with 100-fs laser pulses.

2.4.1   Long pulse

For pulse durations longer than a few tens of picoseconds, there is a significant transfer of energy from the laser-excited electrons to the lattice on the time scale of the pulse duration. The energy transferred to the lattice is carried out of the focal volume by thermal diffusion. Damage occurs when the temperature of the material in the irradiated region becomes high enough for the material to melt or fracture.[16] Energy is deposited into the material by the laser pulse and is transported out of the irradiated region by

thermal diffusion, thus it is the relative rate of energy deposition and thermal diffusion that determines the damage threshold. Simple calculations show that, in this case, the threshold fluence for optical damage will scale as the square root of the pulse duration.[23] Soileau, *et al.* were the first to observe a departure from this dependence for pulses shorter than 10 ps.[24]

For long pulse damage, the source of the initial seed electrons in the conduction band that absorb laser energy by free-carrier absorption is very important. Avalanche ionization is very efficient for long laser pulses because the long pulse duration allows more time for exponential growth of the electron density. Because avalanche ionization is so efficient, the laser intensity required to produce damage for pulse durations longer than a few tens of picoseconds is not high enough to have a high probability of directly photoionizing electrons. Therefore, either thermally excited electrons or impurity and defect states provide the initial electrons to seed the avalanche. A high concentration of easily ionized impurity electrons lowers the threshold for optical damage compared to that of the pure material, making determination of the intrinsic breakdown threshold difficult.

This dependence on impurity electrons in the conduction band also makes the threshold for optical breakdown and damage very statistical. A typical impurity concentration of electrons in the conduction band of a transparent solid is about 10^8 cm^{-3}. [18] A laser beam focused to a 10-μm diameter spot inside the material has a Raleigh range of about 75 μm, and therefore a focal volume of about 10^{-8} cm^3. Thus there is, on average, about one impurity electron in the conduction band of the material in a typical focal volume. Because these few seed electrons are so critical for the breakdown process

with long pulses, fluctuations in the number of seed electrons in the focal volume strongly affects the breakdown process. For a constant laser energy that is near the threshold, some laser shots will produce damage while others will not, depending on how many seed electrons were in the focal volume of each laser shot.

2.4.2 Short pulse

For pulses shorter than a few picoseconds, the conceptual picture of optical damage is simpler than for longer laser pulses. The nonlinear absorption occurs on a time scale that is short compared to the time scale for energy transfer to the lattice, decoupling the absorption and lattice heating processes.[15] Electrons in the conduction band are heated by the laser pulse much faster than they can cool by phonon emission, diffuse out of the irradiated volume, or recombine with their parent ion. As a result, the electron density grows through avalanche ionization until its plasma frequency approaches the critical plasma density.[15] As shown in Section 2.3.3 , this high density plasma strongly absorbs laser energy by free-carrier absorption. It is only after the laser pulse is gone that energy is transferred from the electrons to the lattice. This shock-like deposition of energy into the material, on a time scale much faster than the thermal diffusion time, leads to ablation of material on the surface or permanent structural change in the bulk.

For short laser pulses, photoionization plays an important role in the generation of conduction band electrons. Photoionization on the leading edge of the laser pulse provides the seed electrons for avalanche ionization during the rest of the pulse.[15] This self-seeded avalanche makes short-pulse breakdown less dependent on defects in the material than long-pulse breakdown and therefore makes the threshold for short-pulse damage very deterministic.[25] For very short laser pulses, photoionization can dominate

avalanche ionization and produce a sufficient plasma density to cause damage by itself.[15]

Damage produced by pulses in the femtosecond range is far more regular from shot to shot and more confined than with longer pulses.[26] The regularity from shot to shot is due to photoionization seeding the electron avalanche, as discussed above. Also, because short pulses require less energy than longer pulses to reach the intensity necessary to produce optical breakdown, they deposit less energy in the material. Less energy deposition leads to more precise ablation or bulk material modification. This deterministic breakdown and damage near threshold and controllable material alteration make femtosecond lasers an ideal tool for micromachining. In Chapter 7, several micromachining applications in solid transparent materials and in transparent biological samples are presented.

2.5 Ultrashort-pulse laser systems

Many advances have been made in ultrashort-pulse laser systems in recent years. Pulse durations as short as 5 fs,[27] laser energies greater than 100 J,[28] and average powers greater than 10 W[29] have all been demonstrated. In addition to having more impressive specifications, modern femtosecond laser systems are more reliable and easier to use than the organic dye-based femtosecond lasers used previously. Much of this progress can be attributed to the use of Ti:Sapphire as the gain medium.

For a laser to produce a femtosecond pulse, three essential elements must be present.[30] First, the gain medium must have a wide emission bandwidth. For the laser pulse to be short in time, it must be broad in frequency, and the gain medium has to

30

produce these frequencies. Second, there must be some mechanism to compensate for the dispersion in the laser cavity. Because the group velocity in the optics (and even the air) inside a laser cavity is frequency dependent, an initially short pulse tends to spread in time because different frequency components travel at different velocity. Typically a prism pair is used to compensate for this dispersion in the laser cavity, although recent advances in mirror coating technology allow the dispersion compensation to be taken care of in the optics themselves.[31] Finally, there must be some mechanism that makes the laser run in a pulsed, as opposed to a continuous wave mode. Essentially, all the different frequency components supported by the laser cavity (in terms of gain and dispersion compensation) must add constructively to produce a pulse, a process known as mode-locking.[30]

For long pulse lasers, mode-locking can be achieved by inserting an active modulator into the laser cavity that makes the gain in the laser cavity exceed the loss for only a short time, ensuring that the laser produces a pulse. No active modulator can switch fast enough to produce a femtosecond pulse, however, so the gain (or loss) of the cavity must be modulated in some other way. In Ti:Sapphire lasers, this modulation is accomplished by the so called Kerr-lens mechanism.[32] Briefly, weak self-focusing of the pulse in the gain crystal reduces the transverse size of the beam so that there is better overlap with the optically pumped gain region. It is thus energetically favorable for the laser to run pulsed as opposed to continuous wave (indeed, in a well-aligned Ti:Sapphire laser the average power will go up when the laser is mode-locked).

Typical Ti:Sapphire laser oscillators produce 20-fs, 5-nJ, 800-nm pulses at repetition rate of about 90 MHz. For many applications, higher laser energy is desirable.

Amplification of femtosecond laser pulses requires care, however. As the laser energy grows, the nonlinear optical effects discussed in the first part of this chapter occur in the amplification chain, degrading the pulse. In extreme cases, nonlinear absorption of laser energy by the optics in the amplification chain could cause permanent damage. To avoid these nonlinear optical effects, but still pump more energy into the pulse, Mourou and co-workers devised the clever strategy of chirped-pulse-amplification.[33] The pulse from the oscillator is first stretched temporally, then amplified, and finally recompressed. Because the pulse is long during the amplification stage, nonlinear effects and damage to optics are avoided. The pulse is typically stretched and compressed by arranging for geometrically longer path lengths for different frequency components of the pulse using diffraction gratings.[28] Amplification usually occurs in either a second laser cavity into which a selected number of stretched pulses are switched (regenerative amplification) or by passing a selected number of stretched pulses multiple times through the pumped region of gain medium using clever mirror arrangements (multi-pass amplification).[28] Depending on the repetition-rate, different laser energies are achieved. Typical numbers are 1 μJ at 100 kHz, 1 mJ at 1kHz, and 100 mJ at 10 Hz.

The experiments described in this these were performed on several lasers. A regeneratively amplified Ti:Sapphire laser producing 110-fs, pulses with 0.5 mJ of energy was used for the threshold measurements, the continuum experiments, the dynamics measurements, and for much of the damage morphology work. The oscillator-only micromachining was carried out on a modified laser oscillator described in Section 4.3.2. Several experiments were also performed on a multi-pass laser producing 30-fs, 0.5-mJ pulses.

References

1. J. D. Jackson, *Classical Electrodynamics* (Wiley, New York, 1975).

2. M. Born and E. Wolf, *Principles of Optics* (Pergamon, Oxford, 1980).

3. R. W. Boyd, *Nonlinear Optics* (Academic Press, Boston, 1992).

4. R. L. Fork, C. H. Brito Cruz, P. C. Becker, and C. V. Shank, *Opt. Lett.* **12**, 483 (1987).

5. N. Bloembergen, *Nonlinear Optics* (Benjamin, New York, 1965).

6. Y. R. Shen, *The Principles of Nonlinear Optics* (Wiley, New York, 1984).

7. J. A. Armstrong, N. Bloembergen, J. Ducuing, and P. S. Pershan, *Phys. Rev.* **127**, 1918 (1962).

8. J. H. Marburger, *Prog. Quantum Electron.* **4**, 35 (1975).

9. A. L. Gaeta, *Phys. Rev. Lett.* **84**, 3582 (2000), and references therein.

10. M. J. Soileau, W. E. Williams, N. Mansour, and E. W. van Stryland, *Opt. Eng.* **28**, 1133 (1989).

11. L. V. Keldysh, *Zh. Eksp. Teor. Fiz.* **47**, 1945 (1964) [*Sov. Phys. JETP* **20**, 1307 (1965)].

12. S. C. Jones, P. Braunlich, R. T. Casper, X.-A. Shen, and P. Kelley, *Opt. Eng.* **28**, 1039 (1989).

13. M. Lenzner, J. Krüger, S. Sartania, Z. Cheng, Ch. Spielmann, G. Mourou, W. Kautek, and F. Krausz, *Phys. Rev. Lett.* **80**, 4076 (1998).

14. D. Du, X. Liu, and G. Mourou, *Appl. Phys. B* **63**, 617 (1996).

15. B. C. Stuart, M. D. Feit, S. Herman, A. M. Rubenchik, B. W. Shore, and M. D. Perry, *Phys. Rev. B* **53**, 1749 (1996).

16. B. C. Stuart, M. D. Feit, S. Herman, A. M. Rubenchik, B. W. Shore, and M. D. Perry, *J. Opt. Soc. Am. B* **13**, 459 (1996).

17. P. Y. Yu, and M. Cardona, *Fundamentals of Semiconductors* (Springer-Verlag, Heidelberg, Germany, 1996). p. 296.

18. N. Bloembergen, *IEEE J. Quantum Electron.* **QE-10**, 375 (1974).

19. A.-C. Tien, S. Backus, H. Kapteyn, M. Murnane, and G. Mourou, *Phys. Rev. Lett.* **82**, 3883 (1999).

20. K. K. Thornber, *J. Appl. Phys.* **52**, 279 (1981).

21. E. Yablonovitch and N. Bloembergen, *Phys. Rev. Lett.* **29**, 907 (1972).

22. A. Brodeur, Ph.D. thesis, University Laval (1997).

23. R. M. Wood, *Laser Damage in Optical Materials* (Hilger, Boston 1986).

24. M. J. Soileau, W. E. Williams, E. W. Van Stryland, T. F. Boggess, and A. L. Smirl, *Natl. Bur. Stand. (U.S.) Spec. Publ.* **669**, 387 (1984).

25. D. Du, X. Liu, G. Korn, J. Squier, and G. Mourou, *Appl. Phys. Lett.* **64**, 3071 (1994).

26. E. N. Glezer, M. Milosavljevic, L. Huang, R. J. Finlay, T.-H. Her, J. P. Callan, and E. Mazur, *Opt. Lett.* **21**, 2023 (1996).

27. U. Morgner, F. X. Kartner, S. H. Cho, Y. Chen, H. A. Haus, J. G. Fujimoto, E. P. Ippen, V. Scheuer, G. Angelow, and T. Tschudi, *Opt. Lett.* **24**, 411 (1999).

28. S. Backus, C. G. Durfee III, M. M. Murnane, and H. C. Kapteyn, *Rev. Sci. Instrum.* **69**, 1207 (1998), and references therein.

29. A. Galvanauskas and M. E. Fermann, *Technical Digest: Converence on Lasers and Electro-Optics*, postdeadline paper CPD3 (2000).

30. E. P. Ippen, *Appl. Phys. B* **58**, 159 (1994).

31. L. Xu, C. Spielmann, F. Krausz, and R. Szipöcs, *Opt. Lett.* **21**, 1259 (1996).

32. I. P. Christov, H. C. Kapteyn, M. M. Murnane, C. P. Huang, and J. P. Zhou, *Opt. Lett.* **20**, 309 (1995), and references therein.

33. D. Strickland and G. Mourou, *Opt. Commun.* **56**, 219 (1985).

Chapter 3

Non-linear ionization and optical breakdown

Laser-induced breakdown and damage to transparent materials has remained an active area of research for four decades. In this paper we review the basic mechanisms that lead to laser-induced breakdown and damage and present a summary of some open questions in the field. We present a method for measuring the threshold intensity required to produce bulk, as opposed to surface, breakdown and damage. Using this technique, we measure the material band gap and laser wavelength dependence of the threshold intensity for bulk damage using femtosecond laser pulses. Based on these thresholds, we determine the relative role of different nonlinear ionization mechanisms for different laser and material parameters.

3.1   Introduction

Laser-induced breakdown and damage in transparent materials have been studied since the advent of high-power pulsed lasers.[1] Despite this long history, much still remains to be learned about the fundamental science of high-intensity laser interactions with transparent materials. The availability of laser pulses with femtosecond duration allows

materials to be subjected to higher laser intensity than ever before, opening the door to the study of laser-material interactions in a new regime. From a practical point of view, this high laser intensity offers new challenges and provides new opportunities. The peak power in large laser systems is currently limited by the damage threshold of the optics in the laser chain.[2] Understanding the mechanisms responsible for optical damage may allow higher-damage threshold optics to be constructed for these laser systems. Additionally, in recent years, the structural alterations produced in transparent materials by ultrashort laser pulses have been used for micromachining.[3 - 7] A better grasp of the nonlinear ionzation mechansisms at play may allow for higher-precision micromachining and more control over the changes induced in the material.

In a pure transparent material, there is no linear absorption of the incident laser light. For optical breakdown and material damage to occur, a nonlinear absorption mechanism must deposit laser energy into the material by promoting electrons from the valence band to the conduction band. The two classes of nonlinear excitation mechanisms that play a role in this absorption, photoionization and avalanche ionization, were discussed in Section 2.3. If enough laser energy is deposited into the material by these nonlinear absorption mechanisms, permanent damage is produced.

Although there is a basic understanding of the important absorption mechanisms, there are several open questions that need to be addressed. Most notably, the validity of Keldysh's theory[8] for photoionization needs to be determined, and the scaling of the avalanche ionization rate with laser intensity needs to be established. From an experimental point of view, these issues can be addressed by measuring the breakdown threshold as a function of material and laser parameters. The pulse duration dependence

37

of the damage threshold has been extensively explored in fused silica for infrared laser pulses.[9 - 11, 13, 17 - 19] Some groups have examined the effect of material band gap[9] and laser wavelength,[10] but a systematic study has not yet been conducted. More experiments are needed to quantitatively clarify the relative role of different ionization mechanisms for different laser and material parameters. Such data will hopefully help resolve the debates mentioned above, and spur renewed theoretical interest in the subject.

Most recent experiments in the femtosecond regime have measured the threshold for damage to the front surface of the sample. It has not been established that these surface thresholds are the same as bulk thresholds or if they are lowered by surface effects. The surface could have some contaminants or surface states which are more easily ionized than bulk material. The number of photons needed to ionize these states could, for instance, be smaller than that required to ionize the bulk. These easily ionized states could provide seed electrons for avalanche ionization, lowering the threshold. In fact, von der Linde, *et al.* concluded that the surface thresholds they measured are most likely lowered by contamination or surface imperfections.[20] While the surface damage threshold is relevant for optimizing the damage threshold of first-surface optics and for surface micromachining, the theoretical work to date, however, does not take into account any surface effects, so establishing the importance of these effects through a systematic study of surface and bulk thresholds should be carried out.

In addition to establishing the correspondence between surface and bulk damage thresholds, one should establish the correspondence between the many different criteria that have been used to define the damage threshold. Du, *et al.* monitored the change in

transmission of the laser pulse and the emission of light due to recombination of the plasma. Each spot in the sample was irradiated with only one laser pulse.[17] In contrast, Stuart, *et al*. optically inspected samples that had been irradiated by 600 pulses under a Nomarski microscope.[10, 11] Lenzner, *et al*. measured the volume of ablated material for 50 above-threshold pulses incident on each spot in the sample and extrapolated to zero ablated volume to obtain a threshold.[9] Varel, *et al*. used several ex situ techniques including Nomarski optical microscopy, atomic force microscopy, and scanning electron microscopy to determine a threshold for single-shot ablation.[18] Tien, *et al*. used Nomarski microcopy of samples irradiated by single pulses to determine the threshold.[13] Li, *et al*. measured the plasma emission from multiple shots on a single spot in the sample.[21] This variety of techniques makes comparison between the results of different groups difficult.

In addition to reconciling the different diagnostics used to determine whether or not damage is produced, the effect of multiple laser pulses hitting one spot in the sample must be addressed. Recently, several groups have reported that the threshold for multiple-shot experiments is lower than for single-shot experiments by a factor of two to four for femtosecond laser pulses due to incubation effects.[22, 23]

In this chapter, we present measurements of the bulk damage threshold for femtosecond pulses in materials of four different band gaps with two different laser wavelengths. We use a technique for determining the bulk damage threshold that avoids self-focusing and aberrations, allowing the laser intensity at the focus to be accurately determined. We measure the intensity threshold for bulk material damage and find that, for fused silica, the bulk thresholds for femtosecond pulses agree very well with the

thresholds for surface ablation found by other groups. The bulk threshold we measure in CaF_2, however, is larger than the previously measured surface threshold by about a factor of two.[18] The scaling of the intensity thresholds with laser wavelength and band gap suggests that avalanche ionization is responsible for producing most of the conduction band electrons for large band gap materials, while photoionization is more important for low band gap materials. Furthermore, we find that the photoionization by 400-nm pulses is best characterized as multiphoton absorption, while for 800-nm pulses the absorption is in the intermediate regime between multiphoton and tunneling ionization.

3.2 Measuring bulk ionization thresholds

Early experiments on optical breakdown thresholds in the nanosecond and picosecond regime were done in bulk material.[12, 24 - 27] The results of these experiments are, however, often confused by the effects of self-focusing in the material.[26] More recent experiments on optical breakdown thresholds using femtosecond pulses have been carried out on surfaces. Researchers deliberately avoided bulk measurements because of the complications associated with self-focusing, dispersion, and self-phase modulation. These effects modify the spatial and temporal profile of the laser pulse, making it difficult to determine the laser intensity to which the material is exposed. As mentioned above, however, it is not clear how well existing models, which do not take into account surface effects, apply to the threshold for surface damage. In this section, we present a method for measuring the intensity threshold for bulk damage that avoids the complications due to self-focusing and focusing aberrations.

3.2.1 Complications with bulk threshold measurements: self-focusing

The primary difficulty with accurately determining the threshold for optical breakdown and damage in the bulk of a transparent material is correctly determining the laser intensity at the observed threshold for damage. One measures the laser pulse energy, pulse duration, and beam profile outside the sample. If propagation through the sample did not affect any of these parameters, and if the focusing were aberration-free, then the peak laser intensity is simply related to the quantities that are measured. The high peak power of the laser pulses, however, induces nonlinear propagation effects which strongly distort the spatial and temporal profile of the laser pulse in a manner that is difficult to predict or model.[28, 29] For extremely short pulses, the dispersion in the material has to be taken into account to ensure the pulse is short at the focus inside the material.

Self-focusing, discussed in Section 2.2.2, is the most important nonlinear propagation effect that we must consider when determining bulk ionization thresholds. To avoid excessive self-focusing in the material, we make use of the fact that while the threshold for optical breakdown and damage depends on the laser intensity, the threshold for self-focusing depends on peak power.[28] If the laser pulse is tightly focused into the material using an external lens, the intensity for optical breakdown can be reached with a power that is below the critical power for self focusing. This technique of tight external focusing was first devised by Yablonovitch[30] and is discussed by Bloembergen.[12]

In typical transparent solids, the critical power is on the order of 1 MW,[31, 32] and the intensity threshold for bulk optical breakdown using a femtosecond laser pulse is about 10^{13} W/cm^2.[5] We can crudely estimate how tightly we must focus the laser beam

to produce breakdown with power below the critical power by assuming the beam has a flat-top spatial profile. We then have that

$$I = \frac{P}{\pi(d/2)^2} \tag{3.1}$$

where d is the diameter of the laser spot at the focus, P is the peak power of the laser pulse, and I is the laser intensity. We find that the laser must be focused to a spot size smaller than 3.6 μm to achieve breakdown with a power that is below the critical power. With high numerical aperture (NA) microscope objectives, focal spots of well under 1 μm can be achieved, allowing the threshold for optical breakdown to be measured with powers that are more than an order of magnitude below the critical power. At these low powers, the correction due to self-focusing is small, allowing the spot size of the laser at the focus to be calculated with confidence. Thus the intensity of the laser pulse at the focus can be known, allowing a straightforward interpretation of the wavelength, pulse duration, and band gap dependence of bulk breakdown thresholds.

3.2.2   Complications with bulk threshold measurements: aberrations

Tight external focusing can eliminate the ambiguity in the peak laser intensity inside the material due to self-focusing, but it also brings its own set of problems. With such tight focusing, it is difficult to directly measure the spot size of the laser beam inside the material. Instead, one must calculate the spot size based on the laser beam and focusing lens parameters. Focusing visible light to a spot size under 1 μm, however, requires focusing angles that go well beyond the paraxial approximation.[33] As a result, focusing aberrations can severely distort the focal spot if care is not taken to minimize them. Here, we consider only beams that are incident at the center of the focusing lens and are parallel

42

to the optic axis of the lens. In this case, the most important aberration that must be considered is spherical aberration, although chromatic aberration can also play a for wide-bandwidth pulses.

Microscope objectives used in biological imaging are designed to focus well through a cover slip. They are corrected for all the primary aberrations if focused through 170 μm of glass with the appropriate refractive index ($n = 1.523$ at 589 nm) and Abbe number ($V = 59$) – one such glass is Corning 0211, a zinc-doped borosilicate glass. Because we are interested in investigating the breakdown threshold in materials with different band gap, and therefore different refractive index, we must evaluate how seriously the focus is degraded when focusing into materials with refractive indices different from that for which the objective is designed.

We modeled the effect of different refractive index materials with simple ray tracing. We reproduced the cone of converging rays produced by the microscope objective by assuming a perfect focus 170 μm beneath the surface of a cover slip and tracing rays back out of the cover slip. We then traced the cone back into a material with different refractive index, and varied the position of the material in and out of the cone to minimize the distortion of the focus. We find that for a 0.65-NA microscope objective one can find a focusing depth in a material with refractive index between 1.3 and 2.0 where the geometric spread of the rays is less than 100 nm. Because this size is significantly smaller than the diffraction-limited spot size, we take this small spread in the rays to indicate good focusing. The simulations predict that the laser spot size increases dramatically when the laser is not focused to within 10 μm of the optimal depth in the material for the 0.65-NA objective. For lower NA objectives, good focusing can be

achieved over a greater range of focusing depths and refractive indices. For objectives with NA higher than 0.65 it becomes very difficult to avoid aberrations in any material other than a cover slip. Consequently we avoid using objectives with greater than 0.65 NA in all materials other than Corning 0211.

To ensure diffraction-limited focusing when making measurements, we illuminate the back aperture of the microscope objective as uniformly as possible and completely fill it. The laser is focused into the sample at the best-focus depth determined from the simulations. The threshold for optical damage is measured and the focusing depth is slightly varied to make sure that the threshold is as low as possible, implying the best possible focusing. For microscope objectives with NA greater than about 0.5, we find that the threshold for optical damage increases dramatically when the laser is not focused at the optimal depth in the material, in agreement with the simulations. For the thresholds presented below, the laser is always focused at the depth in the sample where the threshold for producing damage is as low as possible.

3.2.3   Measuring with multiple numerical apertures

To further ensure that we can accurately determine the laser intensity required to produce optical breakdown, we make measurements using multiple microscope objectives with different NA.[5] To first approximation, the energy, E_{th}, required to reach the intensity threshold for optical breakdown, I_{th}, scales linearly with the laser spot size (i.e. $E_{th} \propto I_{th}/NA^2$). As discussed above, aberrations and self-focusing both cause a departure from this linear scaling. Aberrations play a role primarily at high numerical aperture (NA $\geq$ 0.4), where the paraxial approximation breaks down.[33] Self-focusing, on the other

hand, is more important at low numerical aperture (NA ≤ 0.65) because the amount of self-focusing depends on the ratio of the peak power of the laser pulse to the critical power for self-focusing for the material, and because more energy is needed to reach the breakdown intensity at low NA, resulting in a higher peak power.[28] We try to minimize aberrations using the procedures described above, and make the small correction in Eqn. (2.14) to the laser intensity to account for self-focusing. For diffraction-limited focusing in the presence of weak self-focusing, the energy, E_{th}, required to reach the breakdown intensity, I_{th}, is related to the NA of the objective by

$$E_{th} = \frac{I_{th}\tau\lambda^2}{\pi(NA)^2 + I_{th}\lambda^2/P_{cr}}$$ (3.2)

where τ is the laser pulse duration, λ is the laser wavelength, and P_{cr} is the critical power for self-focusing in the material.[5] We measure the energy required to produce breakdown in the material for several objectives with NA between 0.25 and 1.4, and fit the observed energy thresholds to Eqn. (3.2) with I_{th} as a free parameter.

Making measurements at multiple numerical apertures allows us to have very small corrections for self-focusing at high NA (where aberrations might be important), and to have low aberrations at low NA (where self-focusing becomes appreciable). If the energy threshold data over a range of numerical apertures is well fit by Eqn. (3.2), which assumes no aberrations and weak self-focusing, then we can feel confident that we have accurately determined the intensity threshold.

3.3   Experimental techniques

We have used several different techniques to determine the energy threshold for producing permanent bulk damage in transparent materials. The band gap and wavelength dependence data were aquired using a dark-field scattering technique that allows real-time assessment of the threshold. Real-time assessment is critical for bulk measurements because the laser must be focused at the optimal depth in the material for the threshold to be reliable. We first briefly describe post-mortem microscopy and transmission techniques for determining the threshold, then present a method for determining the critical power for self-focusing. Finally, we describe the dark-field scattering technique in detail. We find reasonable agreement between the three different techniques used to determine the threshold for damage.

3.3.1   Post-mortem microscopy

One method for evaluating whether or not optical damage is produced by laser irradiation is to produce arrays of structures made with varying laser energy and examine the array optically. Using differential interference contrast (DIC) microscopy with a 1.4-NA oil-immersion objective allows very small refractive index changes in the material on a sub-micrometer scale to be detected. Figure 3.1 shows a DIC optical micrograph of an array of structures in Corning 0211 produced using 110-fs laser pulses from a 1-kHz laser focused by a 1.4-NA oil-immersion objective. Each structure is made with a different combination of laser energy and number of laser shots on one spot in the sample. The energy increases from 6.6 to 66 nJ going from the left to the right of the image while the

46

number of shots incident on each spot increases from 2 to 5000 going from the top to the bottom of the image.
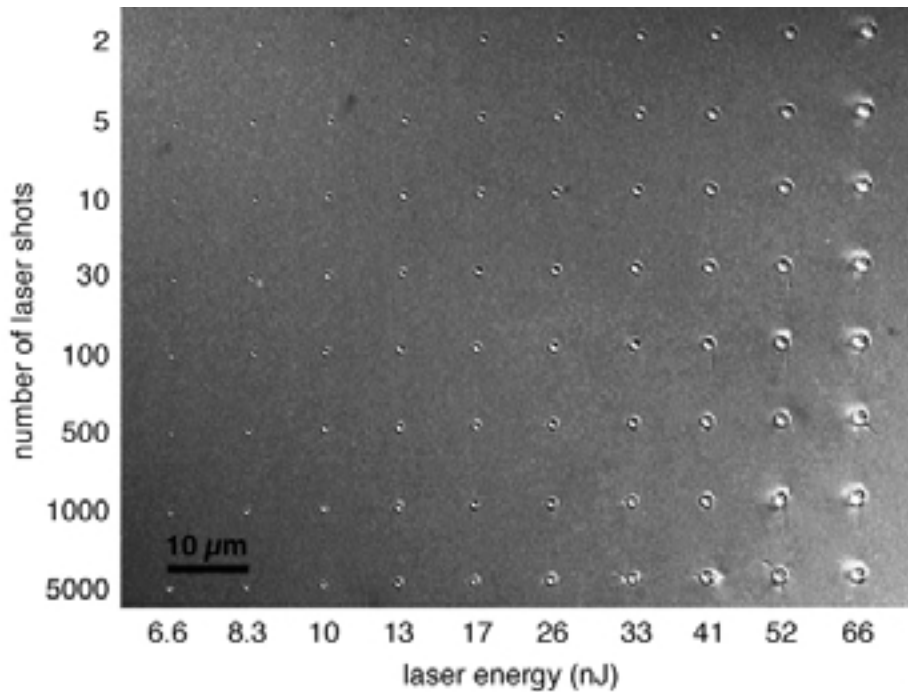
Figure 3.1 DIC optical micrograph of structures produced with various energy and various number of 110-fs laser pulses focused by a 1.4-NA microscope objective. The laser pulses are incident perpendicular to the plane of the image.

No material change is observed for a laser pulse energy below 6 nJ, regardless of the number of shots incident on one spot in the sample. While the damage produced using many 6.6-nJ pulses is easier to see than that produced by only a few 6.6-nJ pulses, we do always observe damage with a single pulse if we observe it with multiple pulses (i.e. the single- and multiple-shot threshold are the same for the laser, material, and focusing parameters used in Figure 3.1). In contrast, we do observe a decrease in the threshold for optically observable damage for increasing number of incident laser pulses when focusing with a 0.25-NA objective. Other researchers have also observed a decrease in

47

the surface ablation threshold of transparent materials with multiple-pulse irradiation.[22, 23] This lower threshold for multiple-shot damage indicates that incubation effects may be important. During multiple pulse irradiation, small changes (e.g. color centers) formed by the first few pulses may make it easier for later pulses to cause damage. More experiments on incubation effects are necessary to determine their importance in bulk and surface damage and to determine whether our observed NA dependence applies to other materials.

3.3.2   Transmission

Just as in measurements on the surface,[17] we can look for a drop in the transmission of the laser pulse due to absorption of significant laser energy by bulk material. Figure 3.2 shows the transmission of 110-fs laser pulses of different wavelength through a fused silica sample as a function of incident laser energy. The laser pulses are focused by a 0.65-NA microscope objective. The sharp drop in the transmission indicates the threshold for optical breakdown and damage to the material. We find an energy threshold of 20 nJ (25 nJ) for 400-nm (800-nm) wavelength pulses.
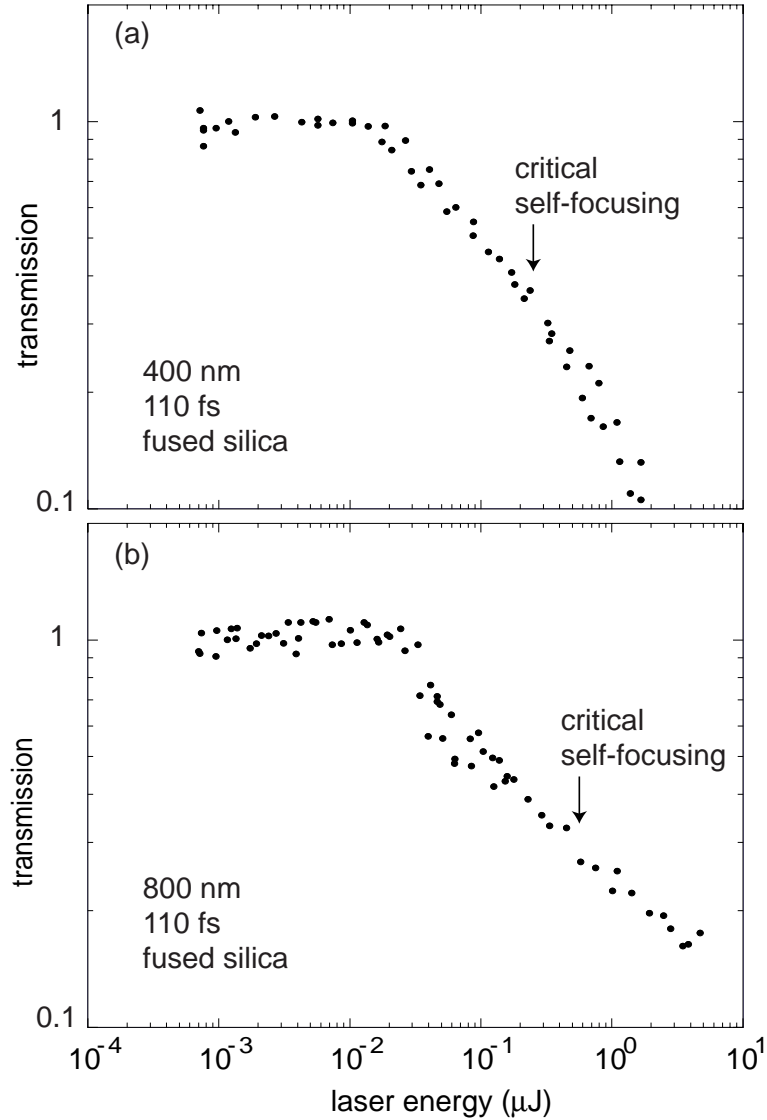
Figure 3.2 Transmission of 110-fs laser pulses focused by a 0.65-NA microscope objective with a) 400-nm and b) 800-nm wavelength through fused silica as a function of laser pulse energy. The energy corresponding to the critical power for self-focusing measured using the technique described in Section 3.3.3 is indicated on each graph.

3.3.3 Self-focusing threshold

The critical power for self-focusing must be known in order to make the correction in

Eqn. (2.14) to the laser intensity. To determine the critical power for self-focusing, we

measured the threshold for white-light continuum generation in various materials for a slow-focusing geometry (0.20-m focal length lens). It has been shown that, in such a geometry, the threshold for critical self-focusing corresponds to the threshold for white-light continuum generation.[31, 32] Note that self-focusing does not depend on the external focusing geometry, but only on the peak power; thus the critical self-focusing threshold is the same for fast and slow external focusing. The measured thresholds for critical self-focusing in fused silica (140 nJ for 400-nm pulses and 580 nJ for 800-nm pulses) are indicated in Figure 3.2. These energies are about an order of magnitude above the damage thresholds determined from the change in transmission, indicating that self-focusing does not play a dominant role in the damage formation.

Over the entire range of numerical apertures used in the measurements described in Section 3.4, breakdown is achieved in all materials with a laser power that is below the critical power for self-focusing. In Corning 0211, for example, self-focusing is negligible for 1.0 and 1.4 NA, while for 0.65, 0.45, and 0.25 NA self-focusing results in a 6, 10, and 20% decrease in spot size, respectively. In previous work, self-focusing played a more dominant role, complicating the determination of the threshold intensity for bulk optical breakdown.[26]

3.3.4 Dark-field scattering

For the material band gap and laser wavelength dependence of the damage threshold presented below, we used a dark-field light scattering technique, illustrated in Figure 3.3, to diagnose whether or not damage is produced in the material by laser irradiation. The primary advantage of this technique is that it is real-time, allowing us to minimize the

damage threshold by varying the focusing depth into the material, assuring that focusing aberrations are minimized.

A 110-fs pump pulse is focused into the material using a microscope objective with NA between 0.25 and 1.4. A He:Ne laser beam is used to probe the pumped region of the sample. The He:Ne is focused into the sample at a lower NA than the femtosecond beam, making the He:Ne spot size in the material larger than that of the femtosecond beam. The directly transmitted He:Ne light is collected by a microscope objective and blocked with a circular beam block whose size is chosen so it just blocks the full He:Ne beam. When damage is produced in the sample by the femtosecond laser beam, some of the He:Ne light scatters off this damaged region. Much of the He:Ne light is scattered into a larger cone angle than the directly transmitted light, and some fraction this light is collected by the microscope objective and focused around the beam block onto the detector.
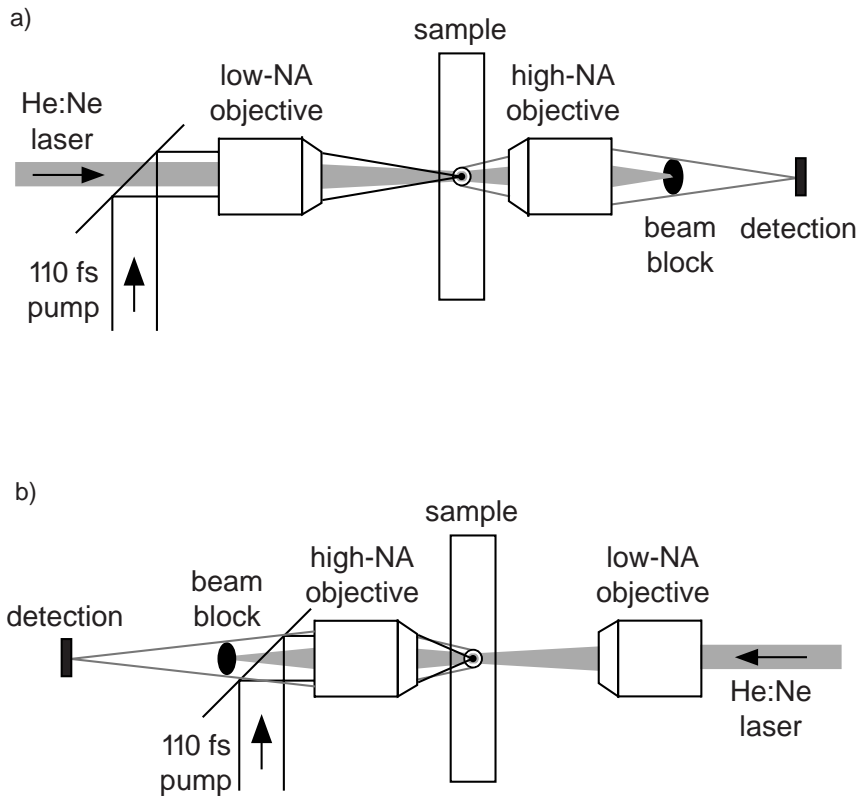
Figure 3.3 Dark-field scattering setup for determining the energy threshold for producing bulk damage in transparent materials using a) low-NA and b) high-NA objectives for focusing the femtosecond laser pulse.

It is critical that the He:Ne probe beam be focused at a lower NA than it is collected. The collection objective must have a higher acceptance angle than the cone angle of the unscattered He:Ne beam so that some of the light scattered by the damage spot is collected. The He:Ne should, however, still have a small enough spot size in the material that a large fraction of the beam scatters off the damage spot. Depending on the NA of the objective used to focus the femtosecond laser beam, we use two different setups. In Figure 3.3a, we show the setup used when the femtosecond beam is focused by an objective with NA lower than 0.45. The He:Ne beam co-propagates with the

femtosecond laser and is focused into the material with the same objective. The He:Ne beam underfills the back aperture of the objective and so has a larger spot size in the material than the femtosecond beam. A 0.65-NA objective is used to collect the scattered He:Ne light. Figure 3.3b shows the setup used when the femtosecond beam is focused by an objective with 0.45 NA or higher. The He:Ne probe counter-propagates with the femtosecond beam and is focused by a 0.25-NA objective into the sample. We do not completely fill the back aperture of the objective with the He:Ne beam. The objective which focuses the femtosecond beam also collects the scattered He:Ne light. A dichroic mirror transmits the He:Ne light to the beam block and detector.

Damage was determined to occur if, after irradiation with 3000 femtosecond laser pulses on a single spot in the sample, we see an increase in the amount of He:Ne light reaching the detector. The threshold was minimized by translating the sample in and out of the beam to find the best focus, then several measurements of the threshold were made and the average value was taken. The sample was always translated laterally after irradiation with the femtosecond beam, even if no damage was observed.

3.4 Ionization thresholds for femtosecond laser pulses

Using the dark-field scattering technique described above we measured the energy required to produce material damage in four dielectric materials with differing band gaps using femtosecond pulses with two different laser wavelengths and focused with three different numerical aperture microscope objectives. Figure 3.4 shows the numerical aperture dependence of the energy threshold for permanent damage for 400-nm (Figure 3.4a) and 800-nm (Figure 3.4b) pulses. The lines represent fits to Eqn. (3.2) using critical

powers from the literature[31] or measured using the technique described in Section 3.3.3. In the case of Corning 0211 where no literature value for the critical power was available and where direct measurement is difficult due to the very thin samples that are available, the critical power at 800 nm was left as a free parameter and we find that $P_{cr} = 1.5$ MW. This value is in good agreement with the 1.6 MW value for BK7 at 800 nm, a glass with composition and band gap similar to Corning 0211. For Corning 0211, there are additional 800-nm energy thresholds at 1.0 NA (7.0 nJ) and 1.4 NA (5.0 nJ) that are not shown in Figure 3.4, but were used in the fitting procedure. We used the known scaling of the critical power with laser wavelength (Eqn. (2.13)) to obtain a value for Corning 0211 at 400 nm.
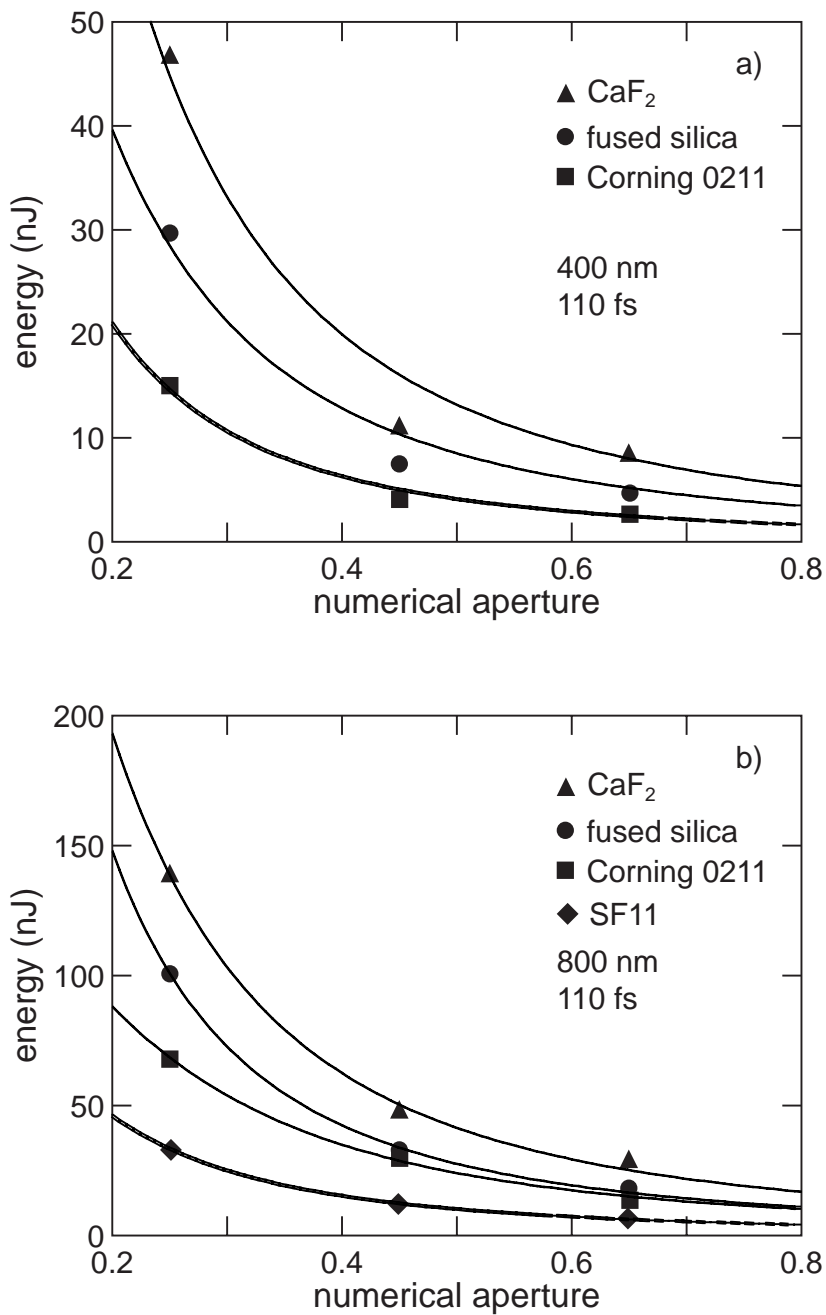
Figure 3.4 Energy threshold for permanent damage in SF11(◆), Corning
0211(■), fused silica(●), and CaF$_2$(▲) as a function of NA for a) 400-nm
and b) 800-nm wavelength, 110-fs laser pulses. Optical breakdown was
not observed in SF11 using 400-nm light. Data points at 1.0 NA (7.0 nJ)
and 1.4 NA (5.0 nJ) in Corning 0211 for 800-nm light are not shown. A fit
to Eqn. (3.2) is shown for each material.

We did not observe damage in SF11 using 400-nm laser pulses with laser energy up to several times the threshold for other materials. We did, however, observe strong blue fluorescence from the pumped region of the sample. For 400-nm pulses, the absorption in SF11 is a two-photon process. Apparently, the two photon absorption is efficient enough that there is significant absorption of the laser pulse before it reaches the laser focus. This absorption limits the peak laser intensity achieved at the focus, preventing optical breakdown from occurring. Perhaps the electrons produced in front of the laser focus by two-photon absorption also act as a negative lens and defocus the laser pulse, further limiting the peak laser intensity.

From the fits to Eqn. (3.2), the threshold intensity for optical breakdown and damage is determined. Table 3.1 shows, for all samples we studied, the measured intensity thresholds and the critical powers for self-focusing and material band gaps used in the fits. Note that while the threshold intensity for 400-nm pulses is lower than for 800-nm pulses in Corning 0211 and fused silica, the threshold for 400-nm pulses is actually slightly higher than for 800-nm pulses in CaF_2.

| material | 400 nm | | 800 nm | | |
	threshold intensity (W/cm^2)	critical power (MW)	threshold intensity (W/cm^2)	critical power (MW)	band gap (eV)
SF11	N/A	N/A	1.6×10^{13}	0.5	3.3
Corning 0211	1.5×10^{13}	0.4	2.8×10^{13}	1.6	4.4
fused silica	2.9×10^{13}	1.1	3.2×10^{13}	4.3	7.5
CaF_2	4.8×10^{13}	1.9	4.3×10^{13}	7.4	10.2

Table 3.1 Intensity threshold for optical breakdown and damage in several transparent dielectrics for 400-nm and 800-nm, 110-fs laser pulses. The band gap of the material and the critical power used in the fit to Eqn. (3.2) are also listed.

The threshold for bulk damage with 800-nm pulses in fused silica is in good agreement with the values in the literature for surface damage using 110-fs laser pulses.[9, 13] Stuart, *et al.* observed a roughly factor-of-two decrease in the surface damage threshold in fused silica for 526-nm pulses compared to 1053-nm pulses for pulse durations of 300 fs and longer.[10] In contrast, we observe only a slight difference in the 400-nm and 800-nm bulk damage thresholds in fused silica. The only other material we looked at that has been extensively studied for femtosecond pulses is CaF_2, where we find the bulk damage threshold to be about a factor-of-two higher than the surface damage threshold found by other groups.[18]

3.5   Discussion

In many recent experiments, researchers measured the pulse duration dependence of the threshold fluence required to produce material damage, and, assuming that the electron density must reach the critical density to produce material damage, fit that dependence to a rate equation for the electron density,

$$\frac{dN}{dt} = \alpha I N + P(I) \tag{3.3}$$

where N is the electron density, α is the avalanche ionization coefficient, and $P(I)$ is the photoionization rate, typically taken to be $\sigma_k I^k$, where σ_k is the multiphoton absorption coefficient for k-photon absorption.[9, 10] The number of photons required is determined by the smallest k which satisfies the relation $k\hbar\omega \geq E_g$, where E_g is the band gap of the material and $\hbar\omega$ is the laser photon energy. The multiphoton absorption coefficient and

57

the avalanche ionization coefficient are fit to the data. This approach has the advantage that it is basically model-independent.

Here, because we do not have pulse duration dependence, we use Keldysh's theory for photoionization to interpret the bulk damage thresholds listed in Table 3.1. First, we calculate the Keldysh parameter (Eqn. (2.18)), and determine whether the photoionization is best represented by a multiphoton or tunneling ionization picture. Next, we calculate the electron density due to photonionization based on the rates predicted by Keldysh and compare this electron density to the critical density to determine the importance of avalanche ionization.

3.5.1   Multiphoton vs. tunneling ionization

Table 3.2 shows the Keldysh parameter and the electron density due to photoionization alone (avalanche ionization is not included) calculated based on the measured intensity thresholds for damage listed in Table 3.1. The full Keldysh expression for $P(I)$, Eqn. 37 in Ref. [8] was used to calculate the electron densities. For 400-nm light, the Keldysh parameter for all materials is well into the multiphoton ionization regime. For 800-nm light, however, the Keldysh parameter is in the intermediate region where the process is not truly a multiphoton ionization process and the approximation of the photonionization rate as $\sigma_k I^k$ in Eqn. (3.3) is not well justified. In fact, based on Figure 2.6 the multiphoton ionization rate is about an order of magnitude below the rate based on the full formula for 800-nm light in fused silica, and it may actually be better to characterize the photoionization for 800-nm light as a tunneling process. Lenzner, *et al* also emphasized

the importance of considering tunneling ionization as an important ionization mechanism for short pulse durations.[9]

material	400 nm		800 nm	
	Keldysh parameter	electron density (cm^{-3})	Keldysh parameter	electron density (cm^{-3})
SF11	N/A	N/A	1.2	3.0 X 10^{21}
Corning 0211	2.7	5.2 X 10^{21}	1.0	2.7 X 10^{21}
fused silica	2.5	3.7 X 10^{20}	1.2	4.1 X 10^{19}
CaF$_2$	2.3	4.8 X 10^{19}	1.2	2.5 X 10^{18}

Table 3.2 Keldysh parameter and electron density due to multiphoton and tunneling ionization calculated using the measured intensity thresholds for damage listed in Table 3.1 and Eqn. 37 in Ref. [8]. Avalanche ionization is not included in the calculation of the electron density. For comparison, the critical density is 6.9 X 10^{21} cm^{-3} (1.7 X 10^{21} cm^{-3}) for 400-nm (800-nm) light.

3.5.2   Contribution of avalanche ionization

The electron densities listed in Table 3.2 should be compared to the critical plasma density for the laser wavelengths. It is commenly assumed that a critical density plasma must be formed to produce material damage.[9, 10, 17] As discussed in Section 2.3.3, the plasma becomes strongly absorbing near the critical density, allowing a significant fraction of the laser pulse energy to be deposited into the material, leading to damage. For a laser wavelength of 400 nm (800 nm) the critical density is 6.9 X 10^{21} cm^{-3} (1.7 X 10^{21} cm^{-3}).

For the low band gap materials (SF11 and Corning 0211 at 800 nm and Corning 0211 at 400 nm) photoionization alone is sufficient to produce a critical density plasma, indicating that avalanche ionization plays a small role in the ionization process. This is in agreement with the results of Lenzner, *et al.* for femtosecond pulses in barium aluminum borosilicate glass which has a band gap of about 4 eV, in the same range as SF11 and

59

Corning 0211.[9] For fused silica and CaF_2 for both 400-nm and 800-nm wavelength, the electron densities in Table 3.2 fall well below the critical density, indicating that avalanche ionization plays a more important role.

We calculate the avalanche coefficients that are necessary to produce a critical density plasma in fused silica and CaF_2 for both 400-nm and 800-nm wavelength using the rate equation, Eqn. (3.3). We use the full Keldysh formula to determine the photoionization rate, $P(I)$, and use our measured threshold intensities. We find the avalanche coefficients to be: 1.6 cm^2/J (800 nm, fused silica), 2.0 cm^2/J (800 nm, CaF_2), 1.3 cm^2/J (400 nm, fused silica), and 1.4 cm^2/J (400 nm, CaF_2). The weak wavelength dependence of the avalanche ionization coefficient that we observe is in agreement with the results of Stuart, *et al.*[10] The avalanche coefficient we find for 800-nm light in fused silica is, however, smaller than that found by other researchers (values range from 4.0 cm^2/J to 10 cm^2/J), perhaps indicating that the electron densities calculated using the Keldysh rates are too high, as Lenzner, *et al.* suggest.[9] If we take the multiphoton ionization rate suggested by Lenzner, $\sigma_6 = 6.0 \times 10^8 \text{cm}^{-3} \text{ps}^{-1} (\text{cm}^2 / \text{TW})^6$, then using our measured threshold intensity, we find an avalanche ionization coefficient of 4.5 cm^2/J, in good agreement with literature values.

3.6   Conclusions

We presented a method for accurately determining the intensity threshold for producing damage in bulk transparent materials by laser irradiation. The laser pulse is tightly focused into the material so that the threshold intensity is reached with low peak power, and therefore with minimal self-focusing. Using this technique, we measured the laser

wavelength and material band gap dependence of the intensity threshold for bulk damage using 110-fs laser pulses. Our results indicate that avalanche ionization produces most of the free electons for large band gap materials, while photoionization produces a significant fraction of the electron density for small band gap materials. For 400-nm laser pulses, photoionization is a multiphoton absorption process, while for 800-nm pulses photoinoization is more in the tunneling regime. More experimental and theoretical work is necessary to resolve the current debates about photoionization rates and the validity of Keldysh's theory as well as the scaling of the avalanche ionization rate with laser intensity.

As a final note, we discuss some implications of this work for micromachining transparent materials. The energy thresholds for 0.65-NA focusing shown in Figure 3.4 are under 50 nJ for all materials studied. This energy is achievable with cavity-dumped[34, 35] and long-cavity[36, 37] femtosecond laser oscillators, opening the door to unamplified micromachining.[5] The threshold in Corning 0211, at 5 nJ for 1.4-NA focusing, is within the range of commercially available laser systems. Using unamplified lasers for micromachining not only greatly reduces the cost and complexity of the laser system, but also, because of the high repetition rate, allows for higher machining speeds than are possible with amplified systems. The morphology of the damage produced with femtosecond pulse trains from a laser oscillator is discussed in Section 4.7, and oscillator-only micromachining applications are discussed in Section 7.3.

References

1. N. Bloembergen, Journal of Nonlinear Optical Physics and Materials **6**, 377 (1997).

2. M. D. Perry and G. Mourou, *Science* **264**, 917 (1994).

3. X. Liu, D. Du, and G. Mourou, *IEEE J. Quantum Electron.* **33**, 1706 (1997).

4. E. N. Glezer, M. Milosavljevic, L. Huang, R. J. Finlay, T.-H. Her, J. P. Callan, and E. Mazur, *Opt. Lett.* **21**, 2023 (1996).

5. C. B. Schaffer, A. Brodeur, J. F. Garcia, and E. Mazur, *Opt. Lett.* **26**, 93 (2001).

6. K. M Davis, K. Miura, N. Sugimoto, and K. Hirao, *Opt. Lett.* **21**, 1729 (1996).

7. D. Homoelle, S. Wielandy, A. L. Gaeta, N. F. Borrelli, and C. Smith, *Opt. Lett.* **24**, 1311 (1999).

8. L. V. Keldysh, *Zh. Eksp. Teor. Fiz.* **47**, 1945 (1964) [*Sov. Phys. JETP* **20**, 1307 (1965)].

9. M. Lenzner, J. Krüger, S. Sartania, Z. Cheng, Ch. Spielmann, G. Mourou, W. Kautek, and F. Krausz, *Phys. Rev. Lett.* **80**, 4076 (1998).

10. B. C. Stuart, M. D. Feit, S. Herman, A. M. Rubenchik, B. W. Shore, and M. D. Perry, *Phys. Rev. B* **53**, 1749 (1996).

11. B. C. Stuart, M. D. Feit, S. Herman, A. M. Rubenchik, B. W. Shore, and M. D. Perry, *J. Opt. Soc. Am. B* **13**, 459 (1996).

12. N. Bloembergen, *IEEE J. Quantum Electron.* **QE-10**, 375 (1974).

13. A.-C. Tien, S. Backus, H. Kapteyn, M. Murnane, and G. Mourou, *Phys. Rev. Lett.* **82**, 3883 (1999).

14. K. K. Thornber, *J. Appl. Phys.* **52**, 279 (1981).

15. R. M. Wood, *Laser Damage in Optical Materials* (Hilger, Boston 1986).

16. M. J. Soileau, W. E. Williams, E. W. Van Stryland, T. F. Boggess, and A. L. Smirl, *Natl. Bur. Stand. (U.S.) Spec. Publ.* **669**, 387 (1984).

17. D. Du, X. Liu, G. Korn, J. Squier, and G. Mourou, *Appl. Phys. Lett.* **64**, 3071 (1994).

18. H. Varel, D. Ashkenasi, A. Rosenfeld, R. Herrmann, F. Noack, and E. E. B. Campbell, *Appl. Phys. A* **62**, 293 (1996).

19. W. Kautek, J. Krüger, M. Lenzner, S. Sartania, Ch. Spielmann, and F. Krausz, *Appl. Phys. Lett.* **69**, 3146 (1996).

20. D. von der Linde and H. Schüler, *J. Opt. Soc. Am B* **13**, 216 (1996).

21. M. Li, S. Menon, J. P. Nibarger, and G. N. Gibson, *Phys. Rev. Lett.* **82**, 2394 (1999).

22. A. Rosenfeld, M. Lorenz, R. Stoian, and D. Ashkenasi, *Appl. Phys. A* **69[Suppl]**, S373 (1999).

23. M. Lenzner, J. Krüger, W. Kautek, and F. Krausz, *Appl. Phys. A* **69**, 465 (1999).

24. W. L. Smith, J. H. Bechtel, and N. Bloembergen, *Phys. Rev. B* **15**, 4039 (1977).

25. M. Sparks, D. L. Mills, R. Warren, T. Holstein, A. A. Maradudin, L. J. Sham, E. Loh, Jr., and D. F. King, *Phys. Rev. B* **24**, 3519 (1981).

26. M. J. Soileau, W. E. Williams, N. Mansour, and E. W. van Stryland, *Opt. Eng.* **28**, 1133 (1989).

27. S. C. Jones, P. Braunlich, R. T. Casper, X.-A. Shen, and P. Kelley, *Opt. Eng.* **28**, 1039 (1989).

28. J. H. Marburger, *Prog. Quantum Electron.* **4**, 35 (1975).

29. A. L. Gaeta, *Phys. Rev. Lett.* **84**, 3582 (2000), and references therein.

30. E. Yablonovitch, *Appl. Phys. Lett.* **19**, 495 (1971).

31. A. Brodeur and S. L. Chin, *Phys. Rev. Lett.* **80**, 4406 (1998).

32. A. Brodeur and S. L. Chin, *J. Opt. Soc. Am. B* **16**, 637 (1999).

33. A. E. Siegman, *Lasers* (University Science Books, Sausalito, CA, 1986), p. 630.

34. A. Baltuska, Z. Wei, M. S. Pshenichnikov, D. A. Wilson, and R. Szipocs, *Appl. Phys. B* **65**, 175 (1997).

35. M. S. Pshenichnikov, W. P. de Boeij, and D. A. Wiersma, *Opt. Lett.* **19**, 572 (1994).

36. S. H. Cho, U. Morgner, F. X. Kartner, E. P. Ippen, J. G. Fujimoto, J. E. Cunningham, and W. H. Knox, *OSA Technical Digest: Conference on Lasers and Electro Optics* **99**, 470 (1999).

37. A. R. Libertun, R. Shelton, H. C. Kapteyn, and M. M. Murnane, *OSA Technical Digest: Conference on Lasers and Electro Optics* **99**, 469 (1999).

Chapter 4

Bulk structural change morphology

4.1   Introduction

In recent years, femtosecond lasers have been used for a multitude of micromachining tasks.[1] Several groups have shown that femtosecond laser pulses cleanly ablate virtually any material with a precision that consistently meets or exceeds that of other laser-based techniques, making the femtosecond laser an extremely versatile surface micromachining tool.[2 – 7] For large band gap materials, where laser machining relies on nonlinear absorption of high intensity pulses for energy deposition, femtosecond lasers offer even greater benefit. Because the absorption in a transparent material is nonlinear, it can be confined to a very small volume by tight focusing, and the absorbing volume can be located in the bulk of the material, allowing three-dimensional micromachining.[8, 9] The extent of the structural change produced by femtosecond laser pulses can be as small as or even smaller than the focal volume. Recent demonstrations of three-dimensional micromaching of glass using femtosecond lasers include three-dimensional binary data storage, [8, 10] and the direct writing of optical waveguides[9, 11, 12] and waveguide

splitters.[13] The growing interest in femtosecond laser micromachining of bulk transparent materials makes it more important than ever to uncover the mechanisms responsible for producing permanent structural changes.

4.1.1   Overview of energy deposition and material changes

To micromachine a transparent material in three-dimensions, a femtosecond laser pulse is tightly focused into the material. As discussed in Section 2.3 and Chapter 3, the laser intensity in the focal volume can become high enough to ionize electrons by multiphoton ionization, tunneling ionization, and avalanche ionization.[14 - 17] This nonlinear ionization leads to optical breakdown and plasma formation, but only in the focal volume where the laser intensity is high. For a transparent material, the laser focus can be located in the bulk of the sample, and so the energy deposition occurs inside the material. Initially, the energy deposited by the laser pulse resides only in the electrons, with the ions still cold. On a ten picosecond time scale, the electrons collisionally heat the ions and the two systems reach thermal equilibrium at a temperature of about 10^5 K. On a ten nanosecond time scale, the electrons recombine with the ions, producing the spark characteristic of optical breakdown. After the plasma recombines, the remaining energy in the material is in the form of thermal energy. This thermal energy diffuses out of the focal volume on a microsecond time scale.

For laser pulse energies above a certain material-dependent energy threshold, permanent structural changes are produced in the material. Several different mechanisms can lead to these changes, each producing a different morphology — from small density variations, to color centers, to voids. For example, if the melting temperature of the material is exceeded in some small volume, the material can resolidifiy non-uniformly,

leading to density and refractive index variations. The laser pulse can induce color center formation in some materials, leading to refractive index changes in the focal volume.[12, 18] At higher laser energy, hot electrons and ions may explosively expand out of the focal volume into the surrounding material.[19] This explosive expansion leaves a void or a less dense central region surrounded by a denser halo. Densification of glass by femtosecond laser pulses in a manner analogous to ultraviolet induced densification has also been suggested.[13] Which of these mechanism causes structural change depends on laser, focusing, and material parameters.

For very tight focusing, the minimum size of a structurally altered region is under 1 μm.[8, 9] These microscopic material changes are the building blocks from which more complex, three-dimensional devices can be micromachined. By scanning the laser focus through the material, a three-dimensional object can be built up out of the changes made by each laser pulse. In addition, as described above, different laser and material parameters can lead to different structural change morphologies, allowing another degree of freedom in device fabrication.

In this chapter, we present a systematic study of the morphology of structural changes induced in bulk glass by tightly-focused femtosecond laser pulses. Using high-resolution optical microscopy we investigate the dependence of the morphology of the structural change on laser energy and number of laser shots as well as on focusing angle. We use electron microscopy to obtain a more detailed look at the morphology. Our observations show a transition from a structural change mechanism dominated by localized melting or densification to one dominated by an explosive expansion. We also present a new method for bulk micromachining with high repetition-rate femtosecond

lasers which causes material changes by a cumulative heating of the material around the focus by multiple laser pulses.

4.2   The role of pulse duration

Previous work has shown that for pulses longer than a few hundred femtoseconds, the structural changes produced by the laser pulse become larger than the focal volume, degrading the machining precision. [8, 15, 20, 21] In addition, such pulses often cause cracks that radiate from the focal region. The greater extent of the structural change and the cracks are due to the greater energy that is required to reach the intensity threshold for nonlinear ionization with these longer pulses.

In transparent materials, the threshold for producing permanent structural change coincides with the threshold for optical breakdown and plasma formation.[15] If the laser intensity exceeds the threshold intensity, a critical density plasma is formed as the temporal peak of the pulse passes through the laser focus. As discussed in Section 2.3.3, this plasma strongly absorbs energy from the second half of the laser pulse, depositing enough energy to produce permanent structural change. This plasma formation and absorption explains the larger damage observed for longer laser pulses. For long laser pulses the energy required to reach the threshold intensity for plasma formation is higher, and consequently more energy is deposited in the material by the strong absorption of the second half of the pulse, leading to more extensive material changes. For femtosecond laser pulses, breakdown occurs with less energetic laser pulses, leading to less energy deposition and smaller structural changes. More discussion of the differences between long and short pulse laser-induced damage can be found in Section 2.4.

For high precision micromachining, damage outside the focal volume must be minimized. Experiments in a variety of transparent materials suggest that pulse durations of a few hundred femtoseconds or shorter are necessary for the structural change produced near the threshold to be confined to the focal volume. All the work described in this paper was carried out with laser pulses with a duration of 110 fs or less.

4.3   Experimental techniques

To achieve micrometer machining precision, the laser pulses must not only be of femtosecond duration and near threshold energy, they must also be focused with high numerical aperture (NA) microscope objectives. Furthermore, care must be taken to ensure that the laser is focused to a diffraction-limited spot size. For this tight focusing, the energy threshold for producing material changes is low enough that an unamplified laser system can be used for micromachining. In this Section, we discuss the proper use of microscope objectives, and describe a modified femtosecond laser oscillator that is used for unamplified micromachining.

4.3.1   Focusing with microscope objectives

A diagram of the focusing setup used in the experiments discussed in this paper is shown in Figure 4.1. A 110-fs, 800-nm laser pulse from a regeneratively amplified Ti:Sapphire laser is focused inside the bulk of a transparent material by a microscope objective with a numerical aperture in the range of 0.25 to 1.4. The sample is moved by a computer controlled stage and single or multiple laser pulses are fired into the sample to produce arrays of structures. We then examine these arrays using differential interference contrast

(DIC) optical microscopy, scanning electron microscopy (SEM), and atomic force microscopy (AFM).
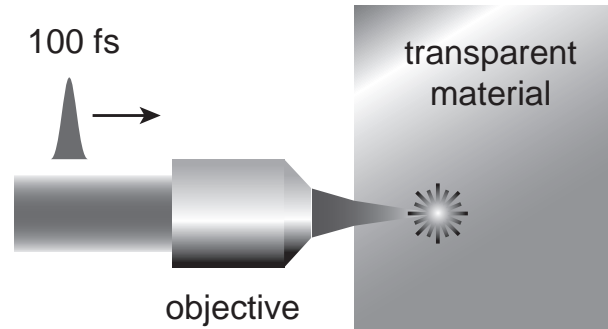
Figure 4.1 Diagram of the focusing setup used to produce structures in bulk glass using femtosecond laser pulses.

To achieve the highest laser intensity for a given pulse energy, the laser pulse must be delivered to the sample without temporal distortion and must be well focused inside the sample. It is difficult to directly measure the laser pulse duration at the focus of the high-NA objectives, so, instead, we minimize the observed threshold for producing structural change by adjusting the grating-based pulse compressor on the laser system. We generally find that for all but the 1.4-NA oil-immersion objective, there is very little change in threshold due to compressor adjustment for transform-limited 110-fs pulses. This lack of change reflects the moderate dispersion of the objectives and the moderate bandwidth of our regeneratively amplified laser system.

To ensure diffraction-limited focusing, the back aperture of the microscope objective is illuminated as uniformly as possible and is completely filled. The sample, Corning 0211, is the glass used to make cover slips, and the laser is focused 170 μm

beneath the surface, where the microscope objective is designed to have minimal spherical aberration. For microscope objectives with NA greater than about 0.5, the threshold for structural change increases dramatically when the laser is not focused at the optimal depth in the material. This increase is caused by degradation of the laser focus due to spherical aberration. For machining applications, this problem can be overcome by using an objective with a collar that compensates for varying amounts of spherical aberration.[22] For the experiments described here, the laser is always focused at the depth where the threshold for producing structural change is the lowest.

For objectives with NA less than about 0.45, the power required to reach the threshold intensity for structural change approaches the critical power for self-focusing for the material. As a result, self-focusing and other nonlinear propagation effects must be taken into account.[23 - 25] Self-focusing can also play a role when above-threshold energy is used to produce structural changes.

4.3.2   Long-cavity oscillator

Using the light scattering technique discussed in Section 3.3.4, we measured the threshold for permanent structural change in Corning 0211 to be only 5 nJ for 110-fs pulses focused by a 1.4-NA oil-immersion microscope objective.[9] This low threshold opens the door to using unamplified laser systems for micromachining. In Section 5.2 we will discuss how micromachining with an oscillator can differ from micromachining with amplified lasers, and in Section 7.3 we show some of the applications of this oscillator-only micromachining. Here describe the long-cavity laser oscillator used for these experiments.

Because of losses in the prism compressor, beam delivery optics, and the microscope objective, it is necessary to start with about 15 nJ of laser energy to deliver 5 nJ to the sample. This energy is slightly higher than the output of standard Ti:Sapphire laser oscillators. To achieve this higher output energy, we constructed a long-cavity Ti:Sapphire laser oscillator.[26, 27] A one-to-one imaging telescope, based on a 2-m radius of curvature mirror, is inserted into the output coupler end of a Ti:Sapphire laser. The telescope images the old position of the output coupler to its new position, keeping the spatial modes of the laser the same, while increasing the length of the cavity. The longer cavity allows more gain to build up in the laser crystal before the pulse depletes it. The result is higher energy pulses at a lower repetition rate. Our laser operates at 25 MHz, and routinely produces 20-nJ, 30-fs pulses.

The 40-nm wide bandwidth of the 25-MHz oscillator makes dispersion compensation essential, especially when using a 1.4-NA objective. We use a prism compressor to minimize the energy threshold for producing a structural change in the sample. Because optical breakdown is an intensity-dependent process, this minimizes the pulse width. We do not measure the pulse duration at the laser focus. Other groups have shown by direct measurement that, using only a simple prism pair for dispersion compensation, pulses as short as 15 fs can be achieved at the focus of high-NA objectives.[28]

4.4   Optical microscopy of structural change morphology

In order to reliably machine a structure, we must know the nature and extent of the structural change produced by a single laser pulse. To this end, we studied the

morphology of the structural change produced for various laser and focusing parameters in bulk borosilicate glass (Corning 0211) by tightly-focused femtosecond laser pulses.

4.4.1 Role of laser pulse energy and focusing angle

We first look at differences in the structural changes produced by different laser pulse energies focused by different microscope objectives. Figure 4.2 shows a DIC micrograph of an array of structures produced in Corning 0211 using single, 40-nJ, 110-fs laser pulses focused by a 0.65-NA microscope objective. The diameter of the structures in the image is about 0.5 μm, the resolution limit of the optical microscope used to take the image. The structures shown in Figure 4.2 are difficult to visualize without a contrast enhancing microscopy technique such as DIC, because the refractive index change is small. The inset in Figure 4.2 shows a side view taken in reflection of a structure produced using 110-fs, 40-nJ pulses focused by a 0.65-NA objective. The inset is on the same scale as the rest of the image. The elongation of the structure reflects the oblong focal volume of the 0.65-NA objective. The structures shown in Figure 4.2 are produced with an energy that is about twice the observed threshold for permanent structural change for this objective.
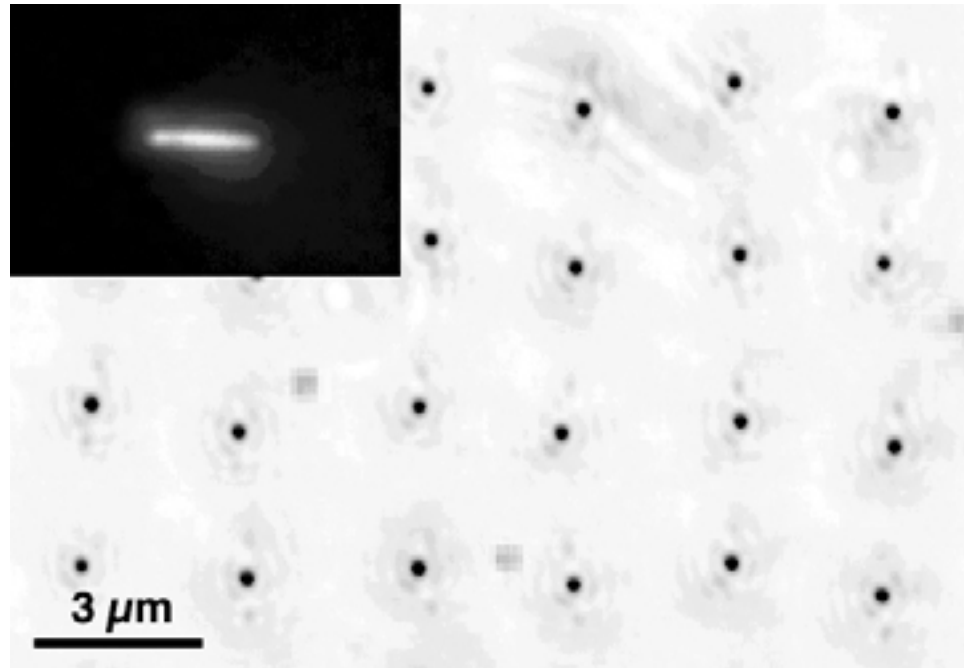
Figure 4.2 DIC optical micrograph of an array of structures produced with single, 40-nJ, 110-fs laser pulses focused by a 0.65-NA objective. The laser pulse is incident perpendicular to the plane of the image. The inset shows, at the same scale, a side-view optical micrograph of a structure taken in reflection. The laser pulse is incident from the left of the inset.

Figure 4.3 shows side-view DIC optical micrographs of structures produced in Corning 0211 using 110-fs laser pulses with different laser energies and focused by different microscope objectives. Figure 4.3a shows structures produced by 50-nJ pulses focused by a 0.45-NA microscope objective. The cylindrical structures are similar to the structures shown in Figure 4.2, except that the cylinders are about 4 μm long, reflecting the longer confocal parameter of the 0.45-NA objective compared to that of the 0.65-NA objective. Figure 4.3b shows structures produced by 15-nJ pulses focused by a 1.4-NA oil-immersion microscope objective. The structures are only slightly elongated along the beam propagation direction and have a length of approximately 1.5 μm. The shape and extent of the structural change is again determined by the focal volume.
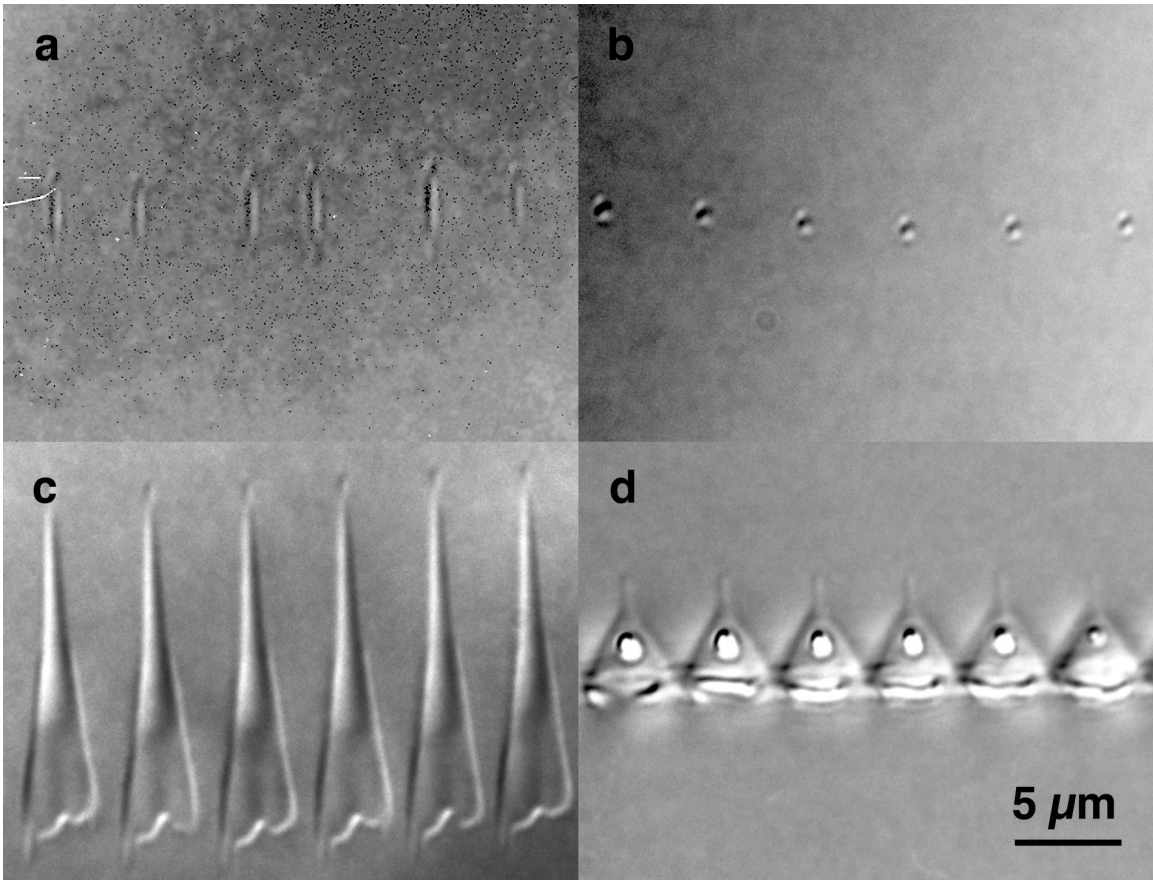
Figure 4.3 Side-view DIC optical images of structures produced in bulk glass using single, 110-fs laser pulses with various laser energies and focusing conditions: a) 50 nJ, 0.45 NA; b) 15 nJ, 1.4 NA; c) 500 nJ, 0.45 NA; d) 500 nJ, 1.4 NA. The laser pulse is incident from the bottom of the figure.

For laser energies that exceed the threshold energy by about a factor of ten or more, the structures show a more complicated morphology than the cylindrical structures shown in Figure 4.2, Figure 4.3a, and Figure 4.3b. Figure 4.3c shows structures produced with 500-nJ pulses focused by a 0.45-NA objective. The structure has a conical shape with the base of the cone oriented toward the incident direction of the laser. The extent of the structural modification is much larger than the focal volume of the objective. The structures are also formed closer to the laser than the focal plane of the objective. This upstream shift in position is due to self-focusing of the laser pulses in the material. Using

third-harmonic microscopy, Squier, *et al.* have taken three-dimensional images of structures similar to those shown in Figure 4.3c.[29]

Figure 4.3d shows structures produced with 500-nJ pulses focused by a 1.4-NA oil-immersion microscope objective. The conical structures have a steeper cone angle than the structures shown in Figure 4.3c, and the base of the cone shows indications of cracking. Also visible in Figure 4.3d is a high contrast, spherically shaped region in the center of each cone. These spherical regions are easily visible under standard white-light transmission microscopy, indicating that the refractive index change is larger in these regions than for the rest of the structure. Electron microscopy reveals that the spherical regions are voids inside the glass.

4.4.2   Multiple-shot morphology at low repetition rate

At repetition rates below about 1 MHz, the energy deposited into the focal volume by one laser pulse is carried away by thermal diffusion before the next pulse arrives. As a result, there is not heating of the material by successive pulses, and multiple pulses amplify the structural change produced by a single pulse leading to higher contrast structures. Figure 4.4 shows a DIC optical micrograph of an array of structures in Corning 0211 produced using 110-fs laser pulses from a 1-kHz laser focused by a 1.4-NA oil-immersion objective. Each structure is made with a different combination of laser energy and number of incident shots. The energy ranges from 6.6 to 66 nJ while the number of shots incident on each spot ranges from 2 to 5000. The diameter of the structures increases with increasing laser energy, while the optical contrast increases with increasing number of incident laser pulses. The desired optical contrast and size scale of the structure can be set, almost independently, by choosing an appropriate laser energy and number of laser

shots on a single spot. For the range of energies shown in Figure 4.4, the structures retain

the slightly elongated morphology shown in Figure 4.3b. It is only at higher energies that

the conical structures shown in Figure 4.3d appear.
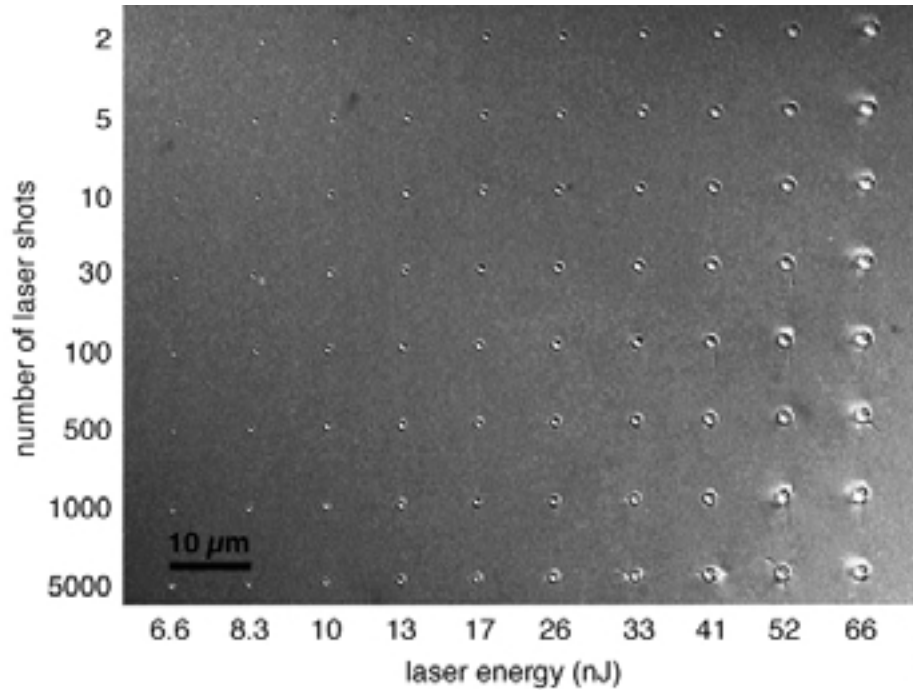
Figure 4.4 DIC optical micrograph of structures produced with various energy and various number of 110-fs laser pulses focused by a 1.4-NA microscope objective. The laser pulses are incident perpendicular to the plane of the image.

For this 1.4-NA focusing, no observable changes are produced by irradiating one

spot in the sample with many pulses that have too little energy to induce a structural

change with one laser pulse. In contrast, we do observe a decrease in the threshold for

optically observable structural changes for increasing number of incident laser pulses

when focusing with a 0.25-NA objective. Other researchers have observed a decrease in

the surface ablation threshold of transparent materials with multiple-pulse irradiation.[33,

34]

4.5 Scanning electron microscopy of structural change morphology

Although the optical micrographs in Section 4.4 show the rough features of the structural change morphology, it is difficult to determine details of the morphology from these optical images because the structures are at the resolution limit of an optical microscope. Because these details provide clues to the mechanisms responsible for producing the structural changes, we turn to scanning electron microscopy.

4.5.1 Sample preparation

Because SEM is a surface imaging tool, it is necessary to expose the bulk structural modifications before imaging. The samples can be prepared by polishing down to the level of the structures.[8] This method allows the diameter of structures that are too small to be resolved optically to be accurately determined. Polishing, however, smoothes out many small-scale features which may provide important information about the mechanism for structural change.

For this study, we prepared SEM samples using the steps outlined in Figure 4.5. A thin sample is scribed on one side using a diamond glass cutter. The femtosecond laser beam is focused into the sample through the unscribed surface, and the sample is translated at about 5 mm/s during the exposure to a 1-kHz pulse train, producing a row of structures spaced by about 5 μm. Multiple 5-μm spaced rows of structures are written 170 μm beneath the surface of the sample in the region just above the diamond scribe line. After irradiation, the samples are fractured along the scribe line. The fracture plane

goes through some structures, bringing them to the surface so they can be imaged in the SEM. Before imaging, the sample is coated with 5 to 10 nm of graphite to make it conductive. In addition to preserving small-scale features that are smoothed out by polishing, this technique provides side-view images, which are hard to obtain by polishing because of the small diameter of the structures.

1. irradiate scribed sample

2. bulk damage above scribe

3. fracture sample along scribe

4. coat surface with graphite

5. image

AFM   SEM
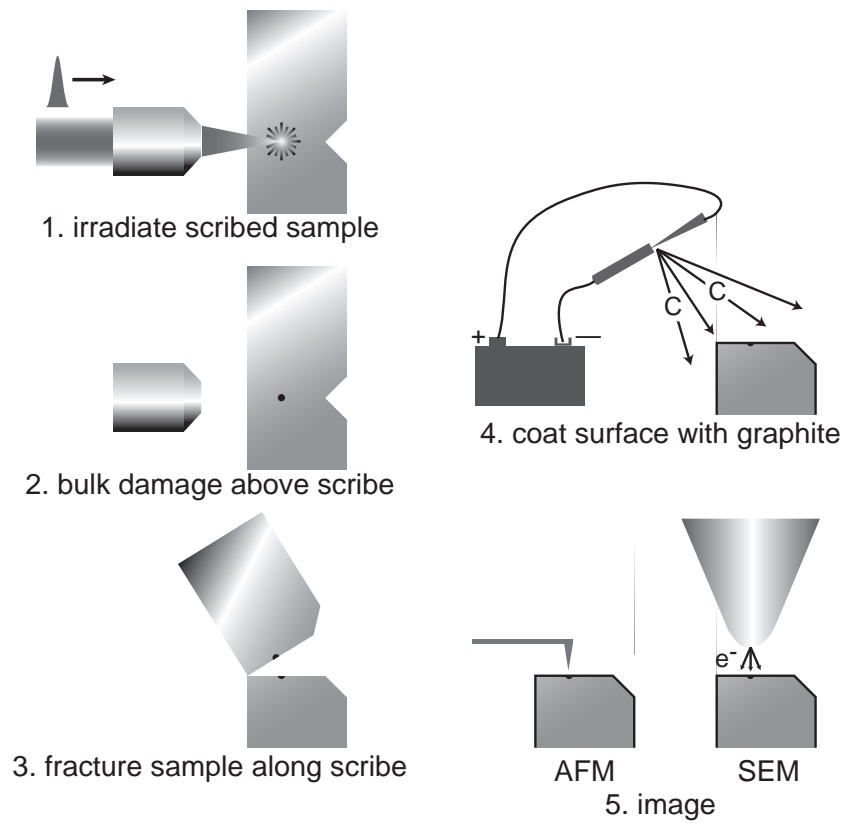
Figure 4.5 Schematic diagram showing the procedure used to prepare samples for imaging in the SEM or AFM.

4.5.2   Role of laser pulse energy and focusing angle

Figure 4.6 shows SEM images of structures produced by 110-fs laser pulses focused by a 0.45-NA objective. The laser pulse energies are 140 nJ in Figure 4.6a, 250 nJ in Figure

4.6b, and 500 nJ in Figure 4.6c. The SEM image of the structures looks different depending on what part of the structure is bisected by the fracture plane. For the structures shown in Figure 4.6, the fracture plane went through the center of each structure. There is a transition in morphology between the structures produced with 140 nJ and those produced with 500 nJ. The structures produced with 500 nJ show clear evidence of a void at the center of the structure, while the structures produced with 140 nJ show only very small surface relief. The structures made with 250 nJ represent a transition between these two morphologies. We have previously observed voids similar to those in Figure 4.6c in SEM studies of samples that were polished to bring the structures to the surface.[8]

We preformed atomic force microscopy on structures similar to those shown in Figure 4.6. We find that the lobes on either side of the void in Figure 4.6c rise a few hundred nanometers from the surface. The outside edges are sharp suggesting that a fracture occurred. The structures shown in Figure 4.6a have a very smooth surface relief of about 100 nm.
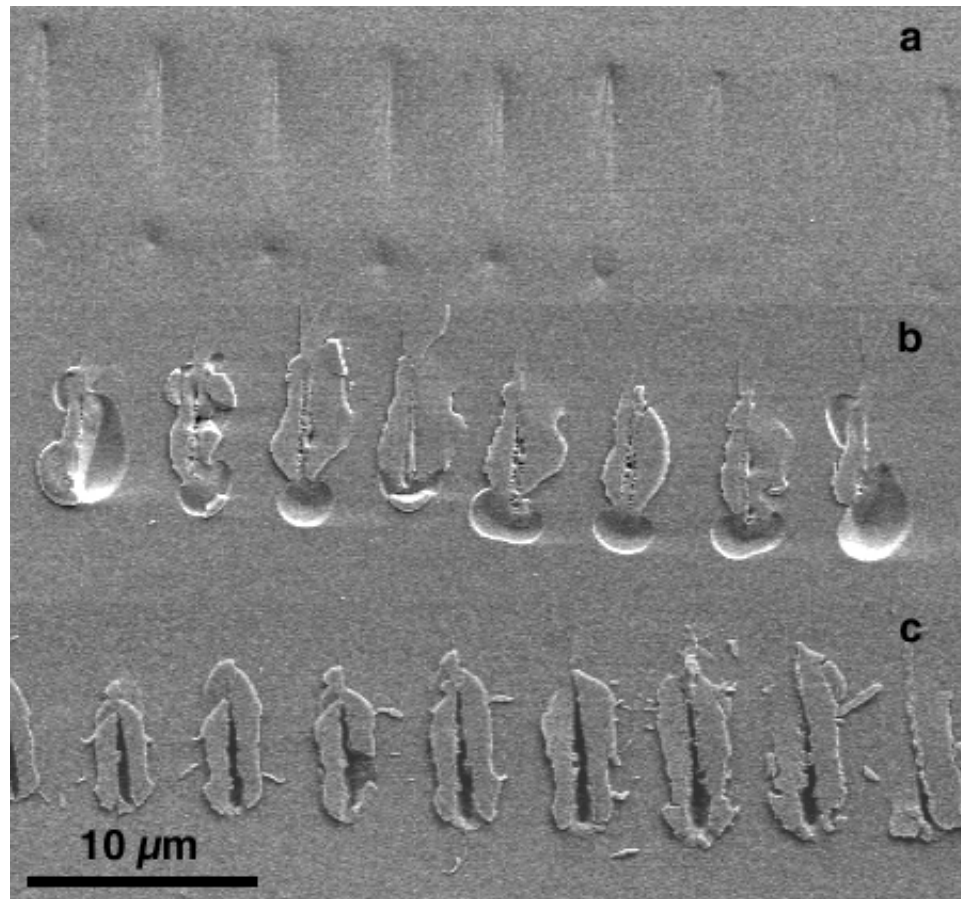
Figure 4.6 Side-view SEM images of structures produced in bulk glass using single, 110-fs laser pulses focused by a 0.45-NA microscope objective. The laser energies are: a) 140 nJ, b) 250 nJ, and c) 500 nJ. The laser pulse is incident from the bottom of the figure.

Figure 4.7shows a similar series of SEM images of structures produced by 110-fs pulses focused by a 1.4-NA oil-immersion objective. The laser energies are 36 nJ in Figure 4.7a, 140 nJ in Figure 4.7b, and 500 nJ in Figure 4.7c. Note the difference in scale relative to Figure 4.6. There is again a transition in morphology, from small surface relief in Figure 4.7, to a void in Figure 4.7b, to extensive cracking of the material in Figure 4.7c. Voids like those in Figure 4.7b produce the high contrast spherical structures in Figure 4.3d.
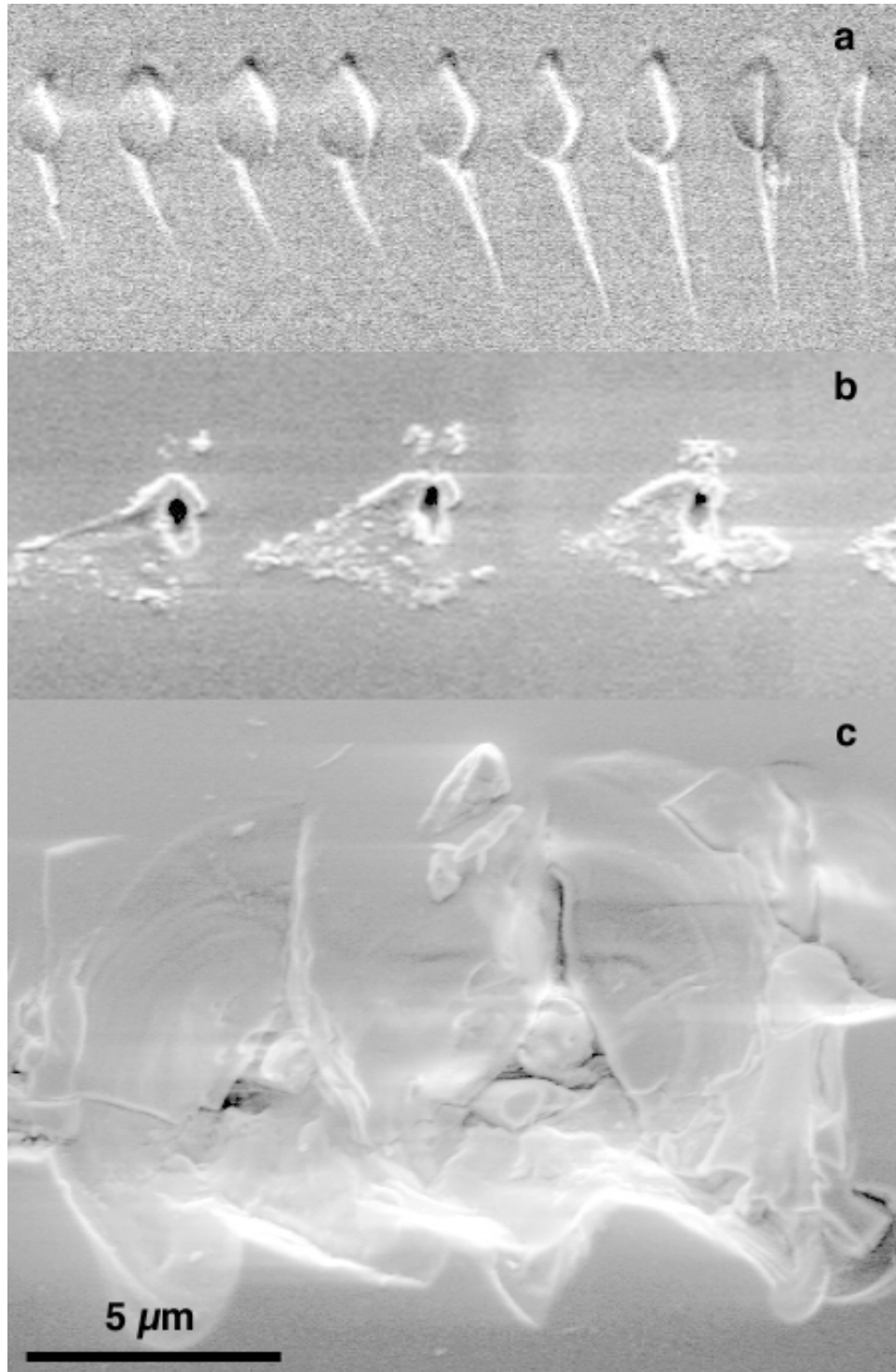
Figure 4.7 Side-view SEM images of structures produced in bulk glass using single, 110-fs laser pulses focused by a 1.4-NA oil-immersion microscope objective. The laser energies are: a) 36 nJ, b) 140 nJ, and c) 500 nJ. The laser pulse is incident from the bottom of the figure.

4.6 Connecting morphology to mechanism

We now discuss how various features of the structural change morphology presented in Sections 4.4 and 4.5 can be explained using the structural change mechanisms introduced in Section 4.1.1.

4.6.1 Cone-shaped structures

The production of the cone-shaped structures in Figure 4.3c and Figure 4.3d can be explained as follows. Because the pulse energy is significantly above the threshold for permanent change, a critical density plasma is formed at the focus by the leading edge of the pulse. This leading edge produces the structural change at the tip of the cone. Because the remainder of the pulse contains more energy than is necessary to produce a critical density plasma at the focus, it produces a plasma upstream from the laser focus, where the laser spot size is larger. Successive time slices of the pulse produce successively larger diameter structural changes that are located farther upstream from the focus, building up the cones seen in Figure 4.3c and Figure 4.3d. At the peak of the pulse, structural change is produced the farthest from the laser focus, forming the base of the cone. The second half of the laser pulse is strongly absorbed by the plasma formed by the peak of the pulse, leading to the extensive structural changes at the base of the cone seen in Figure 4.3d and in Figure 4.7c. This mechanism for producing structural change leads to a structure that extends over a region much larger than the focal volume and contains a wide range of material modification, from small density and refractive index changes near the tip of the cone, to voids inside the cone, to cracking at the base of the cone. From a micromachining perspective, it is clear that the highest precision is achieved when the

83

laser energy is close to the threshold for structural change, and the extent of the structural change is determined by the focal volume of the objective as in Figure 4.2, Figure 4.3a, and Figure 4.3b.

4.6.2   Voids

The voids evident in the SEM images in Figure 4.6c and Figure 4.7b suggest an explosive mechanism. After laser excitation, hot electrons and ions explosively expand out of the focal region into the surrounding material, leaving a void or less dense central region surrounded by a denser halo.[19] The lobes on either side of the void in Figure 4.6c and the ring-shaped surface relief in Figure 4.7c are due to trapped stress in the material resulting from the expansion that was released when the sample was fractured. As is clear from Figure 4.3d, the void is not necessarily formed at the laser focus, but rather where high enough energy density is achieved to drive the expansion.

4.6.3   Small refractive index changes

Closer to threshold the changes are more subtle. The surface relief shown in Figure 4.6a and Figure 4.7a is caused by fracturing either just above or just below material with a different density. A density change also explains the small refractive index change of the structures shown in Figure 4.2, Figure 4.3a, and Figure 4.3b.

How, then, does femtosecond laser irradiation lead to density changes in the material? One possibility is that the material heated by the laser pulse melts and resolidifies non-uniformly. For laser energies close to the threshold, the electrons and ions are not hot enough to drive the explosive expansion described above. Instead, they recombine, leaving molten material which cools and then resolidifies. Because of strong

gradients in temperature, the resolidification is nonuniform, leading to density changes in the material. Another possibility is that the laser pulse drives a structural transition by directly (*i.e.* nonthermally) breaking bonds in the material.[13] Femtosecond laser pulses are known to induce such nonthermal structural changes in semiconductors.[30] Furthermore, silica glasses are known to undergo densification when exposed to ultraviolet light, presumably due to the ionization in the glass.[31]

The different structural change morphologies and mechanisms described above can be used to tailor the structure produced by a single laser pulse to a particular machining application. The small density and refractive index changes produced near threshold are suitable for direct writing of optical waveguides and other photonic devices, while the voids formed at higher energy are ideal for binary data storage because of their high optical contrast. These and other applications are discussed in detail in Chapter 7.

4.7 Multiple-shot, high repetition-rate structural change morphology

In the experiments discussed so far, structural changes are produced by single laser pulses or multiple pulses which arrive at a low repetition rate. We now examine the morphology of the structures produced when multiple laser pulses, arriving at a high repetition rate, irradiate the same spot in a sample. For multiple-shot structural change, the repetition rate of the laser is an important factor. If the time between successive laser pulses is shorter than the roughly 1 μs it takes for energy deposited by one pulse to diffuse out of the focal volume, then a train of pulses irradiating one spot in the sample raises the temperature of

the material around the focal volume.[9, 32] In effect, the laser serves as a point source of heat that is localized inside the bulk of the material.

4.7.1   Optical microscopy of structural changes

Using the 25-MHz laser oscillator described in Section 4.3.2, we make arrays of structures and analyze them using DIC optical microscopy. Figure 4.8 shows an optical micrograph of structures made with 30-fs, 5-nJ pulse trains focused by a 1.4-NA objective. The number of incident pulses increases, by factors of 10, from 10^2 on the left to 10^5 on the right. The size of the structures shown in Figure 4.8 is much larger than the structures produced with single pulses, and the size of the structures increases with increasing number of laser pulses. Figure 4.9 shows the radius of the structures as a function of the number of incident laser pulses. Side-view microscopy reveals that the structures are spherical in shape. There is a series of rings evident in the structures on the right in Figure 4.8, suggestive of regions in the structure with different refractive index.
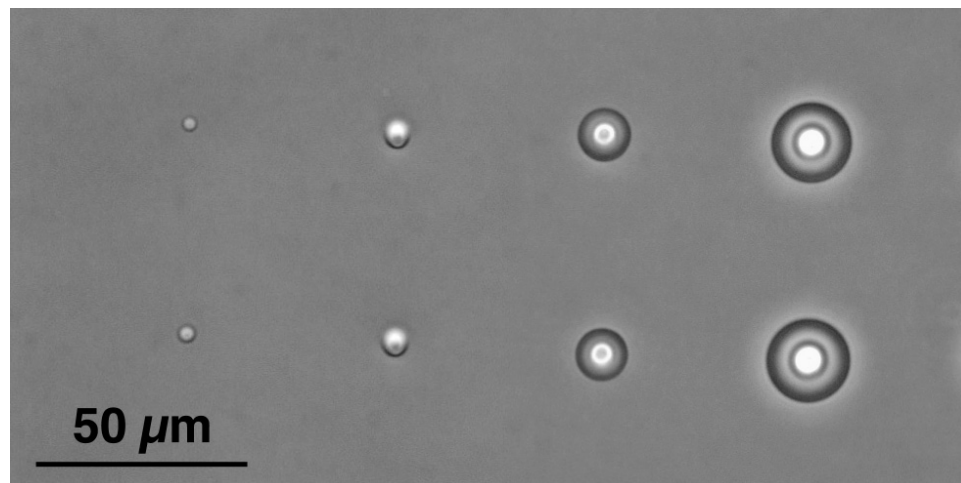
Figure 4.8 Optical microscope image of structures produced with multiple, 5-nJ, 30-fs laser pulses from a 25-MHz oscillator focused by a 1.4-NA objective. The number of pulses used increases, by factors of 10, from 10^2 on the left to 10^5 on the right. The laser pulses are incident perpendicular to the plane of the image.

The structures shown in Figure 4.8 are produced by a cumulative heating of the material around the laser focus by many successive laser pulses followed by non-uniform resolidification.[9] Because the time between successive pulses, at 40 ns, is much shorter than the characteristic time for thermal diffusion out of the focal volume, a train of pulses heats the material around the focal volume. Over many pulses a volume of material much larger than the focal volume is heated above the melting temperature for the glass. The larger the number of incident laser pulses, the larger the radius out to which the glass melts. After the pulse train is turned off, the material cools and, because of the temperature gradients, resolidifies non-uniformly, leading to the optical contrast shown in Figure 4.8. The size of the structures stops growing after about 10^7 pulses. At that point, the structure itself disturbs the laser focus, causing the intensity to drop below the threshold intensity and therefore preventing further energy deposition.

A non-thermal mechanism cannot account for the structures shown in Figure 4.8. First, the laser pulse train never directly irradiates most of the material where refractive index changes are observed. Only the sub-micrometer-sized focal volume at the center is directly irradiated, whereas the structures shown in Figure 4.8 extend up to 10 μm from the focal spot. Second, the size of the structure increases with the number of incident laser pulses, indicating that as more pulses deposit more energy, a larger region melts.

4.7.2   Modeling of cumulative thermal effect

We modeled this cumulative heating effect using a thermal diffusion equation. The maximum radius out to which the temperature exceeds the melting temperature for the glass was calculated for different numbers of incident laser pulses. Energy deposition by the laser is modeled as a series of heat sources that are delta functions in time and are spherical in shape with a volume equal to that of the focal volume for a 1.4-NA objective. The only free parameter is the fraction of each laser pulse that is absorbed by the material. The model best fit the data with 30% absorption, which is consistent with the transmission of the laser pulse slightly above the threshold for permanent structural change (see Section 3.3.2).[35] As shown in Figure 4.9, the model fits the data very well up to about 1000 laser pulses, after which the model underestimates the size of the affected region. This discrepancy is most likely due a change in the thermal properties of the glass as it heats and melts.
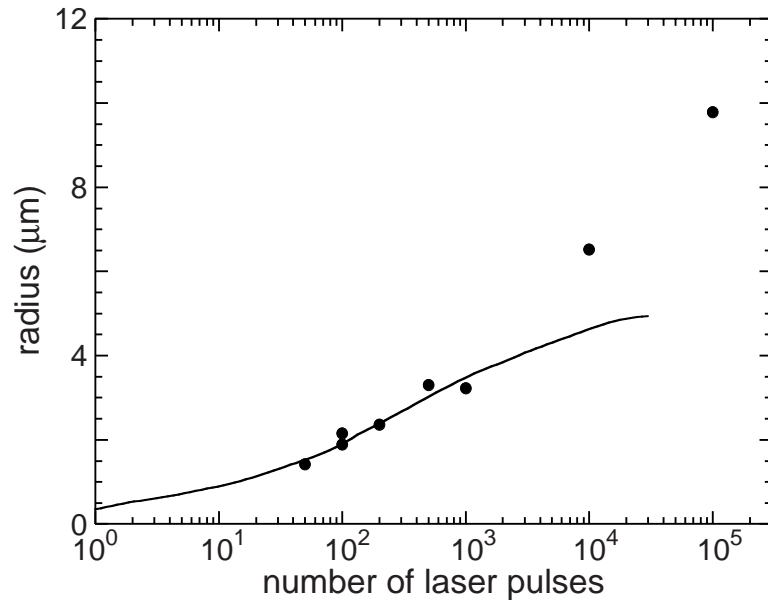
Figure 4.9 Radius of the structure produced with 30-fs, 5-nJ laser pulses incident at 25-MHz and focused by a 1.4-NA objective as a function of the number of incident laser pulses. The line represents the calculated maximum radius out to which the melting temperature of the glass is exceeded for a given number of incident laser pulses.

4.7.3 Implications for micromachining

The cummulative heating of material over many laser pulses described above offers a new possibility for the micromachining of transparent materials. The laser serves as a point source of heat that can be scanned through the bulk of a material. By adjusting the number of laser pulses incident on one spot, the amount of thermal energy deposited in a region can be controlled with nanojoule precision. To the best of our knowledge no other technique allows such precise deposition of thermal energy in micrometer-sized volumes in bulk material. Applications of this cummulative thermal effect for micromachining are discussed in Section 7.3.

4.8   Conclusions

Using optical and electron microscopy, we characterized the morphology of the structural change produced in bulk glass by tightly-focused femtosecond laser pulses with various laser energy and repetition-rate, and under various focusing conditions. We find that near the threshold for permanent structural change, the structures produced by single pulses consist of small density and refractive index changes with a shape that reflects the focal volume of the focusing objective. Under very tight focusing conditions, the threshold for structural change is only about 5 nJ, allowing micromachining with unamplified lasers. At higher laser energies, the shape of the structure is conical with the tip of the cone oriented along the laser propagation direction. This conical shape is produced by different time slices of the laser pulse producing breakdown at different positions upstream from the laser focus. Voids are also often formed in the material at high laser energies, suggesting an explosive mechanism. At high repetition rate, energy is deposited faster than it can diffuse out of the focal volume, resulting in a cumulative heating effect over many pulses. The laser serves as a point source of heat inside the material, melting a region of glass whose volume depends on the number of incident laser pulses. As an application of this cumulative heating effect, we discuss direct writing of single-mode optical waveguides inside bulk glass in Section 7.3.2.

We are currently further investigating the mechanisms responsible for producing permanent structural change, in particular at laser energies near the threshold, and developing applications for the cumulative thermal effect described in Section 5.2. Recently, we also found that femtosecond laser pulses can induce chemical, rather than structural, changes in bulk transparent materials. For example, one can locally carbonize

polystyrene by exposure to intense femtosecond laser pulses, opening the door to micrometer-scale nonlinear photochemistry. This technique shows great promise for the fabrication of micromechanical devices.

References

1. S. Nolte, G. Kamlage, F. Korte, T. Bauer, T. Wagner, A. Ostendorf, C. Fallnich, and H. Welling, *Advanced Engineering Materials* **2**, 23 (2000).

2. X. Liu, D. Du, and G. Mourou, *IEEE J. Quantum Electron.* **33**, 1706 (1997).

3. X. Zhu, A. Yu. Naumov, D. M. Villeneuve, and P. B. Corkum, *Appl. Phys. A* **69 [Suppl.]**, S367 (1999).

4. S. Nolte, C. Momma, H. Jacobs, A. Tünnermann, B. N. Chichkov, B. Wellegenhausen, and H. Welling, *J. Opt. Soc. Am B* **14**, 2716 (1997).

5. M. Lenzner, J. Krüger, W. Kautek, and F. Krausz, *Appl. Phys. A* **68**, 369 (1999).

6. W. Kautek, J. Krüger, M. Lenzner, S. Sartania, Ch. Speilmann, and F. Krausz, *Appl. Phys. Lett.* **69**, 3146 (1996).

7. M. D. Perry, B. C. Stuart, P. S. Banks, M. D. Feit, V. Yanovsky, and A. M. Rubenchik, *J. Appl. Phys.* **85**, 6803 (1999).

8. E. N. Glezer, M. Milosavljevic, L. Huang, R. J. Finlay, T.-H. Her, J. P. Callan, and E. Mazur, *Opt. Lett.* **21**, 2023 (1996).

9. C. B. Schaffer, A. Brodeur, J. F. Garcia, and E. Mazur, *Opt. Lett.* **26**, 93 (2001).

10. M. Watanabe, S. Juodkazis, H.-B. Sun, S. Matsuo, H. Misawa, M. Miwa, and R. Kaneko, *Appl. Phys. Lett.* **74**, 3957 (1999).

11. K. M Davis, K. Miura, N. Sugimoto, and K. Hirao, *Opt. Lett.* **21**, 1729 (1996).

12. K. Miura, J. Qui, H. Inouye, T Mitsuyu, and K. Hirao, *Appl. Phys. Lett.* **71**, 3329 (1997).

13. D. Homoelle, S. Wielandy, A. L. Gaeta, N. F. Borrelli, and C. Smith, *Opt. Lett.* **24**, 1311 (1999).

14. D. Du, X. Liu, G. Korn, J. Squier, and G. Mourou, *Appl. Phys. Lett.* **64**, 3071 (1994).

15. B. C. Stuart, M. D. Feit, S. Herman, A. M. Rubenchik, B. W. Shore, and M. D. Perry, *J. Opt. Soc. Am. B* 13, 459 (1996); *ibid.*, *Phys. Rev. B* **53**, 1749 (1996).

16. M. Lenzner, J. Kruger, S. Sartania, Z. Cheng, Ch. Spielmann, G. Mourou, W. Kautek, and F. Krausz, *Phys. Rev. Lett.* **80**, 4076 (1998).

17. C. Schaffer, A. Brodeur, and E. Mazur, "Laser induced breakdown and damage in trasparent materials using tightly-focused femtosecond laser pusles," to appear in *Measurement Science and Technology* (expected 2001).

18. J. Qiu, K. Miura, and K. Hirao, *Jpn. J. Appl Phys* **37**, 2263 (1998).

19. E. N. Glezer and E. Mazur, *Appl. Phys. Lett.* **71**, 882 (1997).

20. H. Varel, D. Ashkenasi, A. Rosenfeld, M. Wahmer, and E. E. B. Campbell, *Appl. Phys. A* **65**, 367 (1997).

21. D. Ashkenasi, H. Varel, A. Rosenfeld, F. Noack, and E. E. B. Campbell, *Appl. Phys. A* **63**, 103 (1996).

22. These objectives are available from several companies, including Zeiss, Leica, and Nikon.

23. M. J. Soileau, W. E. Williams, M. Mansour, and E. W. Van Stryland, *Opt. Eng.* **28**, 1133 (1989).

24. J. H. Marburger, *Prog. Quantum Electron.* **4**, 35 (1975).

25. A. L. Gaeta, *Phys. Rev. Lett.* **84**, 3582 (2000).

26. S. H. Cho, U. Morgner, F. X. Kartner, E. P. Ippen, J. G. Fujimoto, J. E. Cunningham, and W. H. Knox, *OSA Technical Digest: Conference on Lasers and Electro Optics* **99**, 470 (1999).

27. A. R. Libertun, R. Shelton, H. C. Kapteyn, and M. M. Murnane, *OSA Technical Digest: Conference on Lasers and Electro Optics* **99**, 469 (1999).

28. D. N Fittinghoff, J. A. Squier, C. P. J. Barty, J. N. Sweetser, R Trebino, and M. Müller, *Opt. Lett.* **23**, 1046 (1998).

29. J. A. Squier and M. Müller, *Applied Optics* **38**, 5789 (1999).

30. J. P. Callan, A. M.-T. Kim, L. Huang, and E. Mazur, *Chem. Phys.* **251**, 167 (2000), and references therein.

31. M. Douay, W. X. Xie, T. Taunay, P. Bernage, P. Niay, P. Cordier, B. Poumellee, L. Dong, J. F. Bayon, H. Poignang, and E. Delevaque, *J. Lightwave Technol.* **15**, 1329 (1997).

32. H.S. Carslaw and J. C. Jaeger, *Conduction of Heat in Solids* (Oxford, London, 1959), p. 256.

33. M. Lenzner, J. Krüger, W. Kautek, and F. Krausz, *Applied Physics A* **69**, 465 (1999).

34. A. Rosenfeld, M. Lorenz, R. Stoian, and D. Ashkenasi, *Applied Physics A* **69** [Suppl], S373 (1999).

35. C. B. Schaffer, A. Brodeur, N. Nishimura, and E. Mazur, *Proc. SPIE* **3616**, 143 (1999).

Chapter 5

White-light generation

Continuum generation is a well-known and often-used nonlinear optical effect. Loosely focusing femtosecond laser pulses into a small vial of water produces continuua spectra that span the full visible range, making a very powerful spectroscopy tool. Despite widespread use of the continuum, the mechanisms for continuum generation remain largely unknown and misunderstood. In this chapter we discuss some recent experimental results on the dependence of the continuum spectrum on laser and material parameters. These dependencies help to rule out some of the contending theories of continuum generation.

The continuum is generated when femtosecond pulses with about a microjoule of energy are loosely focused into a transparent material. Typically, material damage is not observed. In Chapter 4 we saw that by tightly focusing the same pulse into a transparent material, permanent damage is produced. No continuum was observed for these tightly-focused pulses. The two processes of continuum generation and material damage seem to be somewhat mutually exclusive, with the strength of the focusing being the primary parameter that connects the two regimes. In Section 5.5, we present some preliminary

data that explores the dependence of the continuum and material damage on external focusing.

5.1 Historical survey of continuum results

Focusing a powerful, near infrared, femtosecond pulse into a transparent material can transform the pulse into a white-light continuum.[1 - 9] The spectrum of the pulse then stretches across and beyond the visible spectral range — making it one of the most spectacular phenomena in nonlinear optics. Most of this spectral broadening occurs on the blue (anti-Stokes) side of the pump frequency, forming a long spectral wing that ususally terminates in a sharp cutoff. This cutoff frequency, interestingly, is the only continuum feature to vary significantly with host material. This fact and the enormous spectral extent of the continuum have fascinated and confounded researchers for decades. Understanding how the continuum is generated would not only allow its optimization, which is desirable in fields such as ultrafast spectroscopy or optical parametric amplification,[2] but would also provide a better understanding of ultrafast pulse propagation dynamics.

The first observation of the continuum by Alfano and Shapiro in the late 1960's was followed by lively debate over its origin.[1, 10] The contending theories were self-phase modulation (SPM) enhanced by ionization[3] and four-wave mixing.[4] A key observation was that continuum generation required power levels sufficient for catastrophic self-focusing and medium ionization.[5] With the advent of femtosecond lasers, which produced even broader continua, continuum generation was initially attributed mostly to SPM.[6, 7] However, the inadequacy of SPM theory was

demonstrated a few years later with continuum generation in pressurized gases.[8] Subsequent work on dispersive effects in the self-focusing of femtosecond pulses[11] led to the discovery of pulse splitting,[12, 13] space-time focusing,[14, 15] and a higher threshold for catastrophic self-focusing.[16, 17] The contribution of these short-pulse effects to continuum generation is still being investigated.

A recent study showed that the threshold for continuum generation coincides with the threshold for catastrophic self-focusing.[9] Continua generated just above that threshold[18] exhibit a very strong Stokes/anti-Stokes asymmetry.[9] For instance, in lithium fluoride the blue-frequency broadening is more than 10 times the red-frequency broadening, an asymmetry that cannot be explained by SPM theory.[7] The authors of Ref. [9] also found that the continuum width tends to increase with the medium's band gap. This observation, the first to relate the continuum width to a material parameter, suggests that ionization determines the continuum width.

A truly satisfying model for continuum generation remains to be established. The knowledge accumulated so far shows that such a model should include self-focusing and its associated dynamics in the femtosecond regime, as well as medium ionization. The model should reproduce the continuum's main spectral features, in particular the long blue wing that terminates in a sharp cutoff.[9, 19] Furthermore, the general features of the continuum, apart from the cutoff frequency, should not depend on the host material. A promising model to describe continuum generation is the nonlinear envelope equation (NEE)[20] modified to include the effects of multiphoton and avalanche ionization.[21]

5.2 Band gap and pump wavelength dependence of the spectral broadening

In this section, we show experimentally that the continuum width depends linearly on the frequency of the input laser pulse. In the next two sections, we then demonstrate that this dependence on pump frequency, as well as the known dependence on band gap, are consistent with simulations based on the modified NEE. Our goal is two-fold: first, we want to improve our understanding of the ultrafast continuum, in order to optimize it and gain insight into its generation mechanisms. Second, we want to validate the modified NEE as a model for continuum generation and as a broad tool to describe femtosecond pulse propagation.

We first investigate the continuum width's dependence on pump frequency and host medium. Figure 5.1 shows the setup used to produce tunable ~100-fs pulses with a two-stage optical parametric amplifier (OPA). The OPA is pumped by 100-fs, 800-nm laser pulses from a Ti:Sapphire chirped-pulse amplification laser chain. Down-conversion to near infrared frequencies is performed in two beta-barium borate (BBO) crystals, the first one seeded by a white-light continuum. Tunability in the visible frequency range is achieved by frequency-doubling the output of the OPA in a lithium-barium borate (LBO) crystal. To generate continua we focus the tunable beam into a sample using a 75-mm focal length lens (the input beam diameter is 1.3 mm at $1/e^2$ level). The pulse energy is attenuated to ~ 25% above the threshold for continuum generation (note that the continuum spectrum is not very sensitive to pulse energy, up to a few times the threshold energy). The continuum is then focused toward the input of a fiber spectrometer through

a diffuser plate in order to decrease alignment sensitivity. Figure 5.2 shows the continuum obtained with a 800-nm laser pulse in fused silica.
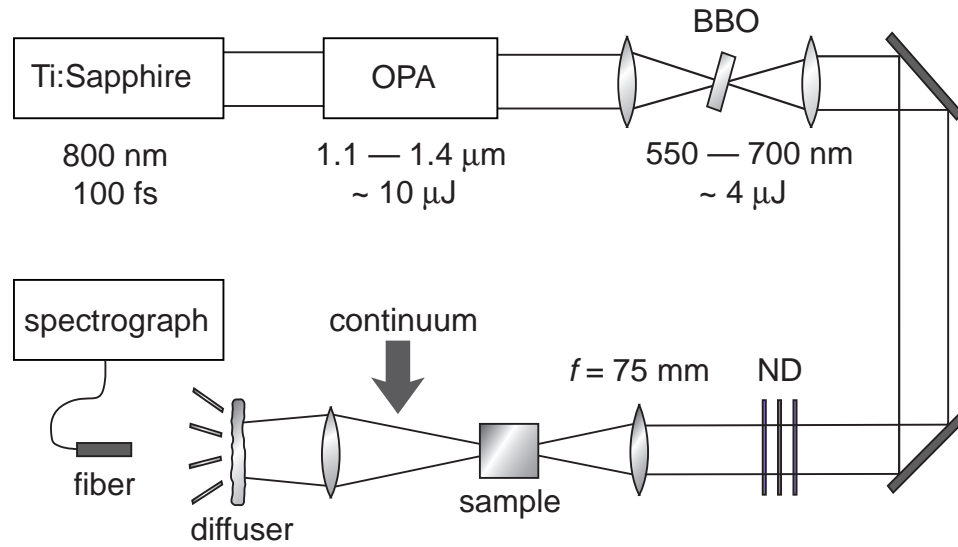
Figure 5.1 Experimental setup to measure the dependence of the continuum width on the pump frequency and host material. The output or frequency-doubled output of a femtosecond OPA is focused into various materials to produce continuum.
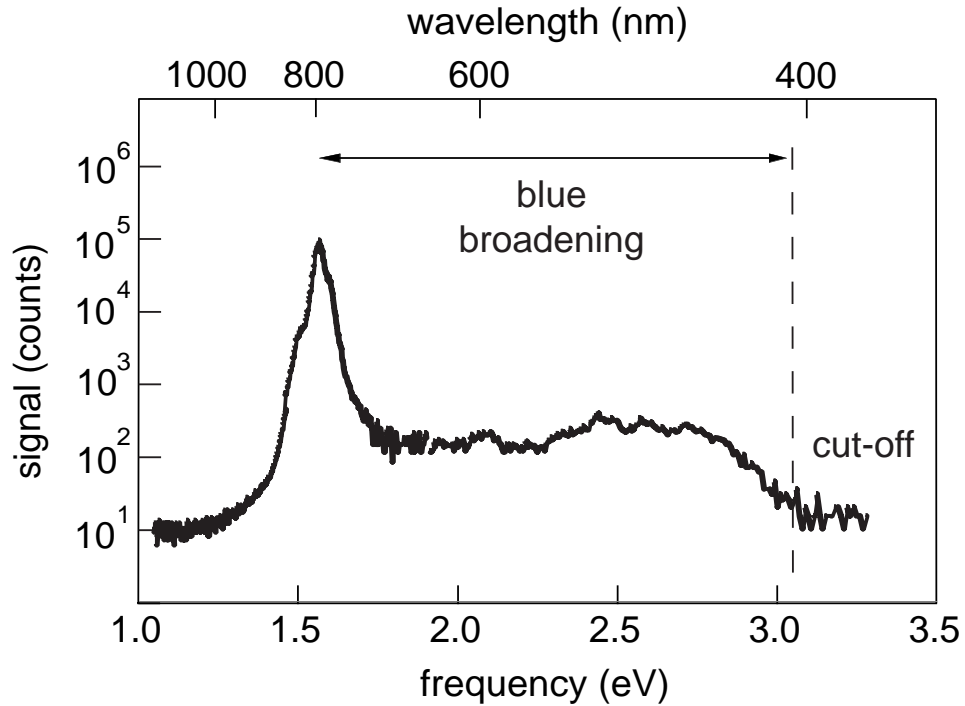
Figure 5.2 Continuum generated with a 100-fs, 800-nm pulse in fused silica.

For every continuum we recorded the blue (anti-Stokes) width $\Delta\omega_+$ of the spectrum, defined as the difference between the cutoff frequency and the laser frequency. The cutoff frequency is taken as the highest frequency where the amplitude is one order of magnitude smaller than the amplitude of the plateau. Figure 5.3 shows that, for all host materials, $\Delta\omega_+$ decreases in a linear manner with increasing laser frequency. Furthermore, the slope of this dependence is similar for all materials. This fundamental observation points to a universal continuum generation mechanism that does not depend strongly on material parameters. One can also see that for a given laser frequency, $\Delta\omega_+$ tends to increases with the material's band gap, in agreement with Ref. 9.
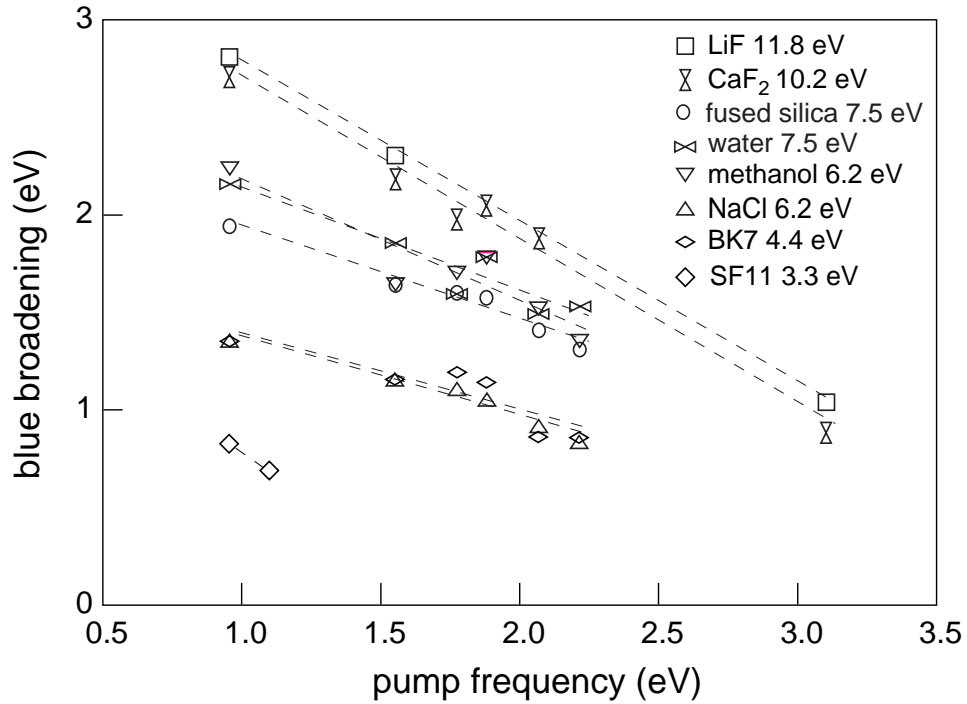
Figure 5.3 Measured continuum width vs. laser frequency for various host materials. The continuum width tends to decrease linearly with increasing laser frequency, and to increase with increasing band gap.

5.3 Mechanisms for continuum generation

To explain these observations we turn to simulations based on the modified NEE.[21] The modified NEE contains terms that account for diffraction, space-time focusing,[14, 15] dispersion, self-steepening,[22] the instantaneous and retarded Kerr index (intensity-dependent index of refraction),[22] avalanche ionization, multiphoton ionization, and plasma coupling. The main effects associated with these terms can be described in the following general manner:

SPM is a mechanism of spectral broadening, central to continuum generation, where the Kerr index causes the phase velocity to be lowest where the pulse is most

intense. This causes the pulse's wave train to be "compacted" at the back of the pulse (hence a blue shift) and "stretched" at the front of the pulse (hence a red shift). The extent of the broadening is determined by the peak intensity and the steepness of the pulse envelope. SPM is further discussed in Section 2.2.3

Self-focusing [22] is the spatial analog of SPM. As discussed in Section 2.2.2, the Kerr index causes a lensing effect which reduces the beam's transverse size and increases the peak intensity at the focus. Self-focusing enhances nonlinear effects such as SPM in the focus and is accompanied by the following short-pulse effects. *Pulse splitting* [12, 13] is a distortion of the pulse envelope that leads to the formation of two or more temporal spikes. It is caused by an interplay between dispersion and SPM. *Self-steepening* distorts the pulse envelope, causing a steep edge to develop at the back of the pulse. This effect can be viewed as an intensity-dependent group-velocity. The peak of the pulse has a slower group velocity than the leading and trailing edges, so the peak shifts to the back of the pulse. The steep back edge of the pulse produces a large blue broadening by SPM. *Space-time focusing* is a change in diffraction strength determined by the temporal steepness of the pulse envelope. In particular, the back and front of the pulse do not diffract the same way, increasing the intensity at the back of the pulse and thus enhancing blue broadening.

Ionization counteracts self-focusing, thus limiting the intensity achieved in the focus. As discussed in Section 2.3.4, the free electrons generated either by nonlinear photoionization or avalanche ionization contribute negatively to the index of refraction, thus forming a negative lens that compensates for the positive Kerr lens that causes self-

focusing. Ionization stops catastrophic self-focusing and determines the maximum intensity achieved in the focus.[23]

In the modified-NEE model, continuum generation arises from the rich interplay between the above mechanisms.[21] As the pulse self-focuses, the peak intensity increases and SPM broadens the spectrum. The continuum's long blue wing is generated when self-steepening and space-time focusing cause a steep, shock-like edge to form at the back of the pulse envelope. This steep edge builds a rapid phase shift by SPM, which translates into a blue-broadened spectrum. The broadening stops when sufficient free electrons are generated to stop self-focusing. The final width of the continuum is thus determined by the ionization rate, as proposed in Ref. 9.

5.4   Simulation results

Figure 5.4 shows the continuum generated in a simulation for a femtosecond pulse in fused silica, the medium for which material parameters are best known. The features of the simulated continuum are consistent with experiment: the spectrum exhibits a long blue wing that terminates in a sharp cutoff, the continuum propagates forward (i.e. on-axis), the blue frequency components lag temporally the red components, and the polarization is in the same direction as the polarization of the input pulse.[2] The extent of the blue broadening also agrees very well with experimental measurements (compare to Figure 5.2).
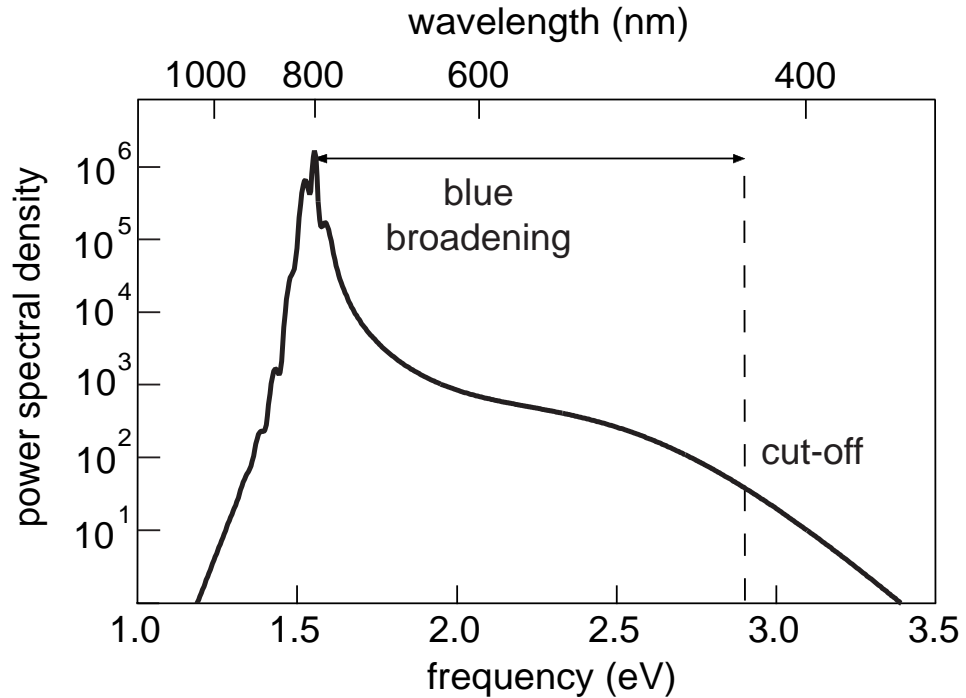
Figure 5.4 Simulation of the continuum generated with an 800-nm femtosecond pulse in fused silica. (Courtesy A. Gaeta)

Figure 5.5 shows the dependence of the simulated continuum width on pump frequency for fused silica. One can see that the width of the simulated continuum decreases in a linear fashion with increasing pump frequency, as in the experiment, albeit with a somewhat steeper slope. In the model, this dependence can be traced to the total rate of ionization (multiphoton and avalanche). The ionization rate increases with pump frequency, causing self-focusing to stop earlier. This limits self-steepening, space-time focusing and SPM, and therefore leads to a narrower continuum.
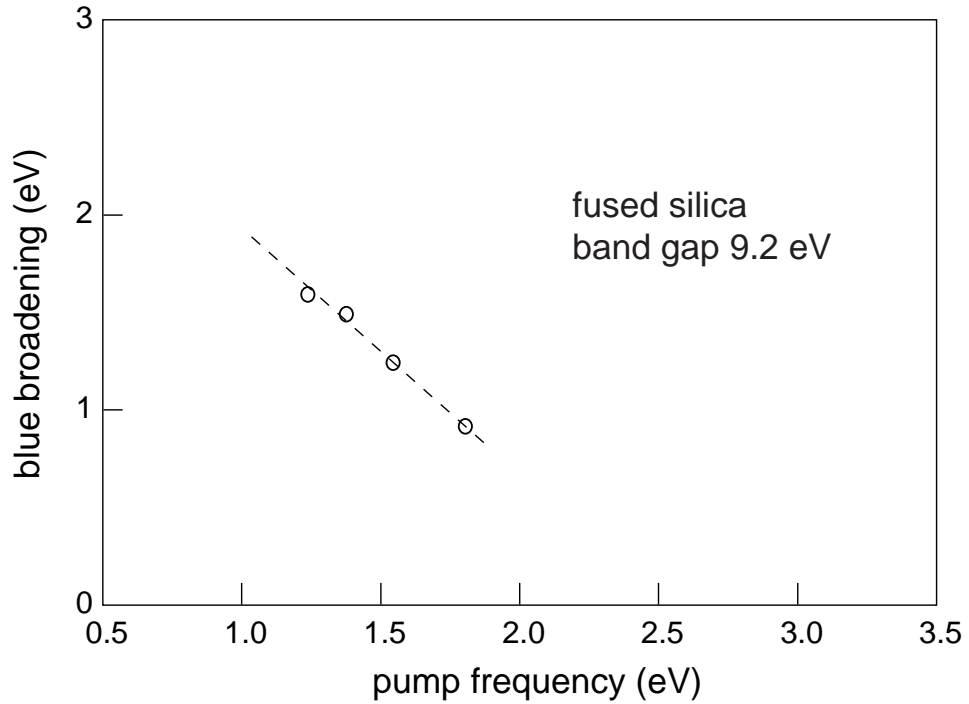
Figure 5.5 Simulated continuum width vs. laser frequency for a femtosecond pulse in fused silica. (Courtesy A. Gaeta)

One can see in Figure 5.5 that the simulated continuum is slightly narrower than the measured continuum. We attribute this discrepancy to the multiphoton ionization cross-sections used for the simulation. Those cross-sections, needed for several pump frequencies, are obtained from Keldysh theory.[24] However, a recent cross-section measurement for fused silica at $\omega_0=1.5$ eV yielded a value 6 orders of magnitude smaller than the Keldysh cross-section.[25] Using this cross-section would likely yield a wider continuum. Thornber's model was used to determine the avalanche ionization rates.[26] A better quantitative agreement between experiment and simulation could likely be achieved with knowledge of appropriate multiphoton and avalanche cross-sections at all pump frequencies.

The observed increase of the continuum width with the band gap is also consistent with the modified-NEE model. A larger band gap implies a lower ionization rate, which allows the development of a broader continuum. One also sees in Fig. 3a that for the 400-nm pump only CaF_2 and LiF produce a continuum. We can reasonably assume that in the other materials, which have smaller band gaps, multiphoton ionization causes an early arrest of catastrophic self-focusing and thus prevents continuum generation.

The modified-NEE model is thus an appropriate framework to explain continuum generation. The model agrees with all qualitative aspects of the continuum. Exact quantitative agreement between theory and experiment will require accurate knowledge of all the parameters involved in the simulation, especially the muliphoton and avalanche ionization cross-sections.

5.5   Effect of focusing angle

The continuum discussed in the previous sections and the bulk damage (at high laser energy) discussed in Chapter 4 are produced with virtually identical laser parameters. The primary difference between the two cases is the strength of the external focusing. The two processes of white-light generation and material damage seem to be somewhat mutually exclusive. Continuum generation is not observed up to very high laser energy under tight focusing conditions, and material damage is either not observed or has a very different morphology from the damage shown in Chapter 4 when white light is produced. In this section, we present some preliminary data that explores the role of focusing angle in continuum generation and material damage. These results will allow the continuum generation process to be optimized and will better define the parameter space where the

107

damage produced by femtosecond pulses can be used for micromachining. More importantly, these results will hopefully lead to a better understanding of the propagation of femtosecond laser pulses in transparent materials.

5.5.1   White-light or damage?

Bulk damage in transparent materials using femtosecond laser pulses was first studied in the mid-1990s. Glezer, *et al.* found that 300-nJ, 100-fs laser pulses focused by a 0.65 numerical aperture (NA) microscope objective produced permanently damaged regions in bulk fused silica.[27] In the same year, von der Linde, *et al.* reported that they were unable to produce damage in bulk fused silica with very high energy (1 mJ), 120-fs pulses focused by a 6-cm focal length lens.[28] They did observe some indications of color center formation in the laser-irradiated region, but no catastrophic damage (i.e. density changes, voids, or cracking) as is observed with longer laser pulses or with tighter focusing of femtosecond pulses. Von der Linde, *et al.* did observe continuum generation in their experiments, and they attributed the color center formation to a multiphoton absorption process. To explain the lack of material damge, they speculated that the femtosecond pulse produced a plasma that was sufficiently dense to defocus the laser pulse (and therefore limit the peak intensity), but not dense enough to produce material damage.

Two years after the work of Glezer and von der Linde, Efimov, *et al.* reported on color-center generation in silicate glasses irradiated by weakly-focused femtosecond pulses.[29] They observed continuum generation and did not observe any catastrophic bulk material damage. They concluded that the color centers are not formed by multiphoton absorption of infrared photons in the femtosecond pulse, but instead by one-

and two-photon absorption of the shorter wavelengths present in the continuum. Very recently, Gaeta concluded, based on simulations using the modified nonlinear envelope equation, that weakly-focused femtosecond laser pulses should not produce catastrophic material damage.[21] Gaeta's model confirms von der Linde's speculation that the electron plasma formed by nonlinear ionization defocuses the pulse, limiting the peak laser intensity in the material. Furthermore, Gaeta's simulations indicate that the plasma density required to produce this defocusing is well below the critical density. Because a critical density plasma is not formed, there is no mechanism for efficient energy deposition into the material, and damage is not produced (see Section 2.3.3). For tightly-focused femtosecond pulses, the external focusing is sufficiently strong to overcome the defocusing effects of the plasma, so higher laser intensities are reached in the material, producing a critical density plasma and leading to the deposition of a large fraction of the laser energy into the material and therefore to material damage.

As discussed in the previous sections, continuum generation results from the complex interplay of many nonlinear propagation effects. The development of a full continuum spectrum requires not only all the components discussed above, but also requires a relatively long interaction length. The laser pulse must propagate at a high intensity over several diffraction lengths for the optical shock to develop and produce the continuum.[21] For slow external focusing, self-focusing leads to just such a high-intensity filament. For tight external focusing, however, self-focusing cannot win over diffraction and the laser intensity is only high over the Raleigh range of the focusing lens. Because the high-intensity region is so short, self-phase modulation and optical shock formation do not occur, so continuum generation is not observed.

So far, a systematic study of the threshold for and nature of the continuum as a function of the numerical aperture of the external focusing lens has not been presented. Similarly, the dependence of the threshold for or morphology of material damage on the numerical aperture has also not been reported. The particular cases that have been investigated and the general comments mentioned above indicate that there is a transition from a self-focusing dominated regime for slow external focusing where continuum is produced to a diffraction dominated regime for tight external focusing where material damage is produced. In the remainder of this section, we examine this transition experimentally.

5.5.2 Experimental setup and results

We measure the threshold for continuum generation and the extent of the blue broadening as a function of the NA of the external focusing lens. The output of an amplified Ti:Sapphire laser which produces 800-nm, 60-fs pulses is spatially filtered to produce a clean Gaussian beam profile. The beam is focused by singlet lenses of varying focal length or by microscope objectives of varying NA into a fused silica sample. The threshold for continuum is defined as the laser energy that results in a blue broadening to 700 nm. The spectrum of the continuum generated at 1.5 and 2.0 times this threshold are recorded using a fiber-coupled spectrometer. In cases where the continuum spectrum is observed to change when multiple pulses irradiate one spot in the sample, we continuously translate the sample during the measurement so that the laser pulse always irradiates pristine material.

Figure 5.6 shows the threshold for continuum generation as a function of NA in fused silica for 60-fs pulses. The threshold increases as the NA increases above about

0.07. The slight increase in threshold at low NA is possibly due to incomplete self-focusing in our 1-cm thick sample. For slower focusing, catastrophic collapse due to self-focusing requires a greater propagation distance, so the continuum requires a greater propagation distance to fully develop.
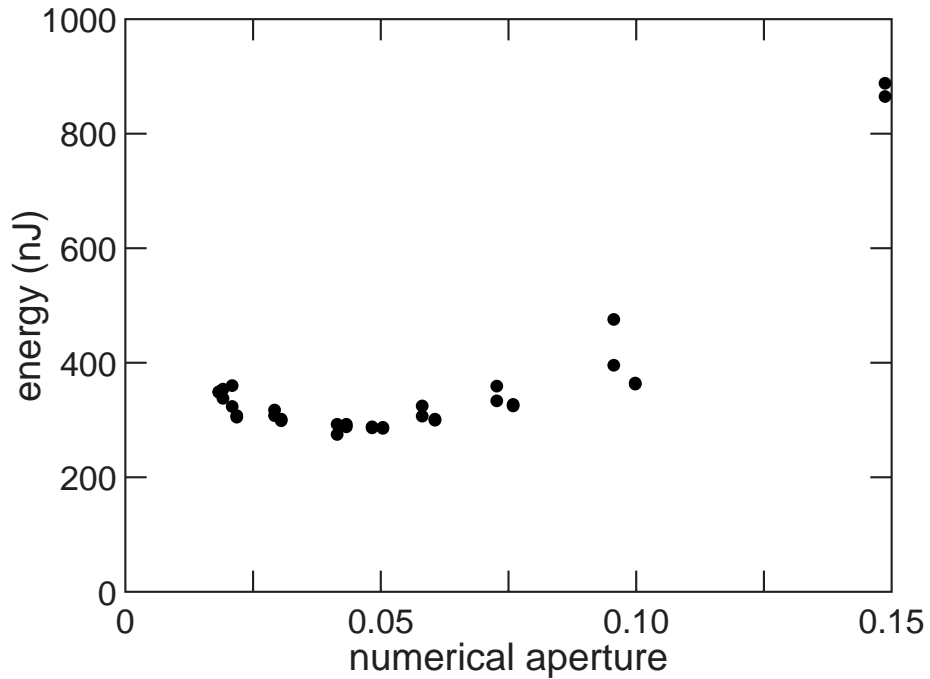
Figure 5.6 Threshold for continuum generation in fused silica for 60-fs, 800-nm laser pulses as a function of the NA of the external focusing lens.

More dramatic is the blue broadening as a function of NA, shown in Figure 5.7. The broadening decreases by 1 eV as the NA increases from 0.04 to 0.07. The continuum spectra for NA above 0.07 do not resemble the spectrum shown in Figure 5.2. There is no plateau, and the broadening to the red and blue side of the laser spectrum is more symmetrical. In addition, for NA higher than about 0.06, the blue broadening was observed to decrease with time if the laser beam continuously irradiated one spot in the

sample. Presumably, some sort of material change is produced which affects the continuum generation mechanism.
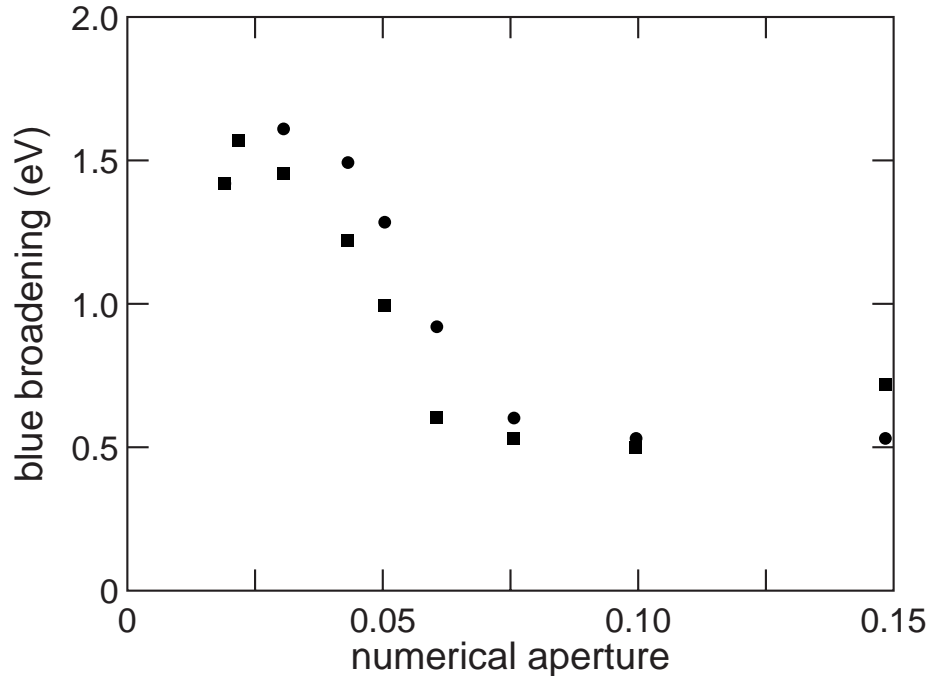
Figure 5.7 Continuum width as a function of NA for white light generated in fused silica using 60-fs, 800-nm laser pulses. The laser energy is 1.5 (■) and 2.0 (●) times the threshold energy shown in Figure 5.6

To further investigate the role of material changes (such as color centers) and catastrophic damage, we measured the threshold for permanent change in fused silica using the dark-field scattering technique discussed in Section 3.3.4. Figure 5.8 shows the continuum thresholds from Figure 5.6, the damage thresholds from Figure 3.4, and new thresholds for material change at NA below 0.1. The thresholds for material change and continuum generation cross around a NA of 0.07. For NA greater than 0.25, we have confirmed by optical microscopy that the material change consists of density changes

similar to those shown in Figure 4.2. These changes are produced with a single laser pulse incident on the material.

For the material change produced at NA less than 0.05, approximately 10,000 laser pulses must irradiate a single spot in the sample before any change is detected with the dark-field scattering setup. As shown in Figure 4.4, this is in contrast to the damage produced with tightly-focused pulses, where multiple pulses irradiating one spot in the sample do not increase the likelihood of producing detectable material change. We suspect that the material changes observed at low NA are color centers produced either by nonlinear absorption of the infrared laser photons or linear absorption of the blue tail of the continuum radiation. In BK7, a borosilicate glass, we easily observed the formation of colored filaments in the glass.

The nature of the material changes produced with NA between 0.07 and 0.2 is less clear. As noted above, the changes disrupt the continuum generation process, and appear to occur with just a few pulses incident on the sample. This abrupt appearance perhaps indicates that the material changes are catastrophic and similar to that observed with even tighter focusing. A careful analysis of the morphology of the material change produced under different focusing conditions is presently underway to determine the nature of these material changes.
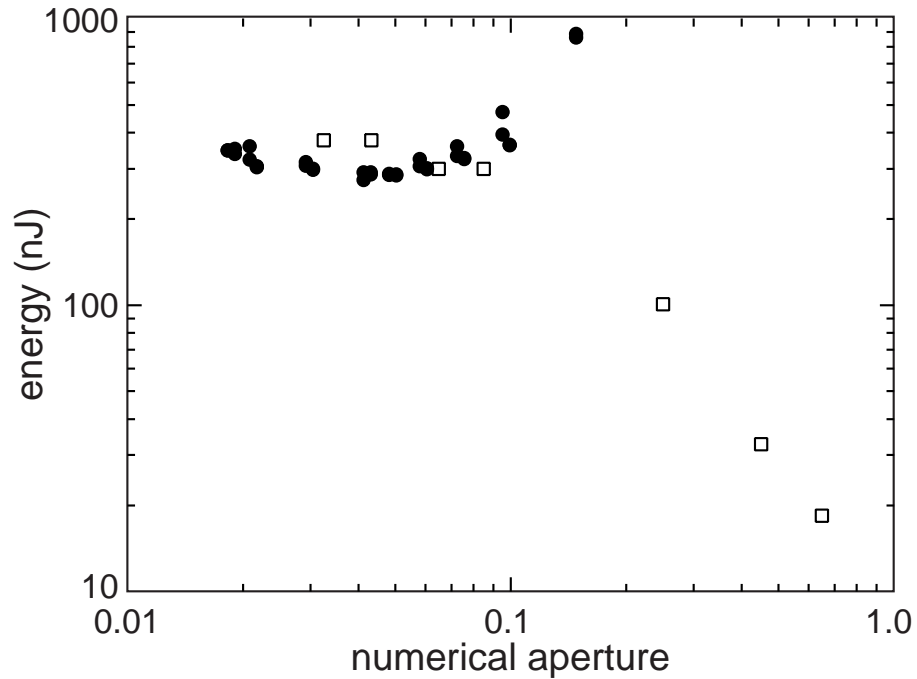
Figure 5.8 Threshold for continuum generation (●) and permanent material change (□) in fused silica for femtosecond laser pulses as a function of NA.

5.6 Conclusions

In summary, we uncovered the linear dependence of the continuum's width on laser frequency and showed that the modified-NEE model presented in Ref. 21 can explain this dependence, as well as the band gap dependence of the continuum. In this model the continuum is generated during critical self-focusing and is due mainly to SPM enhanced by self-steepening and space-time focusing, which cause the observed large blue broadening. Ultimately, the spectral width of the continuum is determined by ionization of the medium, which stops self-focusing and halts spectral broadening.

114

Motivated by the observation that identical femtosecond laser pulses produce either continuum or material damage if they are focused loosely or tightly into a transparent material, we examined the NA dependence of continuum generation and material change. We observed a decrease in the blue broadening, a change in the qualitative shape of the continuum spectrum, and an indication of catastrophic material damage, all appearing as the NA increases above 0.07. The coincidence of these changes in behavior at this NA signals a fundamental change in the nature of the interaction between the femtosecond laser pulse and the material. Further, more detailed, studies will provide important data for understanding this transition and femtosecond pulse propagation in transparent materials, in general.

References

1. R. R. Alfano and S. L. Shapiro, *Phys. Rev. Lett*. **24,** 584 (1970).

2. *The Supercontinuum Laser Source*, edited by R. R. Alfano (Springer-Verlag, New York, 1989).

3. N. Bloembergen, *Opt. Comm*. **8,** 285 (1973).

4. A. Penzkofer, A. Seilmeier, and W. Kaiser, *Opt. Comm*. **14,** 363 (1975).

5. W. L. Smith, P. Liu, and N. Bloembergen, *Phys. Rev. A* **15,** 2396 (1977).

6. R. L. Fork, C. V. Shank, C. Hirlimann, R. Yen, and W. J. Tomlinson, *Opt. Lett*. **8,** 1 (1983).

7. G. Y. Yang and Y. R. Shen, *Opt. Lett*. **9,** 510 (1984).

8. P. B. Corkum, C. Rolland, and T. Srinivasan-Rao, *Phys. Rev. Lett*. **57,** 2268 (1986). P. B. Corkum and C. Rolland, *J. Quant. Electron*. **25,** 2634 (1989).

9. A. Brodeur and S. L. Chin, *Phys. Rev. Lett*. **80,** 4406 (1998). A. Brodeur and S. L. Chin, *J. Opt. Soc. Am. B* **16,** 637 (1999).

10. The continuum beam observed by Alfano and Shapiro consisted of a central white part surrounded by concentric rainbow-like pattern (conical emission), where the emission angle increases with the detuning from the pump. Conical emission exists only at anti-Stokes frequencies. For clarity, the term "white-light

continuum" will hereafter refer to the low-divergence, central part of the beam and exclude the conical emission.

11. D. Strickland and P. B. Corkum, *Proc. Soc. Photo-Opt. Insturm. Eng.* **1413,** 54 (1991). D. Strickland and P. B. Corkum, *J. Opt. Soc. Am. B* **11,** 492 (1994).

12. J. Rothenberg, *Opt. Lett*. **17,** 583 (1992).

13. J. K. Ranka, R. W. Schirmer, and A. L. Gaeta, *Phys. Rev. Lett*. **77,** 3783 (1996).

14. J. Rothenberg, *Opt. Lett*. **17,** 1340 (1992).

15. J. K. Ranka and A. L. Gaeta, *Opt. Lett*. **23,** 534 (1998).

16. P. Chernev and V. Petrov, *Opt. Lett*. **17,** 172 (1992).

17. G. G. Luther, J. V. Moloney, A. C. Newell, and E. M. Wright, *Opt. Lett*. **19,** 862 (1994).

18. When projected on a screen the femtosecond continuum beam appears to the eye as a white disc with a blueish rim. At powers corresponding to a few threshold powers, the white disc is surrounded by conical emission.

19. The asymmetry is largest at peak powers just above threshold, where the continuum can be best studied: the spectrum is smooth, has no significant Raman contribution and is stable from shot to shot. Furthermore, the white-light beam has a high-quality spatial profile and there is no conical emission. In that regime self-

focusing leads to a single filament, i.e. there is no beam breakup due to small-scale filamentation.

20. T. Brabec and F. Krausz, *Phys. Rev. Lett.* **78,** 3282 (1997).

21. A. L. Gaeta, *Phys. Rev. Lett.* **84**, 3582 (2000).

22. J. H. Marburger, *Prog. Quant. Electron.* **4,** 35 (1975).

23. E. Yablonovitch and N. Bloembergen, *Phys. Rev. Lett.* **29,** 907 (1972).

24. L. V. Keldysh, *Sov. JETP* **20,** 1307 (1965).

25. M. Lenzner, J. Krüger, S. Sartania, Z. Cheng, Ch. Spielmann, G. Mourou, W. Kautek, and F. Krausz, *Phys. Rev. Lett.* **80,** 4076 (1998).

26. K. K. Thornber, *J. Appl. Phys.* **52**, 279 (1981).

27. E. N. Glezer, M. Milosavljevic, L. Huang, R. J. Finlay, T.-H. Her, J. P. Callan, and E. Mazur, *Opt. Lett.* **21**, 2023 (1996).

28. D. von der Linde and H. Schüler, *J. Opt. Soc. Am B* **13**, 216 (1996).

29. O. M. Efimov, K. Gabel, S. V. Garnov, L. B. Glebov, S. Grantham, M. Richardson, and M. J. Soileau, *J. Opt. Soc. Am. B* **15**, 193 (1998).

Chapter 6

Dynamics of laser-induced breakdown in water

Femtosecond laser-induced breakdown in transparent materials has attracted much attention in recent years. Nonlinear absorption of tightly focused femtosecond laser pulses inside transparent materials creates a high temperature plasma at the laser focus, providing an ideal means for the micromachining of solid materials,[1 - 3] and offering a more precise laser scalpel for photodisruptive surgery in both tissue and single cells.[4 - 6] Recent studies of laser induced breakdown in solids have focused on absorption mechanisms, threshold dependences on pulsewidth, and damage morphology.[7 - 10] In liquids, similar threshold measurements have been made, and the dynamics of pressure wave propagation and cavitation have been studied.[11 - 14] However, no reports discuss the very early time dynamics following breakdown in any condensed matter system. In this chapter, we present time-resolved imaging and time-resolved scattering techniques for measuring these early time dynamics, and discuss measurements made in water. We find that the initial expansion of the laser-produced plasma is delayed by 20 ps, in spite of its high temperature. We interpert this delay as an indication of the electron-ion energy transfer time. In addition, we track the dynamics over eight orders of magnitude in time, from the initial excitation of the plasma to the final collapse of the cavitation bubble,

providing the most complete picture obtained to date of the dynamics following laser-induced breakdown.

6.1 Introduction

We study the interaction of intense ultrashort laser pulses with transparent materials, i.e. materials that do not normally absorb the laser radiation. When a femtosecond laser pulse is tightly focused inside a transparent material the intensity in the focal volume can become high enough to cause absorption through nonlinear processes, as described in Chapter 3 and in Refs. [8] and [10]. Because the absorption is so strongly intensity dependent, it can take place at the focus inside the material while leaving the surface unaffected. Intially, the highly-excited free electrons created by the laser pulse remain confined to the micrometer-sized focal region because of the Coulomb attraction from the still undisturbed ions. Within ten picoseconds, however, energy is transferred from the free electrons to the ions. The result is a micrometer-sized, highly-excited plasma, trapped inside the material. If the plasma is hot enough, it explosively expands into the surrounding material with a velocity exceeding the speed of sound.

We measure the dynamics of this explosion using time-resolved imaging and scattering techniques. Imaging with a time-delayed laser pulse provides a direct view of the explosion dynamics, but, until now, has been limited to observing events on nanosecond and longer time scales because the spatial resolution of previous experiments was not sufficient to reliably image the early stages of the expansion, when the plasma is small.[5, 11, 13] Time-resolved scattering provides an indirect measure of the plasma

size that does not suffer from limited spatial resolution, but which requires more accurate knowledge about the plasma properties to properly interpret.

6.2   Pump-probe imaging

Figure 6.1 shows the time-resolved imaging setup. A 100-fs, 800-nm wavelength pump pulse is focused by a 0.65-NA microscope objective into a water flow cell. The resulting dynamics are imaged onto a CCD camera with a time-delayed probe pulse using the same microscope objective and a camera lens. For short time delays, the probe was a 100-fs duration, 400-nm wavelength pulse from the same laser, optically delayed with respect to the pump. For time delays longer than a few tens of nanoseconds we used an electronically triggered diode laser as the probe to avoid unreasonably long optical delay lines. The diode laser produced 100-ps pulses at a wavelength of 680 nm. The jitter between the pump and diode laser pulses was less than 10 ps. A spectral filter blocks the 800-nm pump pulse in both cases. A vibrating (~15 Hz) diffuser plate is used to reduce the speckle caused by the nearly monochromatic illumination of the probe pulse. The resolution limit of the imaging setup is approximately 4 μm.
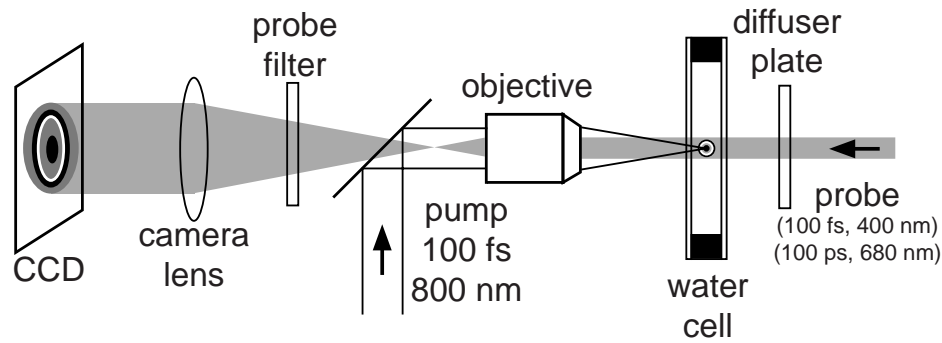
Figure 6.1 Time-resolved imaging setup for observing the dynamics of laser-induced breakdown. A time-delayed probe pulse illuminates the dynamics induced by the femtosecond pulse. The objective used to focus the femtosecond pulse images the dynamics onto a CCD camera.

A series of images of the breakdown dynamics in water probed at various time delays after excitation by a 1-µJ pump pulse is shown in Figure 6.2. The images shown were obtained with the 400-nm, 100-fs probe. Each image is the average of 100 CCD photographs. The 25-ps image shows a small bubble formed at early times which, after a delay of tens of picoseconds, grows rapidly. The rapid growth is evident from a comparison of the 25-ps and 100-ps images. The growth remains supersonic for a few hundred picoseconds, but by 400-ps is no longer supersonic, and all further dynamics occur at acoustic or slower velocities. In the 1.6-ns image we can begin to see the separation of an acoustic pressure wave from the central bubble. The pressure wave produces density variations in the water which translate to refractive index variations, providing the contrast seen in the figure. By 6.4 ns, the acoustic wave is clearly separated, and the central bubble has not expanded significantly compared to the 400-ps image. Using the diode laser probe, we see that, on a microsecond time scale, the central bubble expands and re-collapses as a cavitation bubble.

40 μm

– 10 ps

25 ps

100 ps

400 ps

1.6 ns

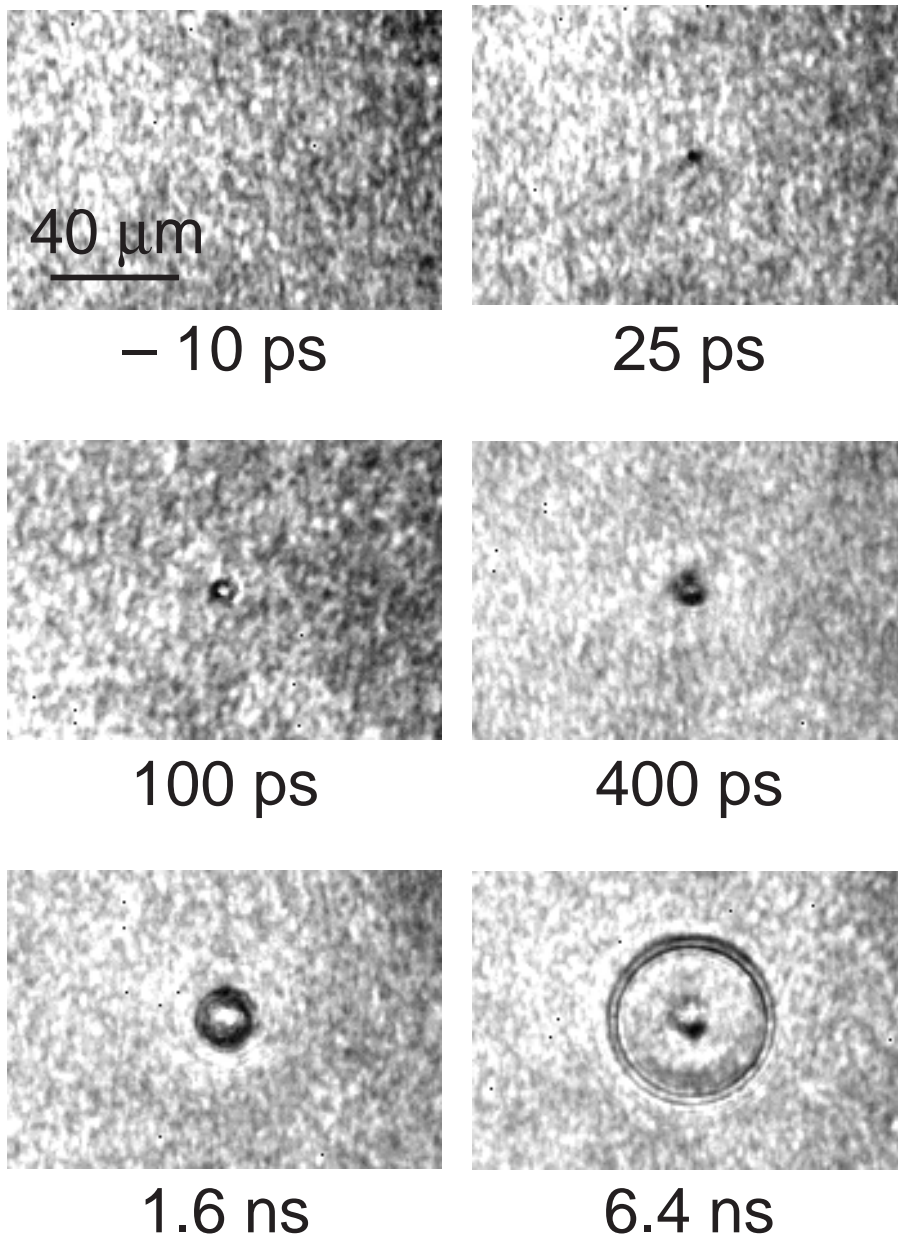6.4 ns

Figure 6.2 Images of femtosecond laser-induced breakdown in water obtained for various time delays using the setup shown in Figure 6.1.

Figure 6.3 shows the results of the imaging measurements in water over eight orders of magnitude in time. The filled circles and open squares are the radii of the bubble and pressure wave, respectively, obtained from the images. The graph shows that a hot

electron plasma with a radius of about 2 μm is formed within 200 fs. Note that this size is at our resolution limit, so the initial plasma size could be smaller. Until about 20 ps after excitation, the plasma mantains a constant radius, or, at least, remains smaller than the resolution limit of the imaging system. Beginning at about 30 ps and continuing to 200 ps, there is a very rapid increase in the size of the plasma. After this rapid growth the bubble radius begins to ring about a 6 μm radius. At about 800 ps, the images show that a pressure wave separates from the bubble, and travels outward at the speed of sound (1.48 μm/ns). The central bubble maintains its nearly constant radius until about 10 ns, when it begins to expand as a cavitation bubble. The cavitation bubble reaches a maximum radius of 100 μm at 5 μs, and then re-collapses by 11 μs. In previous studies of ultrashort pulse-induced breakdown in water the micrometer-scale picosecond dynamics were not resolved.[4, 12]
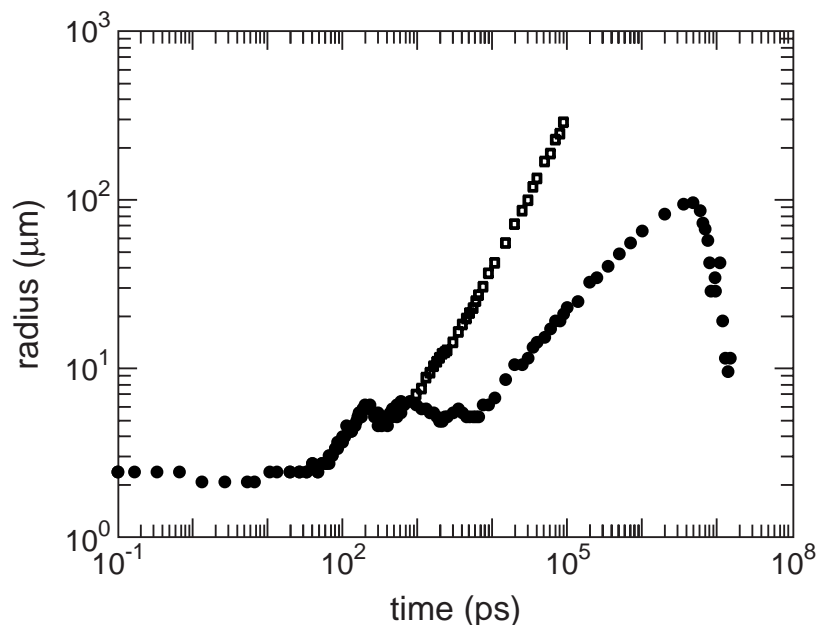
Figure 6.3 Evolution of the radius of the laser-produced plasma, pressure wave, and cavitation bubble as a function of time (● plasma/bubble radius, ❑ pressure wave).

6.3 Time-resolved scattering

In addition to the time-resolved imaging measurement described above, we measured the light scattered from the laser-produced plasma using a pump-probe technique. Figure 6.4 shows the setup used for time-resolved scattering measurements. A narrow probe beam illuminates an area of about 30-µm diameter around the center of the pumped region. The directly transmitted probe beam is blocked, so that only light that is scattered out of the undisturbed beam path and travels around the beam block is registered by the detector.
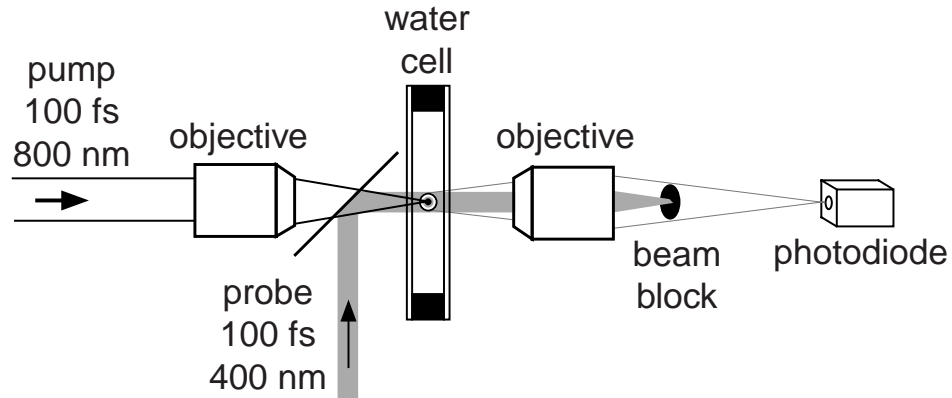
Figure 6.4 Time-resolved scattering setup. The directly transmitted probe beam is blocked so that only scattered probe light reaches the detector.

Figure 6.5 shows the time-resolved scattering signal from the plasma from 100 fs to 10 ns. The scattering signal shows similar features to the imaged radius shown in Figure 6.3. The rise time of the scattering signal indicates that the plasma is formed within 200 fs. Because plasma formation should occur within the duration of the pump pulse, this 200-fs rise time serves as a characterization of the temporal resolution of the setup. We observe the same ~ 20-ps delay before the scattering signal increases that we observe in the imaged radius. The increase in the scattering signal from 30 ps to 200 ps is very rapid, as for the imaged radius.

The amplitude of the scattered signal depends on the size of the plasma and on the density of the plasma. It is difficult to deconvolve these two dependencies without additional measurements. In particular, a measurement of the time-resolved transmission and reflection from the plasma would allow the plasma density as a function of time to be determined. With the plasma density known, the scattering signal would provide a measure of the plasma size, without the image resolution limits of the time-resolved imaging technique. If we assume that the plasma density is always above the critical

126

density for the 400-nm probe light (about 10^{22} cm^{-3}), then the plasma acts like a metallic ball, and the scattered amplitude is proportional to the cross-sectional area of the plasma. We can then use the imaged radius from 100 ps to 1 ns to calibrate the scattering signal. The axis on the right of Figure 6.5 shows the radius obtained using this procedure. The radius in the plateau region from 200 fs to 20 ps, at 0.8 μm, is smaller than that determined from the imaging experiment. This is consistent with the fact that the resolution of the imaging setup was not sufficient to resolve such a small plasma.
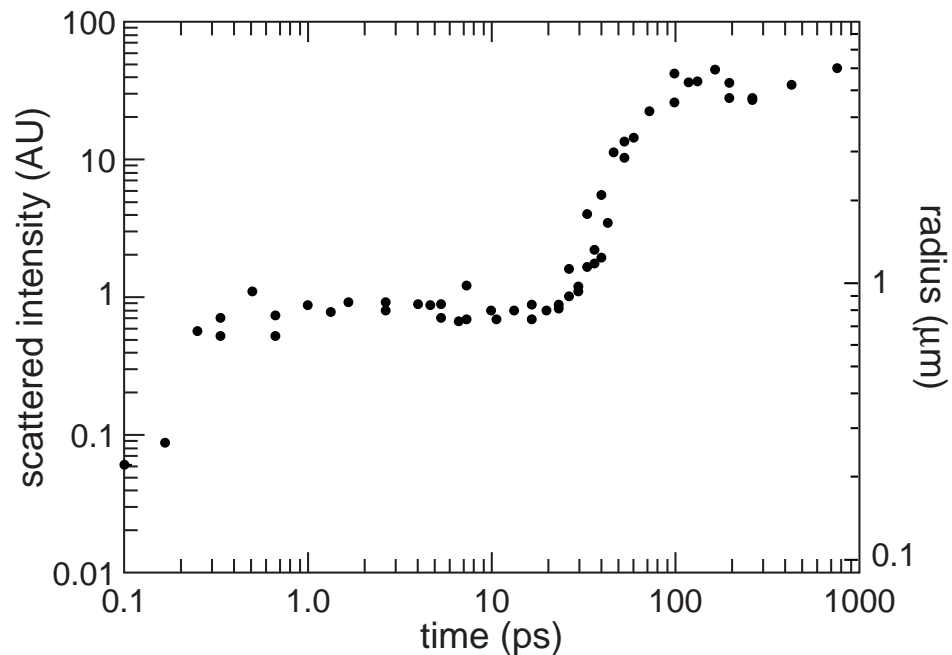

Figure 6.5 Time-resolved scattering signal from femtosecond laser-induced breakdown in water. The axis on the right assumes the plasma density is always sufficiently high that the scattered intensity depends only on the cross-sectional area of the plasma. The imaged radius is then used to calibrate the scattering signal in the 100 ps to 1 ns region.

6.4   Discussion

Some features of the dynamics shown in Figure 6.3 and Figure 6.5 are easily explained. The laser-produced plasma is very hot compared to the surrounding material, so it tends to expand, doing work on the surrounding material. The plasma expansion stops when the kinetic energy of the plasma has been used up doing this work. As the plasma expansion stops, it launches a pressure wave which propagates outward. We first observe the separation of the pressure wave at about 800 ps. After about 10 ns, the electron-ion plasma recombines, and much of the ionization energy ends up as heat. Thus, we are left with a hot gas which expands as a cavitation bubble, once again doing work on the surrounding material. The expansion stops and reverses as the gas cools. The main observations that remain to be explained are the 20 ps delay before expansion begins, the extremely rapid growth of the plasma size from 30 ps to 200 ps, and the launch of the pressure wave at 800 ps even though the plasma growth seems to stop at 200 ps.

The plateau in the radius from 200 fs to 20 ps indicates that the electron plasma produced by the laser pulse does not expand immediately after the excitation. We attribute this 20-ps delay to the electron-ion energy transfer time. Most of the electrons in the hot plasma cannot expand on their own because the electrons do not have enough kinetic energy to overcome the electrostatic attraction of the colder ions. Once the electrons transfer sufficient kinetic energy to the ions, the hot ions and electrons expand together without charge separation. Similar electron-ion energy transfer times have been observed in semiconductors.[15]

If we take the increase in size of the plasma from 30 ps to 100 ps to be due to physical expansion of the plasma produced by the laser pulse at the laser focus, we find

an enormous expansion velocity of 30 μm/ns, 20 times the speed of sound in water. An actual expansion of the plasma with this velocity is highly unlikely. The pressure required to drive such a shock wave is enormous, on the order of 10 GBar.[16]

We can set an upper limit on the pressure using the procedure outlined by Glezer in Ref. [7]. After electron-ion energy equilibration, we can estimate the temperature and pressure of the plasma using simple thermodynamic arguments. The temperature, T, is related to the deposited energy, E, by

$$T = \frac{E}{C_V V \rho} \qquad (6.1)$$

where C_V is the heat capacity at constant volume, V is the volume energy is deposited into, and ρ is the density. The heat capacity at constant volume is valid as a rough approximation well above the ordinary melting and vaporization temperatures because volume remains constant during the ion heating process.[17] For water, $\rho = 1$ X 10^3 kg/m^3 and $C_V = 4$ X 10^3 J/kgK. The incident laser energy is 1 μJ, and we take the absorption to be 50%, which is consistent with the transmision of femtosecond pulses above the breakdown threshold in other transparent materials (see Section 3.3.2). To get an upper estimate on the temperature, we take the focusing to be diffraction-limited. For a 0.6 NA objective, this gives us a spot diameter of about 0.5 μm, and a confocal parameter of about 1.9 μm, giving a focal volume of 1.5 μm^3. This yields a temperature of 8 X 10^4 K. Even though it is still at solid density, at this temperature the water behaves like an ideal gas, so we calculate the pressure based on the ideal gas equation and find a pressure of about 400 kBar. While this is an enormous pressure, it is not sufficient to drive a 30 km/s shock wave. Most likely the conditions are actually less extreme because spherical

aberration due to focusing through the 170 μm thick glass wall of the water cell plus about 200 μm of water increases the spot size in the sample, decreasing the temperature and pressure.[18] Because the peak power of a 1-μJ, 100-fs laser pulse is above the critical power for self-focusing in water, self-focusing most likely also modifies the spatial profile of the laser beam.[19]

The plasma formed at the laser focus by the laser pulse begins to expand after electron-ion energy equilibration, but the expansion velocity is much lower than the growth of the plasma size shown in Figure 6.3 and Figure 6.5. It is also worth noting that the pressure wave is not launched until 800 ps after excitation, after the plasma size goes through a small oscillation. If the rapid growth of the plasma size from 30 ps to 200 ps were an expansion of the electron-ion plasma produced by the laser pulse, one would expect a pressure wave to be launched at the end of the expansion, not 600 ps later. Perhaps the actual expansion of the electron-ion plasma produced by the laser pulse takes 800 ps, and it launches the pressure wave when the expansion runs out of energy and stops. This expansion would have a velocity of 5.2 μm/ns or 3.5 times the speed of sound. The pressure required to drive this supersonic expansion is about 110 kBar,[18] well within the upper limit set by the calculation above. It seems likely, then, that the expansion of the laser-produced plasma is much slower than the growth of the plasma size observed in the imaging and scattering experiments, and that the end of the growth of the laser-produced plasma is indicated by the launch of the pressure wave. The question then, is what is responsible for the very rapid growth in the plasma size that we observe.

Most likely, some mechanism induces plasma formation outside the focal volume. Perhaps the ultraviolet component of the radiation emitted by electron-ion recombination

in the laser-produced plasma ionizes material outside the focal region. We would see the electron plasma formed in this way when its density approached the critical plasma density for the probe wavelength, where the plasma becomes highly absorptive and reflective. Based on measurements with a photodiode, the visible component of the plasma radiation has a 5-ns lifetime. Perhaps the ultraviolet component has a shorter lifetime, explaining the halt of plasma growth after 200 ps.

Ballistic transport of the very high energy tail of the electron distribution produced by the laser pulse out of the focal volume could also lead to dense plasma formation outside the irradiated region. Each of these hot electrons could ionize many additional electrons by impact ionization, raising the plasma density outside the focal region. We do some rough calculations to determine the feasibility of this mechanism. We first estimate how energetic the high energy tail of the laser-produced electron distribution is, then see how far these electrons can run ahead of the ionic cores against the Coulomb force and how many additional electrons we expect them to make by avalanche ionization.

First, we have to decide on what we take the laser-produced electron density to be. A lower limit is the critical density for the pump laser wavelength, about 10^{21} cm^{-3} in our case. As discussed in Section 2.3.3, at the critical density the plasma becomes strongly absorbing at the laser wavelength, allowing efficient deposition of laser energy into the plasma. It is this energy deposition that heats the electrons and provides the energy that drives the subsequent mechanical effects that we observe. The upper limit on the electron density is about 10^{23} cm^{-3}, as this is the density of bonding electrons in water. For these calculations, we split the difference and take a plasma density of 10^{22} cm^{-3}.

Immediately following laser excitation, all of the energy deposited by the laser pulse is in the electrons and the ions are still cold. To determine how hot the electrons are, we assume, as above, that 0.5 μJ of laser energy is deposited into a 1.5 μm^3 volume. We subtract away the energy necessary to produce an electron density of 10^{22} cm^{-3} in the focal volume, and distribute the remaining laser energy over all electrons. This gives an electron temperature of 180 eV. These electrons have a Fermi-Dirac distribution in free electron states, and we use the free-electron density of states.[20] Now, we calculate the energy of the highest 0.01% of the electrons in the distribution. This high energy tail sits above an electron energy of 1.75 keV. If we assume that this energy is all kinetic and is directed outward from the focal volume and that only the Coulomb force from the ions at the focal volume slows the electrons, then these electrons will travel about 5 μm out into the surrounding material before they are stopped. At 1.75 keV, each electron which escapes the focal volume can ionize about 250 more electrons by impact ionization. This would produce a plasma density of about 10^{19} cm^{-3} in a 5-μm radius volume around the laser focus. Although this density is below the critical density for the 400-nm probe, it is possible that we would still see it. Using a time-resolved imaging technique similar to the one described above, von der Linde, *et al.* estimated that they could detect a plasma density of about 10^{19} cm^{-3}.[21]

This ballistic electron transport would happen much faster than the expansion of the laser-produced electron-ion plasma, explaining the very rapid plasma growth observed between 30 ps and 200 ps. One would also not expect the ballistic electrons to launch a pressure wave when they stopped, which is consistent with our observations.

Additional measurements and theoretical work is necessary to fully explain the rapid plasma growth we observe from 30 ps to 200 ps.

6.5   Conclusions

The ultrafast laser-induced optical breakdown described in this report opens the door to a number of interesting new opportunities. Using a relatively simple femtosecond laser it is possible to carry out tabletop studies of confined, high-density, high-temperature plasmas. Because femtosecond laser-induced optical breakdown requires less energy and produce more confined damage than optical breakdown with longer pulses, it may find promising applications in ophtalmology, in retinal microsurgery, and in medical and biological experiments.[4 - 6] As shown in Figure 6.3, the region of supersonic expansion is limited to a 7-μm radius for 1-μJ, 100-fs pulses. In contrast, supersonic expansion over several hundred microns is often observed with breakdown induced with picosecond laser pulses.[6] Because this supersonic expansion would cause collateral tissue damage, femtosecond pulses offer much higher surgical precision. Applications of femtosecond pulses for tissue and single-cell surgery are discussed in Sections 7.4 and 7.5. In solids the breakdown leaves behind a permanently damaged region inside the material. This material damage is discussed extensively in Chapter 4.

References

1. E. N. Glezer, M. Milosavljevic, L. Huang, R. J. Finlay, T.-H. Her, J. P. Callan, and E. Mazur, *Opt. Lett*. **21**, 2023 (1996).

2. H. Varel, D. Ashkenasi, A. Rosenfeld, M. Wahmer, and E. E. B. Campbell, *Appl. Phys. A* **65**, 367 (1997).

3. X. Liu, D. Du, and G. Mourou,. *IEEE J. Quantum Electron*. **33**, 1706 (1997).

4. T. Juhasz, G. A. Kastis, C. Suarez, Z. Bor, and W. E. Bron, *Lasers Surg. Med.* **17**, 1 (1995).

5. J. P. Fischer, T. Juhasz, and J. F. Bille,. *Appl. Phys. A* **64**, 181 (1997).

6. B. Zysset, J. G. Fujimoto, C. A. Puliafito, R. Birngruber, and T. F. Deutsch, *Lasers Surg. Med*. **9**, 193 (1989).

7. E. N. Glezer and E. Mazur, *Appl. Phys. Lett.* **71**, 882 (1997).

8. M. Lenzner, J. Kruger, S. Sartania, Z. Cheng, Ch. Spielmann, G. Mourou, W. Kautek, and F. Krausz, *Phys. Rev. Lett*. **80**, 4076 (1998).

9. D. Du, X. Liu, and G. Mourou, *Appl. Phys B* **63**, 617 (1996).

10. B. C. Stuart, M. D. Feit, S. Herman, A. M. Rubenchik, B. W. Shore, and M. D. Perry, *J. Opt. Soc. Am. B* **13**, 459 (1996); *ibid. Phys. Rev. B* **53**, 1749 (1996).

11. E. N. Glezer, C. B. Schaffer, N. Nishimura and E. Mazur, *Opt. Lett*. **22**, 1817 (1997).

12. A. B. Doukas, A. D. Zwieg, J. K. Frisoli, R. Birngruber, and T. F. Deutsch, *Appl. Phys. B* **53**, 237 (1991).

13. A. Vogel, S. Busch, and U. Parlitz, *J. Acoust. Soc. Am.* **100**, 148 (1996).

14. Q. Feng, J. V. Moloney, A. C. Newell, E. M. Wright, K. Cook, P. K. Kennedy, D. X. Hammer, B. A. Rockwell, and C. R. Thompson, *IEEE J. Quantum Electron.* **33**, 127 (1997).

15. L. Huang, J. P. Callan, E. N. Glezer, and E. Mazur, *Phys. Rev. Lett.* **80**, 185 (1998).

16. A. Vogel, J. Noack, K. Nahen, D. Theisen, S. Busch, U. Parlitz, D. X. Hammer, G. D. Noojin, B. A. Rockwell, and R. Birngruber, *Appl. Phys. B* **68**, 271 (1999).

17. R. W. Hopper and D. R. Uhlmann, *J. Appl. Phys.* **41**, 4023 (1970).

18. A. Vogel, K. Nahen, D. Theisen, R. Birngruber, R. J. Thomas, and B. A. Rockwell, *Appl. Opt.* **38**, 3636 (1999).

19. J. H. Marburger, *Prog. Quantum Electron.* 4, 35 (1975).

20. N. W. Ashcroft and N. D. Mermin, *Solid State Physics* (Saunders College Publishing, Orlando, 1976) p. 44.

21. D. von der Linde and H. Schüler, *J. Opt. Soc. Am B* **13**, 216 (1996).

Chapter 7

Applications

7.1 Introduction

There are several applications of the work presented in this thesis. Here we discuss two topics that have been pursued in detail in the group. The first could be generally described as three-dimensional refractive index patterning of transparent materials. The techniques discussed in Chapter 4 can be used to produce refractive index changes in the bulk of a transparent material in any desired pattern. This refractive index pattern could be used to store information, it could form an optical device, or (in one actual application of this technology) it could be used to decorate a glass paperweight. This three-dimensional index patterning goes beyond the more standard surface micromachining with femtosecond lasers that has been extensively studied in recent years.[1, 2]   In Section 7.2 we briefly describe how waveguide beam splitters can be manufactured using femtosecond lasers, and in Section 7.3 we outline the implications of the low energy threshold for inducing a structural change discussed in Section 4.7 for three-dimensional refractive index patterning.

There are also biological applications of this work. Tissue and cells are transparent to the 800-nm wavelength of the Ti:Sapphire lasers used in this work. Thus one can induce nonlinear absorption and optical breakdown in biological samples in much the same way as in transparent solids. The laser can serve as a precise surgical scalpel capable of cutting in the bulk of tissue without damaging the surface or in the interior of a single cell without damaging the cellular membrane. We discuss the use of these techniques for sub-surface skin surgery in Section 7.4 and for the ablation of sub-cellular organelles inside single cells in Section 7.5.

7.2 Femtosecond laser micromachining

In recent years, femtosecond laser pulses have been used to micromachine a great variety of materials. Ultrashort pulses cleanly ablate virtually any material with a precision that meets or exceeds that of other laser-based techniques, making the femtosecond laser an attractive micromachining tool.[1, 2] In transparent materials, where micromachining relies on nonlinear absorption, femtosecond lasers allow three-dimensional microfabrication with sub-micrometer precision.[3, 4] These lasers can produce three-dimensionally localized refractive index changes in the bulk of a transparent material, opening the door to the fabrication of a wide variety of optical devices.

7.2.1 Machining waveguide splitters

Waveguides can be directly written into bulk glass by loosely focusing 1-µJ amplified femtosecond laser pulses into the sample using a 0.1-NA lens.[1 - 3] Irradiation with a single laser pulse produces a cylindrically-shaped structure similar to those in Figure 4.2

but with a larger diameter and length. By translating the sample at about 20 μm/s along the axis of a 1-kHz train of such pulses, the cylindrical structures connect smoothly, forming an optical waveguide. The low numerical aperture used in this technique allows waveguides to be written tens of millimeters inside the material.

By writing multiple waveguides close to each other, it is possible to produce a waveguide splitter. The waveguides must be close enough that their modes overlap and light can leak from one waveguide to another. We used a temporally decorrelated multifocal beamlet array[4 - 6] to write multiple waveguides into a sample simultaneously, making a waveguide splitter in one step.

We used a 0.1-NA, 10x aspheric lens and the beamsplitter array to produce 4 foci spaced by 10 μm. Using 1-μJ per beamlet, we machined sets of parallel waveguides by translating the 1-cm fused silica plate axially through the focus. The translation speed was 10 μm/s. We began machining with four beams and successively blocked beams during the machining process so that the number of waveguides goes from four to three to two to one inside the sample, with only one waveguide extended all the way through the sample. To show that this structure acts as a waveguide coupler, we polished the ends of the plate to remove pitting at the surface and coupled light from a He:Ne laser into the single waveguide end of the structure. Figure 7.1a shows an image of the near-field output mode of the waveguides. One can clearly see four distinct outputs. The waveguide that extends all the way through the sample into which light was coupled is on the right in the image. Figure 7.1b shows the near-field output mode of four waveguides written all the way through the fused silica sample using 2-μJ per beamlet and translating the sample at 20 μm/s. Light was again coupled into the waveguide on the right.
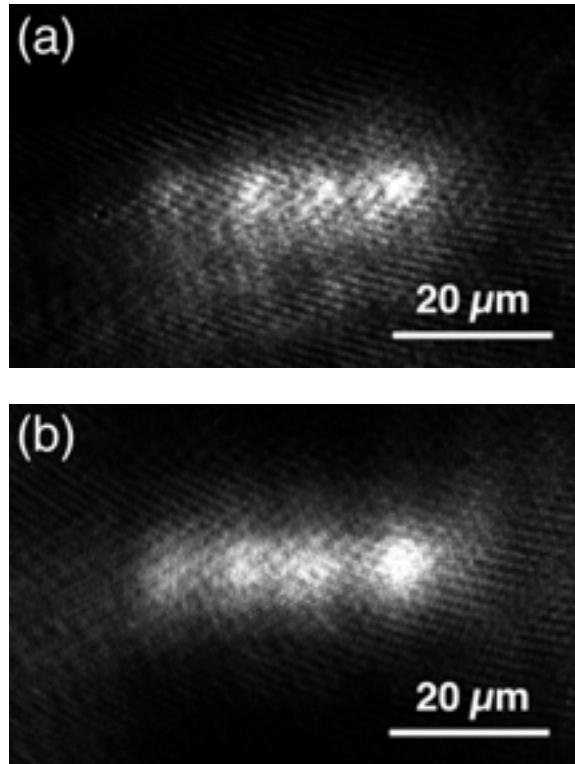
Figure 7.1 Images of the near-field output mode of waveguides written with femtosecond laser pulses. One can clearly see four distinct outputs. In Figure 7.1a, the waveguide that extends all the way through the sample into which light was coupled is on the right in the image. Figure 7.1b shows the near-field output mode of four waveguides written all the way through the fused silica piece using 2-μJ per beamlet and translating the sample at 20 μm/s. Light was again coupled into the waveguide on the right.

7.3 Oscillator-only micromachining

Until now micromachining of transparent materials required amplified laser systems. We recently found that transparent materials can also be micromachined using tightly focused trains of femtosecond laser pulses from an unamplified laser oscillator (see Section 4.7). In addition to reducing the cost and complexity of the laser system, femtosecond laser oscillators enable micromachining using a multiple-shot cumulative effect. In this section, we concentrate on two applications of oscillator-only micromachining of bulk

transparent materials that have been explored by our group: three-dimensional binary data storage and direct writing of optical waveguides.

7.3.1 Three-dimensional binary data storage

The structures shown in Figure 4.2 can be used as bits for three-dimensional binary data storage.[3, 7] The presence of a structure represents a "1" and the absence of a structure a "0." Multiple planes of data are written inside the same sample, with a minimum spacing of about 1 μm within a plane and about 5 to 10 μm between planes, depending on the microscope objective used to write the data. Readout is accomplished either with transmission, reflection, or scattered light microscopy using an objective whose confocal parameter is smaller than the spacing of data planes.

The oscillator-only machining discussed in Section 4.7 has important implications for this three-dimensional data storage application. In previous demonstrations, an amplified laser operating at kilohertz repetition rate was used to write the data. The structures shown in Figure 4.3b, however, can be produced with pulses from an unamplified, megahertz repetition-rate laser. Using an oscillator provides two major benefits. First, the cost of an unamplifed laser system is much smaller than an amplified laser. Second, the higher repetition rate of the oscillator allows writing speeds on the order of 50 Mbits/sec (for the 25-MHz oscillator described in Section 4.3.2).

7.3.2 Optical waveguide and device fabrication

The cumulative thermal effects discussed in Section 4.7 provide a new tool for micromachining transparent materials. A train of femtosecond laser pulses is focused into the bulk of the sample. Because of the high intensity at the focus, laser energy is

nonlinearly absorbed by the material in the focal volume. When this energy is absorbed at a rate faster than it is carried out of the focal volume by thermal diffusion, the material around the laser focus melts. After the pulse train is turned off or the focus is moved away, the material resolidifies nonunifomly because of the temperature gradients. This nonuniform resolidification produces density and refractive index changes in the material around the focal volume. Therefore, by scanning the laser focus of a continuous 25-MHz pulse train inside the sample, the refractive index can be changed in regions of any desired three-dimensional shape. We have used this technique to write diffraction gratings, single-mode optical waveguides, and waveguide splitters inside bulk Corning 0211 glass.[4]

Figure 7.2 illustrates how single-mode waveguides are written inside a slab of transparent material. A 1.4-NA oil-immersion microscope objective focuses a 25-MHz train of 30-fs, 5-nJ pulses about 100 μm beneath the surface of the sample which is translated at a speed of 20 mm/s in a direction perpendicular to the laser beam. The material surrounding the focus melts and then resolidifies after being moved away from the laser focus.
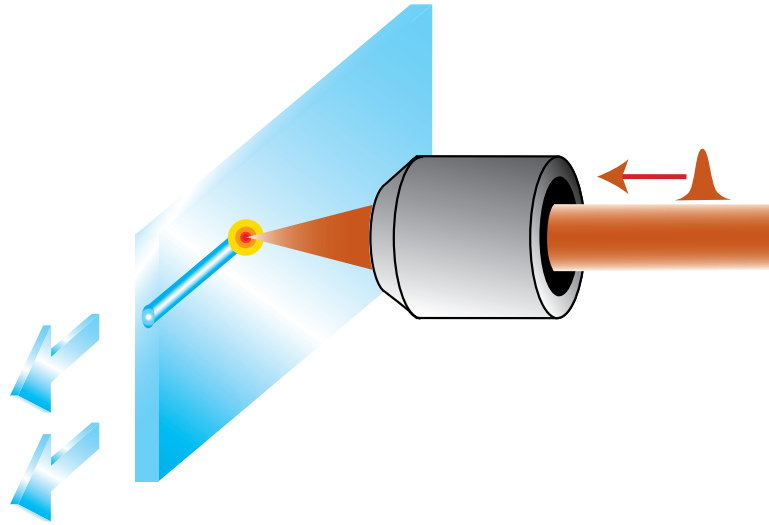
Figure 7.2 Procedure for directly writing waveguides inside bulk glass using a femtosecond laser oscillator. The sample is translated at 20 mm/s perpendicular to the incident direction of a 25-MHz train of 30-fs, 5-nJ laser pulses that are focused by a 1.4-NA microscope objective.

Figure 7.3 shows a DIC image of cylindrical structures produced using the technique described above. The cylinders form single-mode optical waveguides, indicating that the refractive index is higher at the center of the cylinder than in the surrounding material.[4] This change in refractive index suggests the glass at the center of the cylinder densifies as it cools. The inset in Figure 7.3 shows an end view of one of these waveguides after cleaving the glass to produce a clean face. The same ring structure as in Figure 4.8 is evident in the end view.
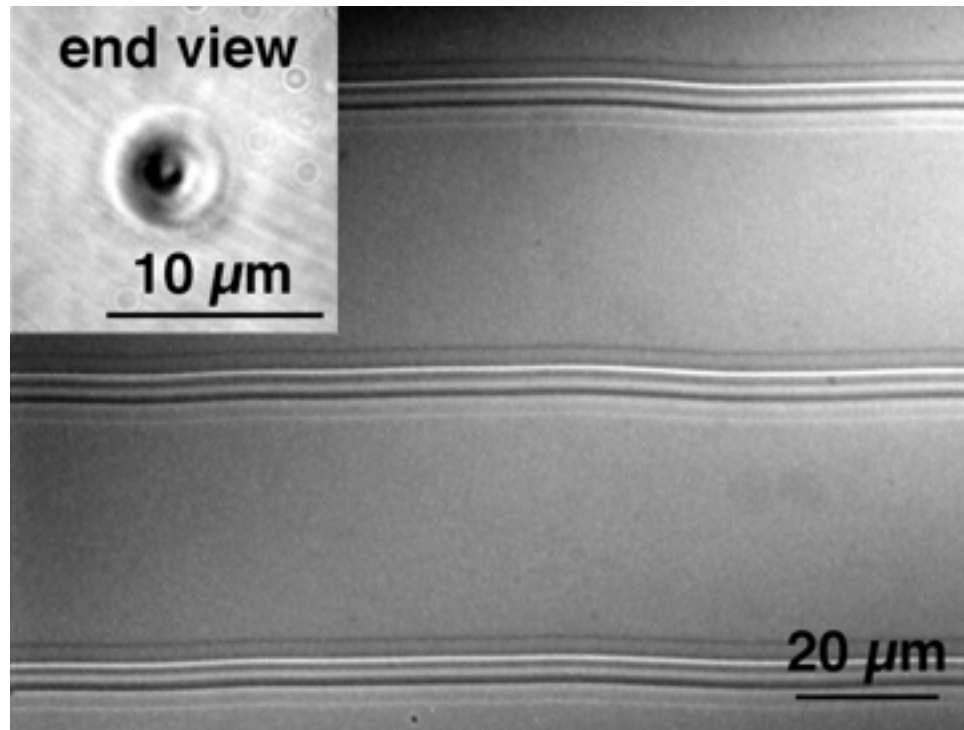
Figure 7.3 DIC optical microscope image of waveguides written inside bulk glass using the technique illustrated in Figure 7.2.

Figure 7.4 shows the near-field output profile of one of these waveguides for 633-nm laser light. Light from a He:Ne laser was coupled into a 10-mm long waveguide using a 0.25-NA microscope objective. The output end of the waveguide was imaged onto a CCD camera using a 0.65-NA objective. As the data show, the waveguide has a single-mode, near-Gaussian output profile for visible wavelengths. From the divergence of the waveguide output we find that the refractive index change between the core of the waveguide and the surrounding material is about 3×10^{-4}.
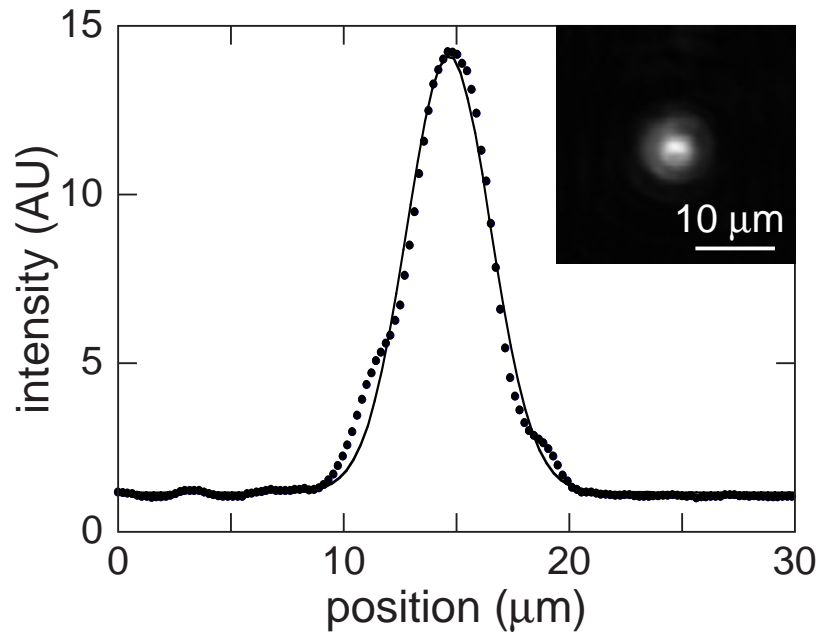
Figure 7.4 Waveguide output profile at 633 nm. The points correspond to a cross-section of the near-field mode and the curve represents a best-fit Gaussian. The inset shows a raw CCD image of the near-field mode.

More complex devices can be built up by combining single-shot and thermal micromachining. For example, Figure 7.5 illustrates how a three-dimensional waveguide splitter can be manufactured by intersecting three waveguides inside a transparent material. Some of the light coupled into one of the waveguides leaks to the other two at the intersection, making a waveguide beamsplitter. Because the three waveguides do not all lie in the same plane, it is very difficult to fabricate such a splitter using conventional, photolithographic techniques. Preliminary work in our lab has produced such a three-dimensional splitter that has three equal-intensity outputs. A periodic line of single-shot structures, like those shown in Figure 4.2, written inside the core of a waveguide could act as a Bragg grating which transmits only certain wavelengths. Using Bragg gratings of different periods in each of the waveguides in Figure 7.5, one could produce a

wavelength selective splitter. Three-dimensional photonic devices such as the wavelength selective splitter described above are important for the telecommunications industry. As we have shown, such devices can be produced with just a femtosecond laser oscillator. The cumulative thermal mechanism described above does not require a laser amplifier and offers a much higher machining speed than is possible with amplified lasers.
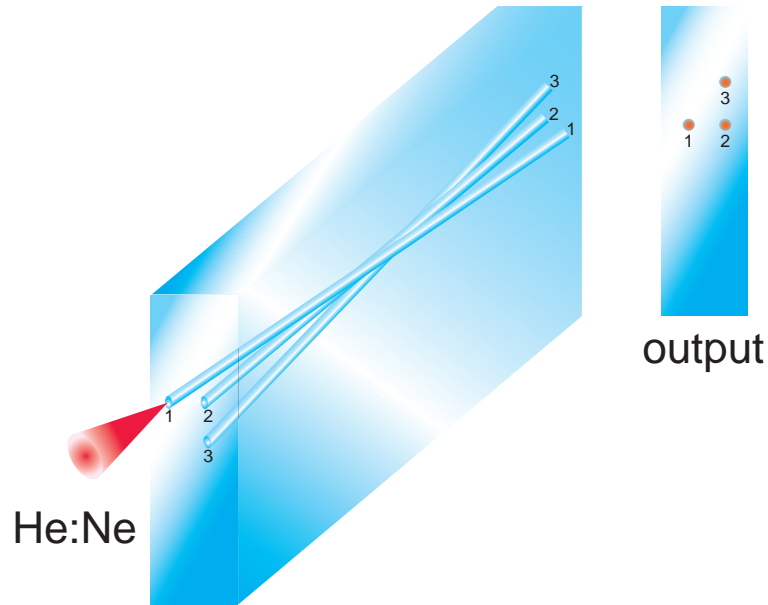
Figure 7.5 A three-dimensional waveguide splitter made by intersecting three waveguides in the bulk of a glass sample so that they cross each other. Light coupled into one of the waveguides leaks into the other two at the intersection, resulting in three outputs.

7.3.3   Bulk point source of heat

By exploiting the cumulative heating effect discussed in Section 4.7, a tightly focused train of femtosecond laser pulses can be used as a point source of heat located in the bulk of a transparent sample. The amount of energy that is deposited in a micrometer-sized volume can be controlled with nanojoule precision by varying the number of incident pulses. No other technique allows for such precise deposition of energy in such small

145

volumes in bulk material. In the previous section, we described how this point source of heat can be used to fabricate single-mode optical waveguides. There are other applications as well. One could, for example, induce thermally-driven chemical changes inside the bulk of a sample. If the solubility properties of the material were changed by the chemical reaction, a free-standing three-dimensional structure could be fabricated.

7.4   Femtosecond laser surgery

Ultrashort pulses may provide an ideal tool for laser surgery, especially in transparent (or nearly transparent) tissues, i.e., tissues that do not normally absorb the laser radiation. When a femtosecond laser pulse is tightly focused inside a transparent material, the intensity in the focal volume can become high enough to cause absorption through nonlinear processes.[8] Because the absorption is nonlinear, it takes place at the focus inside the material instead of at the surface. The absorption produces a micrometer-sized, highly-excited plasma trapped inside the material. This plasma can be used to precisely vaporize tissue while minimizing damage to surrounding tissue.

7.4.1   Review of mechanisms

Laser-induced tissue ablation is a multi-stage process. First, tissue is ablated by the hot plasma formed at the focal volume of the laser. Second, as discussed in Chapter 6, the plasma expands with supersonic velocity, and drives a shock wave.[9] As the shock wave propagates outward, it decays into an acoustic pressure wave[10]; the region of supersonic expansion is called the shock zone. Next, a cavitation bubble is formed by the expansion of vaporized material. The bubble expands outward from the focal region until,

after tens of microseconds, it collapses under external pressure. The laser-produced plasma vaporizes tissue, providing the surgical effect. However, both the shock wave and the cavitation bubble propagation create a surrounding region of partial damage due to mechanical disruption.[11, 12]

Most clinical applications employ 10-ns pulses from a Nd:YAG laser with pulse energies greater than 1 mJ. These pulses produce large shock zones which limit the surgical precision and cause collateral tissue damage.[13, 14] Furthermore, unwanted energy deposition can occur in any absorbing tissue outside the focal region.[13]

Several recent experiments [15 - 19] have shown that picosecond and femtosecond lasers produce smaller ablation regions as well as more limited shock zones and cavitation bubble sizes. Using the time-resolved imaging technique discussed in Chapter 6 and in Ref. [19] we find that the shock zone radius in water created by 10-μJ, 100-fs pulses is only 8.5 μm. In contrast, other researchers [10] have found that with picosecond pulses at the same laser energy the shock zone radius is 50 μm. Furthermore, with 1-mJ nanosecond pulses in saline solution the explosion front propagates at supersonic speeds for nearly 100 μm, and the cavitation bubble reaches a radius of ~500 μm.[20] The increased size of mechanical effects is due to the higher threshold for breakdown with longer pulses. Longer pulses require more energy to initiate breakdown, and thus when breakdown occurs they deposit more energy into the sample, leading to larger shock zones and cavitation bubbles.

In the following sections, we report on femtosecond and picosecond laser-induced breakdown in water and human skin tissue. In water, we find a much lower breakdown threshold for femtosecond pulses, with more consistent energy deposition near the

threshold. In skin, we investigate surface ablation and sub-surface cavity formation with both femtosecond and picosecond pulses. We find that similar size surface ablation is produced with both pulse lengths, but that the shorter pulses produce smaller sub-surface cavities. Furthermore, for both surface ablation and sub-surface cavity formation, the extent of collateral damage is greatly reduced by using femtosecond instead of picosecond laser pulses.

7.4.2   Thresholds for breakdown in water

Tissue is composed primarely of water, so measuring the dependence of the breakdown mechanisms and breakdown threshold on laser parameters in water provide results that are applicable to tissue. In water, breakdown thresholds were determined by measuring the laser energy required to launch a pressure wave which was detected acoustically.[19] We performed measurements using 100-fs and 200-ps, 800-nm pulses from an amplified Ti:Sapphire laser. A 0.65 numerical aperture (NA) objective is used to focus the pulses inside a water cell containing a submerged piezoelectric sensor (see inset to Figure 7.6). We amplify the piezoelectric voltage and record the signal on a digital oscilloscope. The amplitude of the response increases with increasing energy, but the shape of the response changes only slightly. Using the height of the first peak, we measure the magnitude of the pressure in the wave as a function of input energy. Figure 7.6 shows, on a logarithmic scale, the pressure produced by 100-fs and 200-ps pulses over three orders of magnitude in laser pulse energy. Above 10 μJ, the pressure produced by the 100-fs and 200-ps pulses is equal. In the range 10–100 μJ the logarithmic slope is 0.5, indicating that the pressure increases approximately as the square-root of the input energy and therefore that the deposited energy is proportional to the input energy.
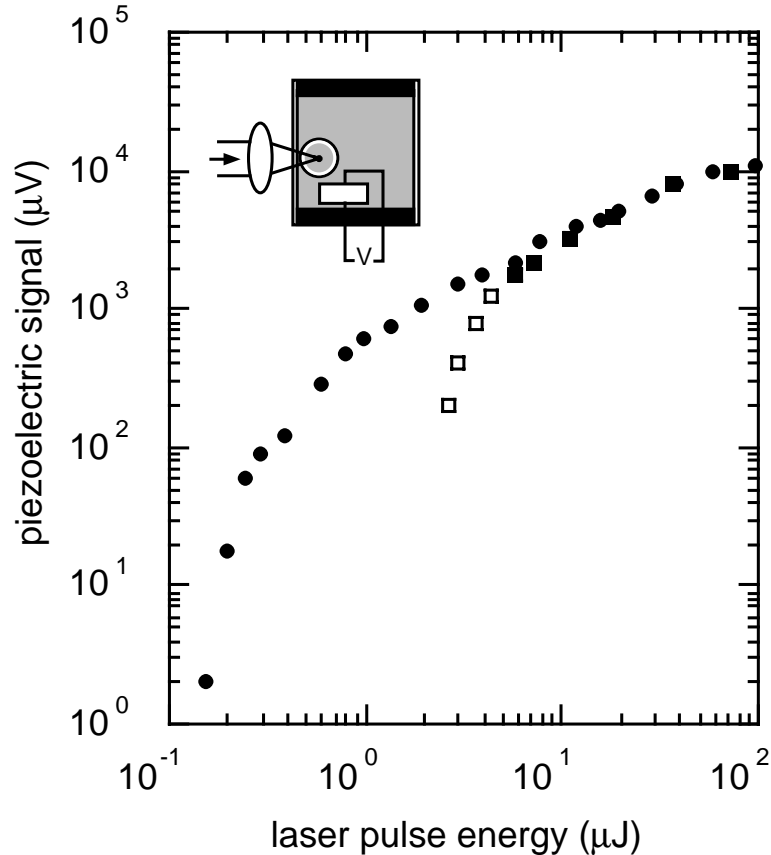
Figure 7.6 Comparison of the piezoelectric signal as a measure of the pressure produced by 100-fs pulses (filled circles) and 200-ps pulses (squares) in water. Each point is averaged over 100 pulses. For the 200-ps data, the open squares represent a range in pulse energy where some pulses produce no signal, while others significantly exceed the average. Inset shows the water cell for piezoelectric pressure measurements.

With 200-ps pulses no clear breakdown threshold exists. In the range 2–6 μJ, as the energy increases, an increasing percentage of the laser shots produce breakdown, with no breakdown below 2 μJ and breakdown on every shot above 6 μJ. In contrast, with 100-fs pulses there is little shot-to-shot variation in the pressure produced by the breakdown even very close to the threshold. Below 1 μJ, the absorbed fraction of each pulse diminishes with decreasing incident energy, but the breakdown occurs consistently from shot-to-shot. This difference in behavior occurs because the energy deposition for

100-fs pulses is initiated by multiphoton absorption, whereas the absorption of 200-ps pulses relies on absorbing impurities to generate the initial electrons (see Section 2.4).

For pulses with energies greater than 10 μJ we find a transmission of 20% through the water sample, indicating that a large fraction of the incident energy is absorbed. Assuming 80% absorption in this energy range, we can use the pressure measurements to extrapolate the absorption coefficient to smaller energies. The low pressure produced by 100-fs pulses near the 0.2-μJ threshold indicates that it is possible to consistently deposit a small fraction of the incident energy into the pressure wave — approximately 50 pJ. The ability to consistently deposit this low energy using femtosecond laser pulses could provide an important advantage for precise surgical applications.

7.4.3   Surface and sub-surface skin surgery

We examined the differences between femto- and picosecond laser-induced breakdown in tissue. Pulsed lasers are of medical interest for their precision and their ability to cut beneath a surface without damaging the layers above the focus.[13] We compared the effects of single 100-fs and 200-ps Ti:Sapphire laser pulses on the surface and in the bulk of skin. We used an in vitro, stratified human skin model, EpiDerm™, from MatTek Corporation. The 100-fs and 200-ps pulses were focused with a 0.65-NA microscope objective. The samples were translated during irradiation so that each laser pulse left a single isolated damaged region. For cross-sectional views, the samples were fixed in 10% formalin, stained in toluidine blue, then sliced in 30-μm sections using a vibratome and

photographed with an optical microscope. For top-views, photographs of unstained samples were taken with an optical microscope.

We compared laser ablation on the skin surface using 100-fs and 200-ps pulses. We find that although the ablation spot size is similar for femtosecond and picosecond pulse lengths at similar laser energies, the surrounding tissue damage is much greater for picosecond pulses. Figure 7.7a, and Figure 7.7b show top-view photographs of skin surface ablated by 200-ps and 100-fs pulses at 40-µJ energy. The 100-fs pulse ablated region has a diameter of ~14 µm, while the 200-ps pulse ablated region is about ~12 µm in diameter. However, the picosecond ablation diameter is difficult to define because the edge of the ablated region is jagged. The picosecond ablated region is surrounded by damaged tissue indicated by darkened, uneven areas and white, shiny areas with diameters up to 50 µm. By contrast, the femtosecond ablated region has clearly defined edges and the surrounding area is unaffected. The ablation threshold was determined as the lowest energy at which ablation spots were visible on the skin surface. For 100-fs pulses the threshold was ~2 µJ and the 200-ps threshold was ~5 µJ. Figure 7.7c and Figure 7.7d show surface ablation with a laser energy of four to five times the observed ablation threshold for each of the two different pulse lengths. Once again, the ablated regions have similar diameters of ~7 µm. The edges of the 200-ps ablation spots are jagged and show radiating damage, while the 100-fs ablation spots have smooth edges and show no collateral damage.
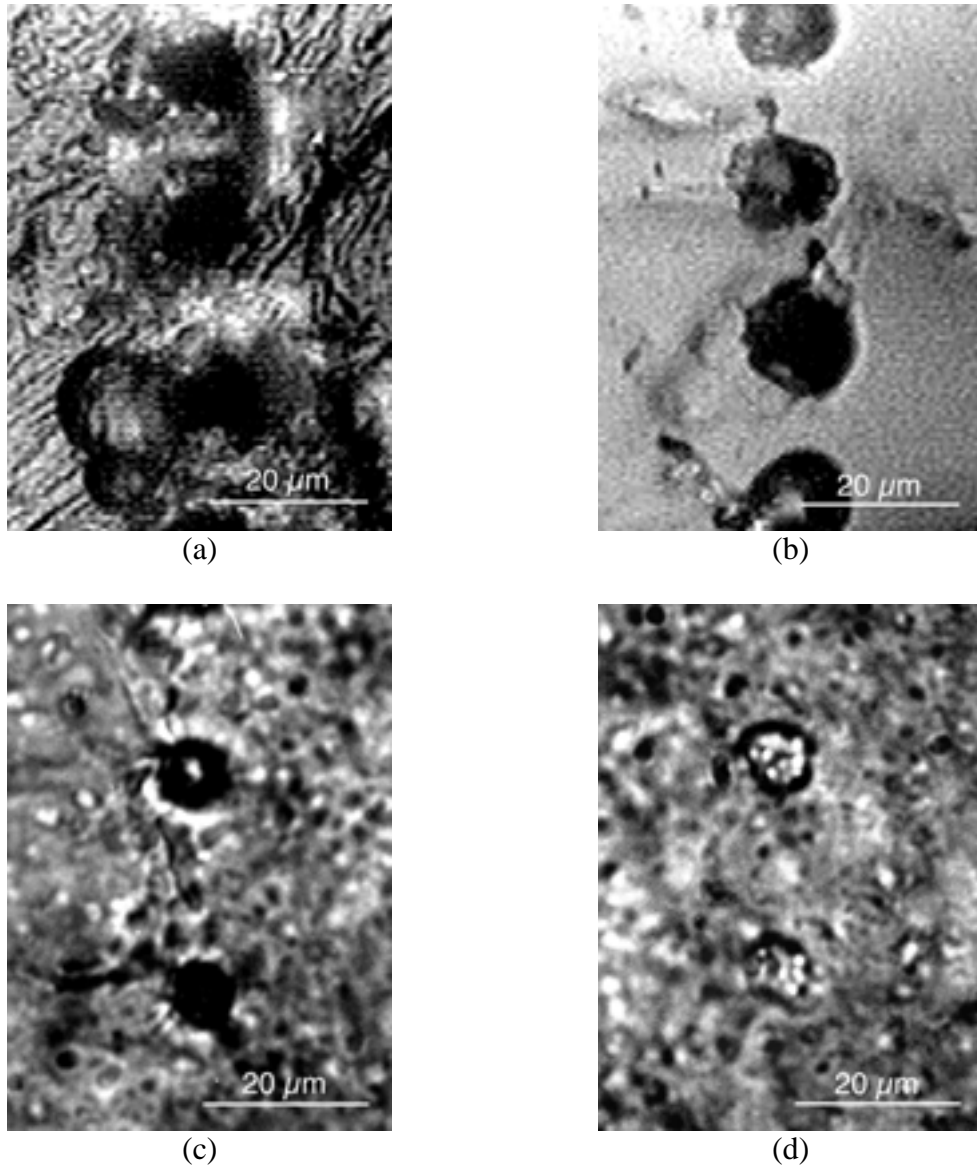
(a)   (b)

(c)   (d)

Figure 7.7 Surface ablation of human skin tissue using 100-fs and 200-ps laser pulses. (a) 200-ps, 40-µJ ablation spot on skin surface. (b) 100-fs, 40-µJ ablation spot on skin surface. Both ablation regions have similar size, but the collateral tissue damage is much greater for the 200-ps pulses. (c) 200-ps, 20-µJ ablation on surface. (d) 100-fs, 10-µJ ablation on surface. Again, the ablation regions for the two different pulse lengths are similar. However, the 200-ps pulse ablation region shows collateral tissue damage in a radiating pattern. All images are top-views of the surface.

We also compared sub-surface cavity formation in skin using femtosecond and picosecond laser pulses. Figure 7.8 shows a series of cavities produced with 100-fs, 20-µJ

152

pulses at varying depth beneath the surface. The cavities lie beneath the surface of the skin with no damage on the tissue surface itself. At 20 µJ of energy, 200-ps pulses caused cavities which ruptured the back of the sample at a depth of about ~100 µm. We did not see cavities from 100-fs pulses below about ~50 µm at 20 µJ.
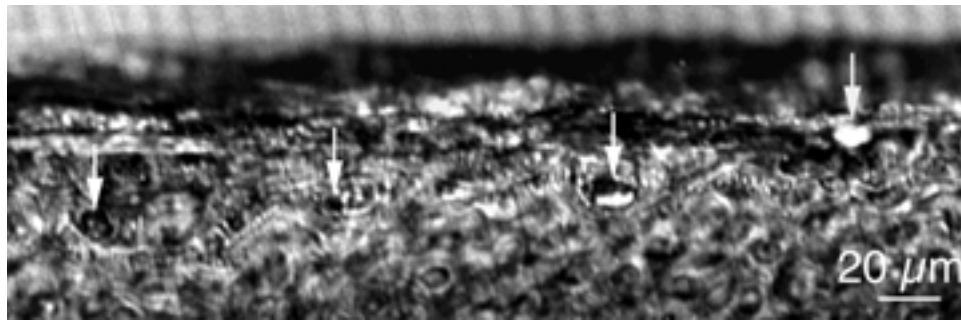

Figure 7.8 Cross-sectional view of a series of cavities made in the bulk of skin with 100-fs, 20-µJ pulses. Each pulse was focused at a different depth relative to the skin surface.

Figure 7.9 shows cavities from 200-ps and 100-fs pulses at 20 µJ. The cavities produced by 200-ps pulses are larger and elongated along the axis of beam propagation, while cavities produced by 100-fs pulses cover less than half the area of the picosecond cavities and are elongated perpendicular to the beam axis. In addition to having a larger size, cavities produced by picosecond pulses have more collateral tissue damage than those produced with 100-fs pulses. The more extensive collateral damage produced by the picosecond pulses can be seen in Figure 7.9a as a thick dark ring around the irradiated area. Figure 7.10 shows two subsurface cavities formed in mouse skin by single, 20 µJ, 100-fs pulses. The histology and imaging is better in this image, allowing better visualization of the precise sub-surface ablation that is possible with femtosecond pulses.

(a)   (b)
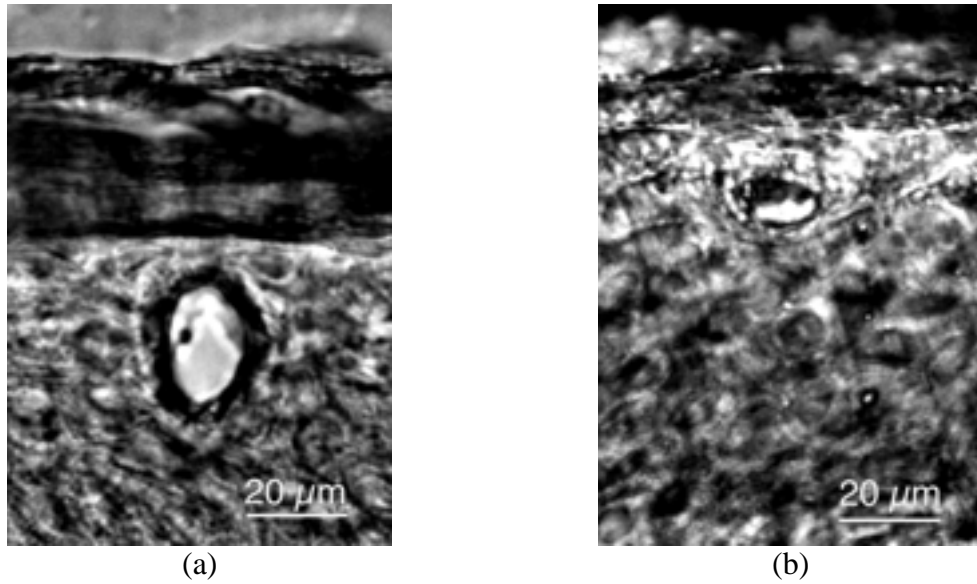
Figure 7.9 (a) Sub-surface cavity created by 200-ps, 20-µJ pulse. The cavity is surrounded by a thick ring of damaged tissue. (b) Sub-surface cavity created by 100-fs, 20-µJ pulse. This is a close-up of the third cavity from the left pictured in Figure 7.8. Both images are cross-sectional views.

Figure 7.10 Optical microscope image of the cross-section of a piece of mouse skin. The two subsurface cavities in the dermis were produced using a 100-fs, 20-µJ laser pulse.

Figure 7.11 shows a region on the surface of the skin sample that has been ablated with multiple, 100-fs, 4-μJ pulses. The sample was tr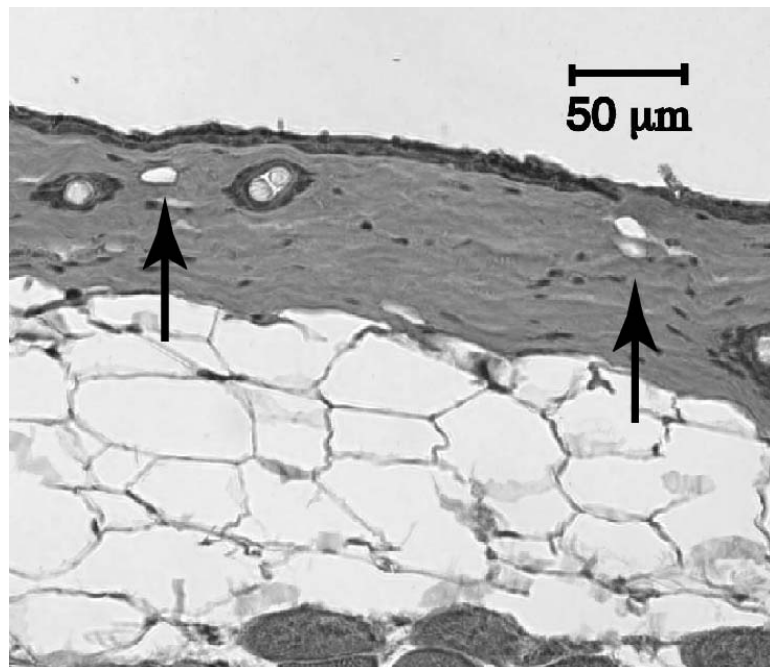anslated slowly under the laser beam, cutting a line across the skin surface. The width at the top of the ablated region is about 25 μm. The ablated region goes through the keratinized layer of the skin to a depth of about 25 μm. The edges of the ablation are straight and the surrounding tissue shows little damage.
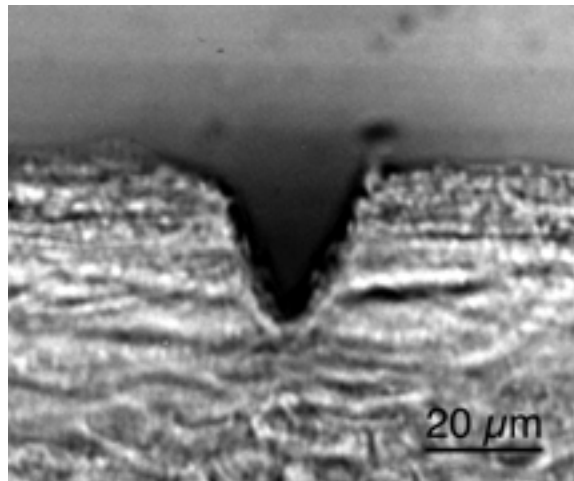
Figure 7.11 Cross-section of 25 μm-deep incision produced by multiple-shot ablation with 100-fs, 4-μJ laser pulses.

7.4.4   Conclusions

We investigated the potential of femtosecond and picosecond laser pulses for surgical use. We measured the breakdown threshold in water using a pressure wave detection technique. We find that femtosecond thresholds are significantly lower than picosecond thresholds. In addition, at energies near the breakdown threshold, picosecond pulses were unable to produce breakdown consistently. Femtosecond pulses, in contrast, produce breakdown with each pulse, even at threshold. We conclude that femtosecond pulses

allow for very low energy deposition, while still consistently producing breakdown. Comparisons of laser-induced ablation with femtosecond and picosecond pulses in skin shows that the collateral tissue damage is much less extensive for shorter pulses. This is evident in both surface ablation and bulk cavity formation. On the surface, both femtosecond and picosecond pulses produce similar ablation spot sizes, but in the bulk, cavities were found to be smaller for femtosecond pulses. Finally, we demonstrated that femtosecond pulses can produce very clean, precise incisions with minimal collateral damage in tissue by multiple shot ablation. These findings show that femtosecond lasers offer potential advantages over picosecond lasers in surgical applications.

7.5   Sub-cellular photodisruption

Organelles and other sub-cellular structures provide the machinery by which cells carry out their basic functions. Understanding the role of individual sub-cellular structures and how these structures interact in a cell is one of the major challenges in cell biology research today. A common technique for connecting cellular functions to specific sub-cellular structures is to use biochemical and genetic techniques to disturb the sub-cellular structure and observe how the cellular function is affected. Because of the complexity of the biochemical and genetic processes in a cell, however, it is difficult to isolate effects with high certainty.

Individual sub-cellular structures can also be physically manipulated, but the techniques available to date have not had sufficient precision to disrupt small structures without affecting the rest of the cell. By focusing nanojoule, femtosecond laser pulses with high numerical-aperture microscope objectives, however, it is possible to cause

photodisruption in cells with sub-cellular precision. Because the laser focus can be located inside the cell, we can disrupt sub-cellular structures inside the cell without affecting the cellular membrane. In addition, because the total energy deposited into the cell is small, the temperature rise in the cell is small. The small scale of the disrupted region together with the low temperature rise may allow sub-cellular structures to be disrupted without affecting the viability of the rest of the cell. This would prove a very useful tool for studying the function of various structures in live cells. To demonstrate this technique, we photodisrupt sub-cellular regions in biochemically fixed cells.

As shown in Figure 7.12, a fluorescence microscope is set up colinearly with the femtosecond laser system to visualize the target cell during photodisruption. In our study, we use fibroblast cells with actin fibers tagged with fluorescein isothiocyanate (FITC). We translate the cell while continuously irradiating to make channels inside the cell or we disrupt selected regions of the cell with a varying number of laser pulses. After laser irradiation, we image the cell using fluorescence confocal microscopy to obtain a series of image slices at different depths in the sample.
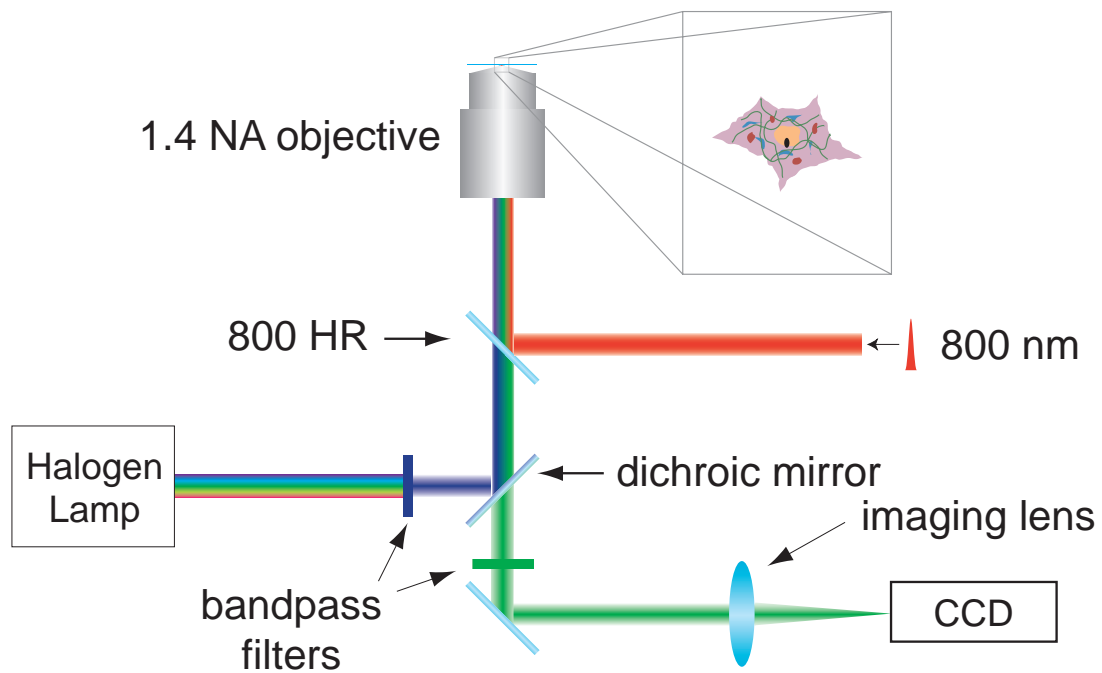
Figure 7.12 Setup for sub-cellular photodisruption. A fluorescence microscope is used to visualize the target cell while single femtosecond pulses or pulse trains disrupt sub-cellular structures.

Figure 7.13 shows the central slice of a cell photodisrupted using 100-fs laser pulses focused by a 1.4-NA microscope objective with laser energy ranging from 0.5 to 2.0 nJ. The size of the channels through the top half of the cell are comparable to the width of an actin fiber bundle. In the lower half of the cell, regions were disrupted using varying number of pulses. Figure 7.14 shows the side view of a cell disrupted with 2nJ, 100-fs laser pulses. Tissue is removed only from the middle of the cell while both the top and bottom layers remain intact. The very small amount of energy needed and near-infrared wavelength of the laser light used to photodisrupt sub-cellular structures suggest the possibility of applying this prodedure to living cells for cellular structure and function

research. Using this method, it is possible to directly study biology problems such as organelle function, cell repair mechanisms, and intracellular signal transduction.
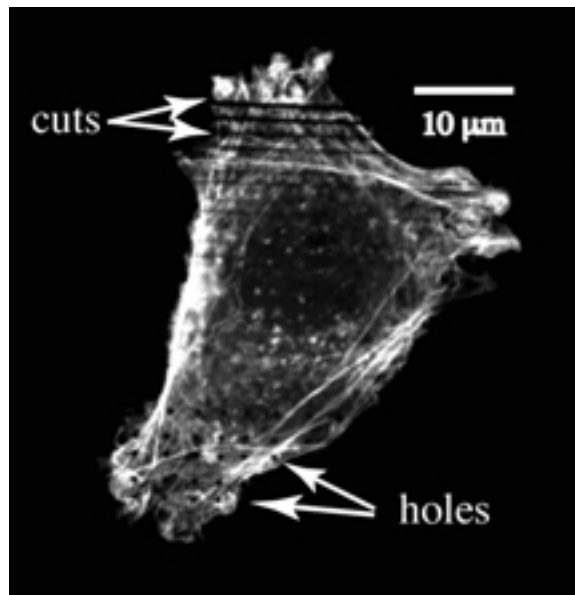

Figure 7.13 Fluorescence confocal microscope image of the central slice of a cell photodisrupted by 100-fs laser pulses. Top half of the cell shows laser-produced channels Energy of the laser pulses used decreases from 2 nJ at the top to 0.5 nJ at the bottom. A varying number of laser pulses ranging from 500 to 100 per spot were used to create cavities in the lower half of the cell.
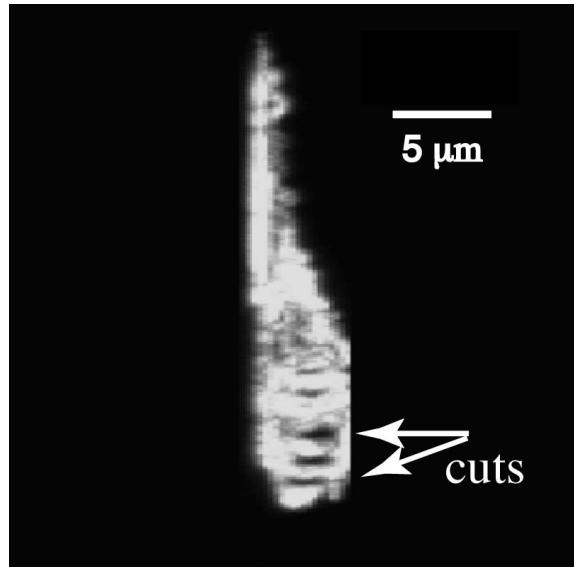
Figure 7.14 Fluorescence confocal microscope image of the side view of a photodisrupted cell. The cigar-shaped dark regions are laser-produced channels.

7.5.1 Integration with nonlinear microscopy

The setup shown in Figure 7.12 could be combined with a nonlinear microscope[21] to make a powerful biological research tool. In nonlinear microscopy, a short laser pulse is focused into the sample. The wavelength of the laser is selected to be in the transparency region of the sample. At the laser focus, the intensity can become high enough to induce nonlinear processes. Because this nonlinear signal can vary with local sample properties, it can be used to provide optical contrast in the image. For example, one could tag a specific structure in a sample with a fluorescent dye, excite the dye using two-photon abosroption, and image the fluorescent light. Recently, a whole gamut of nonlinear processes have been used for imaging, including second harmonic generation,[22] third harmonic generation,[23] and coherent anti-Stokes Raman scattering.[24] Because the process is nonlinear, the signal is generated only from the focal region, where the laser

160

intensity is high, allowing three-dimensional optical sectioning of the sample. With tight external focusing, nonlinear microscopy achieves a resolution equal to or better than confocal microscopy.[21]

Because the threshold energy for sub-cellular photodisruption is less than 5 nJ, an unamplified laser can be used. To avoid the cumulative heating effects described in Section 4.7, individual pulses have to be sliced out of the pulse train to induce photodisruption. As shown in Figure 7.15, the pulses not sliced out for photodisruption can then be attenuated to below the damage threshold for the sample and used for nonlinear imaging. This would allow real-time, three-dimensional imaging of the cell before, during, and after photodisruption of a particlular sub-cellular structure.
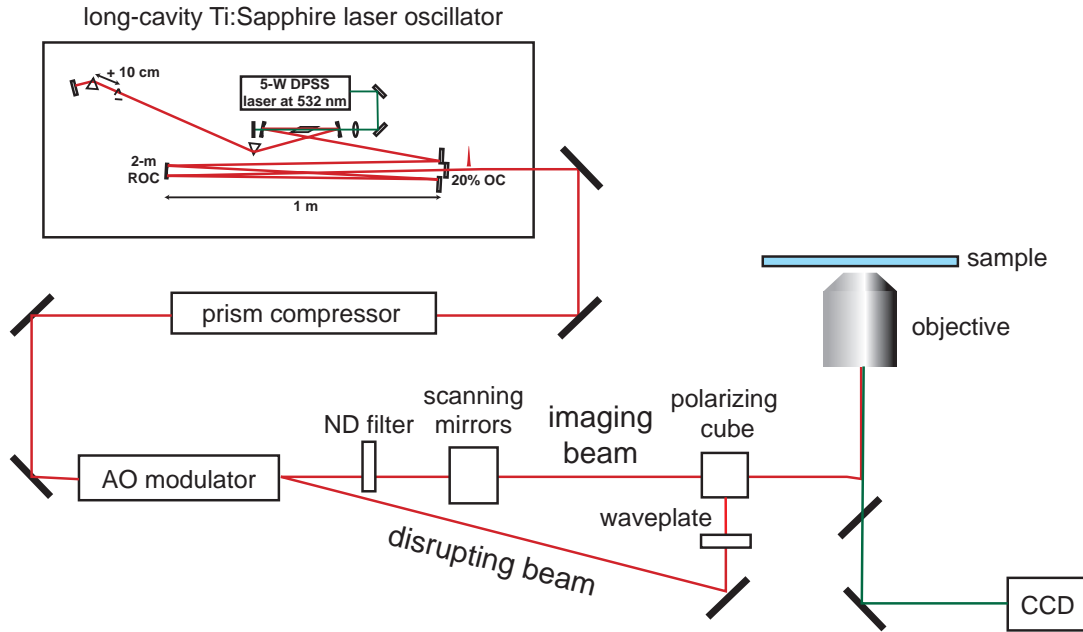
Figure 7.15 Nonlinear microscope with integrated photodisruption capabilities. Pulses from a long-cavity Ti:Sapphire laser oscillator go through a prism compressor for dispersion compensation and are then split into two beams by an acousto-optic modulator. The beams are recombined using a polarizer and directed through a microscope objective to the sample. One beam is attenuated and scanned by scanning mirrors to induce, for example, two-photon fluorescence which is imaged onto a CCD camera. The other, unattenuated, beam is used to photodisrupt sub-cellular structures.

References

1. S. Nolte, G. Kamlage, F. Korte, T. Bauer, T. Wagner, A. Ostendorf, C. Fallnich, and H. Welling, *Advanced Engineering Materials* **2**, 23 (2000).

2. X. Liu, D. Du, and G. Mourou, *IEEE J. Quantum Electron.* **33**, 1706 (1997).

3. E. N. Glezer, M. Milosavljevic, L. Huang, R. J. Finlay, T.-H. Her, J. P. Callan, and E. Mazur, *Opt. Lett.* **21**, 2023 (1996).

4. C. B. Schaffer, A. Brodeur, J. F. Garcia, and E. Mazur, *Opt. Lett.* **26**, 93 (2001).

1. K. M Davis, K. Miura, N. Sugimoto, and K. Hirao, *Opt. Lett.* **21**, 1729 (1996).

2. K. Miura, J. Qui, H. Inouye, T Mitsuyu, and K. Hirao, *Appl. Phys. Lett.* **71**, 3329 (1997).

3. D. Homoelle, S. Wielandy, A. L. Gaeta, N. F. Borrelli, and C. Smith, *Opt. Lett.* **24**, 1311 (1999).

4. D. N. Fittinghoff and J. A. Squier, *Opt. Lett.* **25**, 1213 (2000).

5. D. N. Fittinghoff, P. W. Wiseman, and J. A. Squier, *Optics Express* **7**, 273 (2000).

6. A. Egner and S. W. Hell, *J. Opt. Soc. Am. A* **17**, 1192 (2000).

7. M. Watanabe, S. Juodkazis, H.-B. Sun, S. Matsuo, H. Misawa, M. Miwa, and R. Kaneko, *Appl. Phys. Lett.* **74**, 3957 (1999).

8. Y. R. Shen, The Principles of Nonlinear Optics, New York: Wiley, 1984, pp. 528–540.

9. P. A. Barnes and K.E. Rieckoff, *Appl. Phys. Lett*. **13**, 282 (1968).

10. B. Zysset, J. G. Fujimoto, and T. F. Deutsch, *Appl. Phys. B*. **48**, 139 (1989).

11. T. Juhasz, G. A. Kastis, C. Suarez, Z. Bor, and W. E. Bron, *Lasers Surg. Med.* **17**1 (1995).

12. B. Zysset, J. G. Fujimoto, C. A. Puliafito, R. Birngruber and T. F. Deutsch, *Lasers Surg. Med.* **9**, 193 (1989).

13. J.M. Krauss and C. A. Puliafito, Lasers in Ophthalmology, in *Laser Surgery and Medicine: Principals and Practice*, ed. by C. A. Puliafito (Wiley-Liss, New York, 1996), Chap. 8.

14. R. F. Steinert and C. A. Puliafito, *The Nd:YAG laser in Ophthalmology*. (Philadelphia, PA: Saunders, 1985).

15. A. G. Doukas, A. D. Zweig, J. K. Frisoli, R. Bringruber, and T. F Deutsch, *Appl. Phys. B*. **53**, (1991).

16. F. H. Loesel, J. P. Fischer, M. H. Gotz, C. Horvath, T. Juhs, F. Noack, N. Suhm, and J. F. Bille, *Appl. Phys B*. **66**, 121 (1998).

17. A. A. Oraevsky, L. B. DaSilva, A. M. Rubenchik, M. D. Feit, M. E. Glinsky, M. D. Perry, B. M. Mammini, W. S. Small IV, and B.C. Stuart, *IEEE J. Select. Topics Quantum Electron.* **2**, 801 (1996).

18. J. Noack, D. X. Hammer, G. D. Noojin, B. A. Rockwell, and A. Vogel, *J. Appl. Phys.* **83**, 7488 (1998).

19. E. N. Glezer, C. B. Schaffer, N. Nishimura, and E. Mazur, *Opt. Lett*. **22**, 1817 (1997).

20. J. G. Fujimoto, W. Z. Lin, E. P. Ippen, C. A. Puliafito, and R. F. Steinert, *Invest. Ophthalmol. Vis. Sci.* **26**, 1771 (1985).

21. W. Denk, J. H. Strickler, and W. W. Webb, *Science* **248**, 73 (1990).

22. L. Moreaux, O. Sandre, M. Blanchard-Desce, and J. Mertz, *Opt. Lett.* **25**, 320 (2000).

23. J. A. Squier, M. Müller, G. J. Brakenhoff, and K. R. Wilson, *Optics Express* **3**, 315 (1998).

24. M. Muller, J. Squier, C. A. De Lange, and G. J. Brakenhoff, *Journal of Microscopy* **197**, 150 (2000).

Chapter 8

Conclusions and outlook

The interaction of intense laser pulses with transparent materials has remained an active area of research since the advent of Q-switched ruby lasers. Despite this long history, there remains much that we do not know. Some issues are addressed in this thesis, others remain unsolved, and new questions arise from the work presented here. In this final chapter, we review some of the key conclusions of this thesis and briefly discuss areas where further work is sorely needed.

By measuring the threshold intensity for bulk material damage induced by femtosecond laser pulses, the dominant nonlinear ionization mechanism for different laser and material parameters was determined. In particular, we found that for small band gap materials, photoionization produces a large fraction of the electron density, while for large band gap materials, avalanche ionization (seeded by photoionization) is responsible for most of the ionization. For short laser wavelength, photoionization is best characterized by a multiphoton absorption process, while for long laser wavelength, tunneling ionization is a more appropriate description. The bulk intensity threshold for damage we measure in fused silica agrees well with literature values for surface damage,

indicating that surface effects are minimal. For CaF_2, however, literature values for the surface damage threshold are lower than what we measure for the bulk.

In future work, measurements of the pulse duration dependence of the intensity threshold for bulk ionization for different material band gap and laser wavelength would allow the nonlinear photoionization rate and the avalanche ionization rate to be determined independent of any models. By comparing the dependence of these ionization rates on laser wavelength and material band gap with that predicted by contending theories, one could hopefully resolve some of the controversy about the validity of Keldysh's theory for nonlinear photoionization and the correct model for avalanche ionization. The effects of incubation when multiple shots irradiate one spot in the sample, as well as the origin of the difference (or lack of difference) between surface and bulk damage thresholds should also be investigated.

Nonlinear ionization deposits laser energy into a transparent material, how that energy leads to material changes is another question. By investigating the morphology of the structural change produced in bulk glass by tightly-focused femtosecond laser pulses with different laser energy and focused at different numerical apertures, we identified a transition between two different structural change morphologies. At high laser energy, an explosive expansion of the hot laser-produced plasma leaves a void or less-dense central region surrounded by a densified shell. At lower laser energy, small density changes are induced in the glass either by melting and nonuniform resolidification or by non-thermal bond breaking and structural rearrangement. Furthermore, we find that the extent of the structural change is determined by the focal volume of the focusing objective only for pulse energies up to a few times the threshold energy. For higher pulse energies, the

structural changes extend upstream toward the laser from the focus because the threshold intensity is reached in front of the laser focus. For micromachining applications, the highest precision is achieved if laser pulse energies close to threshold are used.

For very tight external focusing, the threshold for producing a structural change is within the range of an unamplified laser oscillator. Micromachining with an oscillator allows faster machining speeds and permits the use of a cheaper laser source. Oscillator-only micromachining also enables a new, cumulative thermal mechanism to be used to produce a structural change. If the repetition rate of the laser is high enough that energy is deposited by nonlinear absorption faster than it can be carried out of the focal volume by thermal diffusion, then the pulse train serves as a sub-micrometer-sized source of heat located inside the bulk of the material. Over many pulses, micrometer-sized regions of the material melt and can resolidify nonuniformly, leading to refractive index changes that can be used for micromachining optical devices.

Future research could investigate the nature of the structural change that is produced by single laser pulses near the threshold. Measurements of photoluminescence, Raman, and ultraviolet absorption spectra could reveal the structural rearrangements that have occurred, and hopefully uncover the mechanism for structural change. The cumulative bulk heating effect should be studied in different materials, with the goal of identifying materials in which large refractive index changes can be produced. It would also be interesting to systematically study the size of the melted region as a function of laser repetition rate and shot number. For pulses arriving slower than the thermal diffusion time, there should be no cumulative effects. For pulses arriving faster than the plasma recombination time, linear absorption by the plasma left by the previous pulse

should greatly enhance the absorption of subsequent pulses. The experiments discussed in this thesis lie in between these two extremes, where the plasma completely recombines between pulses, but the thermal energy does not have time to diffuse away. The bulk heating effect may also provide a unique means for studying the thermal properties of materials. No other technique allows for such precise delivery of thermal energy into bulk transparent materials. An addition to structural changes, femtosecond laser irradiation with tightly-focused pulses could produce localized chemical changes in some transparent materials. This micrometer scale chemistry could have great utility if the solubility properties of the material were changed. In addition to direct photochemistry, the bulk heating effect could locally fuel thermally-driven chemical changes.

Loosely focusing a femtosecond laser pulse into a transparent material produces a white-light continuum pulse. The mechanism for this continuum generation has eluded researchers for decades. We measured the band gap and pump wavelength dependence of the extent of the continuum broadening, and found that the blue broadening decreased linearly with increasing pump frequency and increased with increasing band gap. These parametric dependences of the continuum features allowed us to identify the mechanisms responsible for continuum generation. Briefly, self-focusing leads to an increase in the peak laser intensity, triggering self-phase modulation which broadens the laser spectrum. Self-steepening and space-time focusing tend to skew the pulse envelope so that a steep, shock-like edge develops at the trailing edge of the pulse. The rapid intensity change on this trailing edge leads to strong blue broadening due to self-phase modulation, producing the plateau characteristic of continuum generation. Nonlinear ionization produces an electron plasma whose contribution to the refractive index defocuses the laser pulse and

halts self-focusing. This plasma defocusing limits the peak laser intensity and therefore limits the steepness of the optical shock and thus the extent of the blue broadening. This mechanism is confirmed by simulations which take all of the above effects into account and which reproduce the observed pump wavelength dependence of the broadening in fused silica.

The observation that a femtosecond laser pulse produces damage but no white light when tightly focused into a transparent material and produces white light but no damage when loosely focused into the material led us to investigate the dependence of white light and damage on the external focusing angle. We found an abrupt increase in the white-light threshold along with a qualitative change in the white-light spectrum, and an abrupt decrease in the damage threshold as well as indications of a change in the damage morphology as the numerical aperture of the external focusing increases above 0.07. These changes indicate a fundamental change in the nature of the interaction, suggesting a transition from propagation dominated by nonlinear effects at low numerical aperture to propagation dominated by diffraction at high numerical aperture.

Further experimental studies of the continuum could help to more firmly establish the scenario presented above for continuum generation. One could, for example measure the change in the pulse envelope as the laser power approached the threshold for continuum generation in order to confirm the development of the steep, shock-like edge by self-steepening and space-time focusing. More simulations of the continuum spectrum for different laser wavelengths and different band gap materials would also help establish the validity of the model. Further exploration of the focusing angle dependence of the continuum threshold and spectrum and the damage threshold and morphology are also

warranted. The role of color centers produced either by multiphoton absorption of infrared laser light or by linear absorption of the blue tail of the continuum needs to be established as well as the nature of the damage produced for different focusing angles. Additional modeling should help identify the various competing effects that cause the abrupt changes observed at a numerical aperture of 0.07.

The dynamics of laser-induced breakdown in water was studied using time-resolved imaging and time-resolved scattering. The imaging resolution in these experiments surpassed that which was previously achieved, allowing observation of the picosecond time scale dynamics where the plasma is small. We observe a 20 ps delay before there is any observable growth in the plasma size, which we attribute to electron-ion energy equilibration. Most of the electrons cannot leave the focal volume without the ions because of the Coulomb attraction, and it takes tens of picoseconds for the electrons to collisionally heat the ions so that electrons and ions can expand together. A very rapid growth of the plasma is observed from 30 ps to 200 ps. This growth is most likely not due to a physical expansion of the laser-produced plasma, but rather due to generation of plasma outside the focal volume. This plasma generation could be due to the very high energy tail of the electron distribution running away from the focal volume and producing more electrons though impact ionization, or, perhaps, due to photoionization of electrons outside the focal volume by the ultraviolet component of the recombination light from the laser-produced plasma. The physical expansion of the laser-produced electron-ion plasma proceeds at a much slower rate and launches a pressure wave when the expansion uses up its energy. The pressure wave propagates away at the speed of

sound. After the electron-ion plasma recombines, the gas bubble that remains expands and recollapses as a cavitation bubble.

Additional measurements of the plasma, especially at early times would help to establish the mechanism for the rapid plasma growth that we observed. By measuring the time-resolved reflection and transmission of the plasma, the plasma density could be determined which, together with the scattering and imaging measurements should provide a measure of the plasma size that is not encumbered by image resolution issues.

There are several applications of the work presented in this thesis. The refractive index changes produced by single laser pulses or by high-repetition rate trains of pulses can be used to fabricate optical waveguides and other photonics devices inside bulk transparent materials. We demonstrated direct writing of waveguide splitters using the refractive index changes produced by single pulses. We also showed that waveguides can be directly written into a transparent material using the cumulative pulse thermal effect discussed above. This femtosecond thermal micromachining requires only an unamplified femtosecond laser oscillator, greatly simplifying the laser technology needed for three-dimensional optical device fabrication.

The damage produced inside bulk transparent solids by tightly-focused femtosecond laser pulses can also be produced inside transparent tissues and cells, providing an extremely precise laser scalpel. We demonstrated the superior precision of femtosecond compared to picosecond pulses for surface and sub-surface cutting of human skin tissue. More interestingly, the damage produced by a femtosecond pulse can be confined to a region much smaller than a single cell, enabling the disruption of sub-cellular structures for biological research applications. We demonstrated that actin fibers

can be disrupted inside fixed cells without disturbing the cellular membrane either above or below the disrupted region. Integration of a nonlinear microscope with the sub-cellular disruption setup would provide a versatile tool for studying topics such as mechanical signal transduction and cell repair in live cells.

Additional work on writing waveguides and other devices with the thermal mechanism should be carried out. Finding a material which undergoes a large refractive index change when it is melted and resolidifies is a high priority for industrially-viable waveguide writing. To work in materials with different refractive index, the laser beam must be focused more slowly into the material to avoid spherical aberration. Slower focusing, in turn, means that higher pulse energies are required to produce breakdown. Mode-locked fiber lasers and fiber amplifiers may provide the necessary energy at high enough repetition rate for cumulative heating to occur. In biological materials, more investigation of the limits of sub-surface disruption in turbid tissues are needed to determine crucial factors such as how deep inside the material we can cut, and how short a pulse is really needed. In single cells, the femtosecond laser scalpel promises to open up an entirely new technique for studying the function of various sub-cellular structures. Live cell studies are needed to confirm the viability of cells after disruption of various sub-cellular structures.

The study of the interaction of ultrashort laser pulses with transparent materials will undoubtedly continue for some time. The physics of the extremely nonlinear interaction remains unresolved, and new applications drive more research in this area.